DEVELOPMENT OF A HIGH-SPEED ROTATING BAR MECHANISM

by

David Allen White

Thesis submitted to the Faculty of the

Virginia Polytechnic Institute and State University

in partial fulfillment of the requirements for the degree of

Master of Science

in

Mechanical Engineering

APPROVED:

Dr. Wing F. Ng, Chairman

Dr. Thomas E. Diller

Dr. R. Gordon Kirk

Dr. Reginald G. Mitchiner

December 1995

Blacksburg, Virginia

Key words: Design, Rotordynamics, High-Speed, Rotating, Shock Wave

Development of a High-Speed Rotating Bar Mechanism

by

David Allen White

Dr. Wing F. Ng, Committee Chairman

Mechanical Engineering

ABSTRACT

A high-speed rotary device was designed to generate shock waves in a transonic blowdown wind tunnel cascade. The rotary device (Rotating Bar Mechanism) will be used in research conducted at Virginia Tech to study the effects of unsteady aerodynamic flow and heat transfer (resulting from upstream shock wave / wake passing) on turbine blades.

The rotating bar mechanism (RBM) consists of: a rotor with flexible cable "bars" attached to the rim of the disk, a disk housing, a bearing housing, a driving air turbine, and a turbine mounting housing. The RBM is mounted to the side of the wind tunnel so that only the bars enter and exit the tunnel test section through a small slot. As the bars translate through the test section, the bars create shocks / wakes similar to those shed from the trailing edges of nozzle guide vanes of a transonic turbine.

Considerable design effort was required for the RBM due to it's relatively high operating speed. As the result of a finite element stress analysis, a unique method of

securing the disk to the shaft was developed. This unique method reduced the stress concentration factor at the disk hub from 2.9 to 1.7. In addition to the stress analysis, a rotordynamic study was also performed. The study revealed that the RBM could not be designed to operate below the first natural frequency. A critical speed of 14,000 RPM was predicted for the rotary device. This prediction was later verified by testing.

An integral component of the overall design was the development of a computer code to predict the RBM's speed under various loading conditions. The loading on the device is due primarily to the aerodynamic drag on the flexible cable bars. Since the mechanism was design to facilitate bars of different diameters, the prediction code was an essential design tool. The speed prediction code was also verified by testing. The RBM was tested to wind tunnel operating speeds in a spin pit filled with argon to verify the mechanical design. Based on test performance, it was concluded that the RBM is suitable to generate shock waves in a transonic wind tunnel.

Acknowledgments

I would like to take this opportunity to thank the many individuals who have contributed to this thesis and made my graduate studies a very memorable time. My sincere thanks to professors Dr. Tom E. Diller, Dr. R. Gordon Kirk, Dr. Reginald G. Mitchiner, and Dr. Wing F. Ng for giving their valuable time and insight while serving on my advisory committee. In addition, I would like to thank Dr. Larry D. Mitchell for his exceptional input on various aspects of the mechanical design of my project. Furthermore, I sincerely thank Dr. Tibor Kiss for his assistance with the finite element analysis and his extremely helpful recommendations regarding the overall project design. I would also like to thank Jamie Hale for his assistance in testing the Rotating Bar Mechanism.

I also wish to thank several former fellow employees at Chevron USA, Inc. in New Orleans who made my graduate studies possible. First, I'd like to acknowledge Lionel "The Hammer" Hamrick for his unwavering confidence in me and all of his subordinates. Also, I'm extremely grateful to Sid Olivier and Bob Howard for their exemplary leadership. Both Sid and Bob took exceptional steps in defending their employees through some turbulent times in the oil industry. Finally, I would like to recognize Jim Howard. Jim personifies all of the qualities of a true leader. He took countless young engineers under his wing and helped to nurture their careers. Jim set an

example of amiable, open-minded leadership that will remain with me for the rest of my life.

Table of Contents

List of Illustrations

List of Tables

Nomenclature

C_{Dc}	drag coefficient on the bars in the cascade test section
C_{Dh}	drag coefficient on the bars in the disk housing
d	bar diameter
D_t	disk friction torque
E_k	kinetic energy
g	acceleration due to gravity
g_c	constant relating force, mass, length and time
Hz	hertz, frequency
N_c	number of bars in the cascade test section
N_h	number of bars in the disk housing
r	radius
R_{cg}	centroid
r_m	mean bar radius
rpm	revolutions per minute
U	bar velocity in the disk housing
V	bar-relative velocity at mean bar radius
y	thickness

$\in$	unit strain
γ	shear strain
μ	Poisson's ratio
ρ	gas density
σ	radial, tangential stress
σ'	von Mises stress
ω	rotational speed, radians per second

1.0 Introduction

Since the advent of aircraft gas turbine engines, considerable experimental research has been devoted to wind tunnel cascade tests of transonic turbine blading. However, most of the cascade tests have not been able to model the unsteady aerodynamic flow and the heat transfer performance resulting from the relative rotation of upstream blade rows. The downstream blades rotate through shock waves shed by the upstream blade row. This phenomenon is known as "shock wave passing" and is illustrated in Figure 1.1. Another unsteady flow phenomenon occurs in subsonic flow when wakes are shed by the upstream blade row; the event is known as "wake passing". Studies by Doorly and Oldfield (1985), among others, have shown that shock wave passing and wake passing greatly contributes to flow unsteadiness and may significantly affect the heat transfer rate to the turbine blades.

Research is currently being conducted at Virginia Tech to study the effects of unsteady aerodynamic flow and heat transfer (resulting from upstream shock wave / wake passing) on turbine blades. The research utilizes a two-dimensional cascade of stationary blades with an upstream shock wave / wake generator. The shock wave / wake generator contains a rotor with flexible cable "bars" attached to the rim of the disk. This Rotating

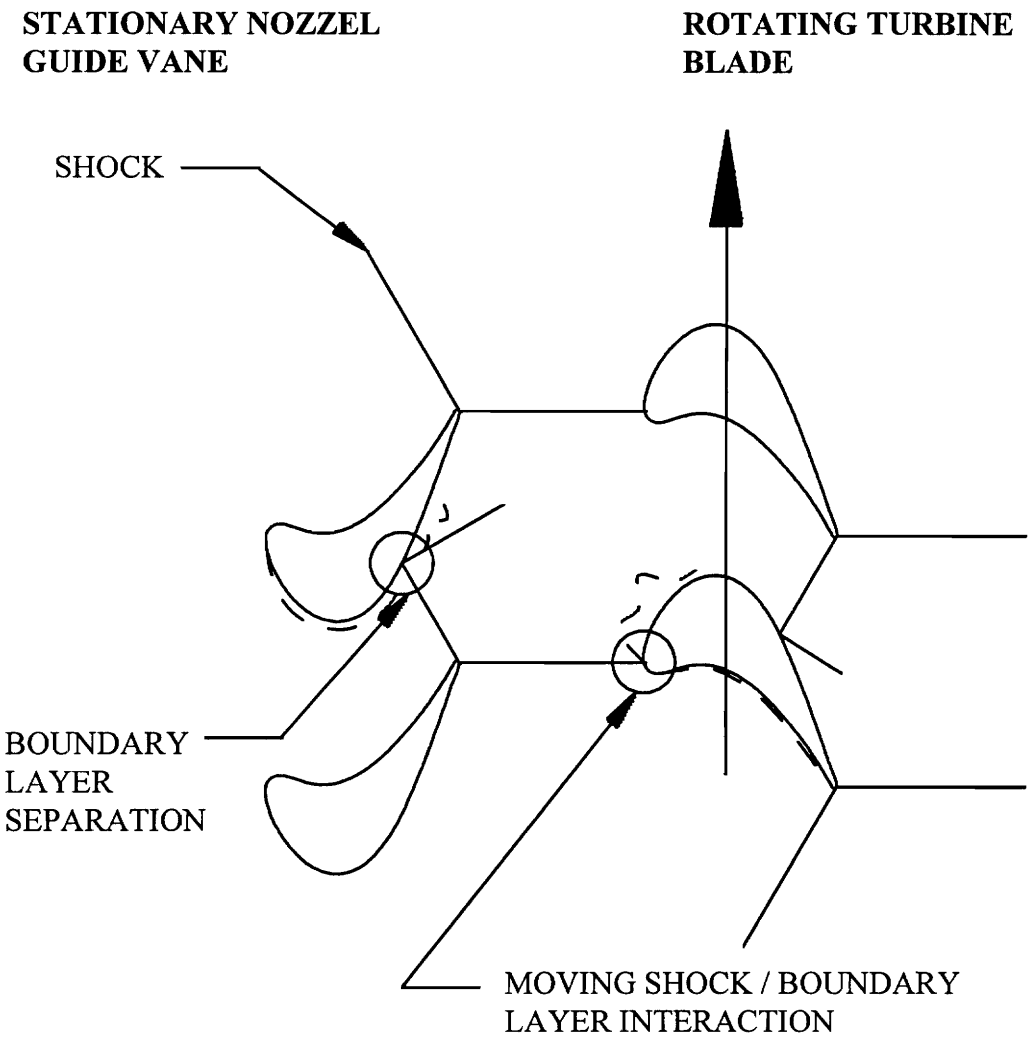

Figure 1.1: Diagram of Shock Wave Passing

Bar Mechanism (RBM) is mounted to the side of the tunnel such that only the bars enter and exit the tunnel test section through a small slot. The bars, which rotate through a plane parallel to the leading edges of the turbine blades, create shocks/wakes similar to those shed by the trailing edges of nozzle guide vanes of a transonic turbine. A conceptual model of the tunnel cascade and RBM is depicted in Figure 1.2.

1.1 Previous Research

Previous research utilizing RBM's to generate shock waves in turbine cascades is limited to tests in the Isentropic Light Piston Tunnel at Oxford University (Doorly, 1984). Doorly conceptualized a rotary wake generator capable of producing shock waves based on metal "squirrel cages" upstream up the cascade blade row to generate planar wakes (Bayley et all, 1980 and Pfeil et all, 1982). The squirrel cages simulated a continuous row of parallel bars passing upstream of the cascade. Realizing that the squirrel cage arrangement was unsuitable to simulate shock waves, Doorly applied the concept of passing a continuous row of bars through the test section. He noted that the continuous bar row could be viewed as bars (extending in the radial direction) attached to the rim of a disk of infinite diameter. Substituting the infinite diameter disk with a disk of large finite dimensions, Doorly was able to construct a suitable wave / wake generator.

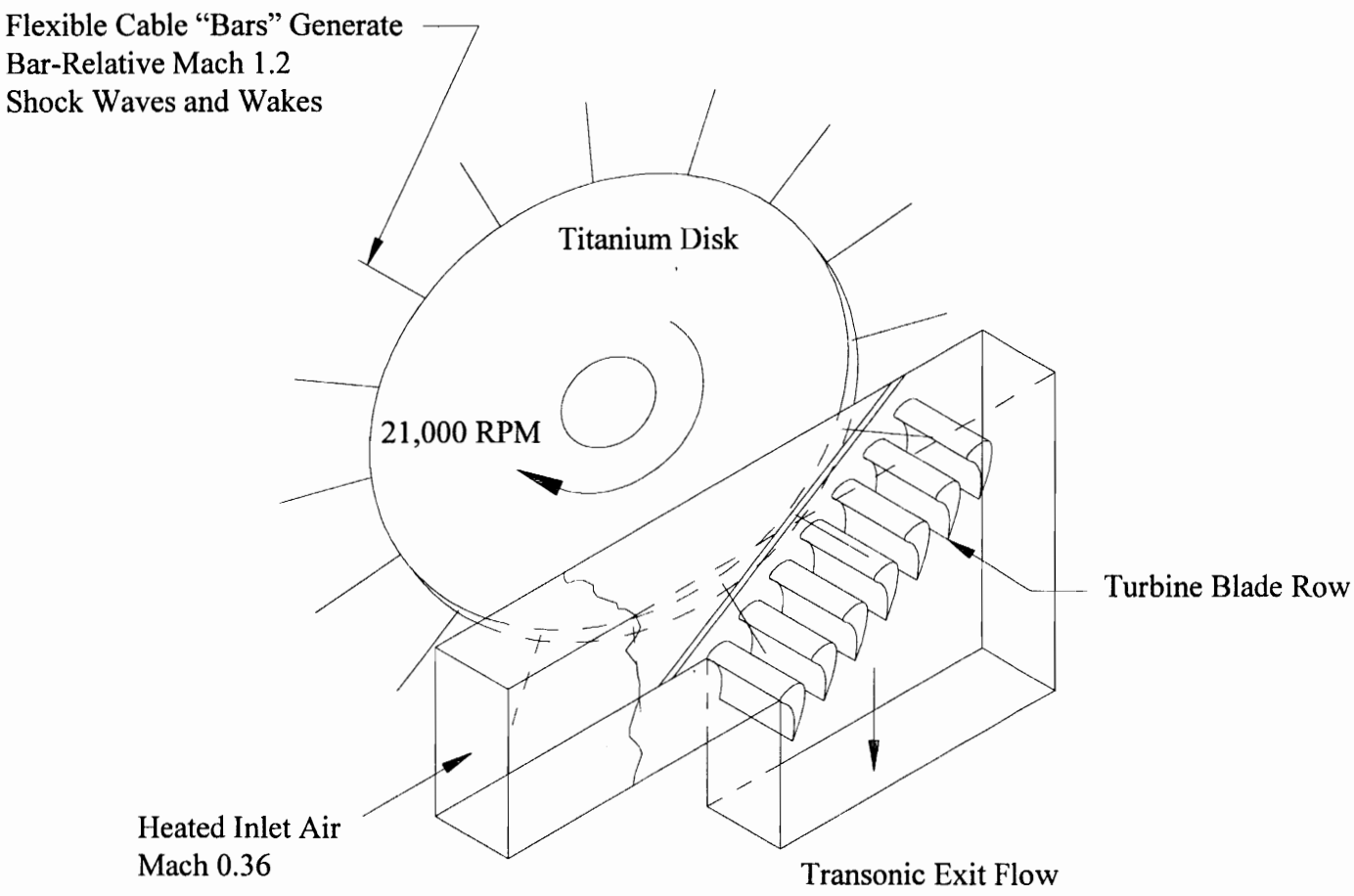

Figure 1.2: Conceptual Diagram of Wind Tunnel Cascade and Rotating Bar Mechanism

The RBM developed at Oxford included a rotor attached to the test section of the cascade tunnel. Sixteen flexible cable "bars" were attached to the rim of the disk through dovetail retaining pieces. The bars were allowed to cyclically pass upstream of the cascade blade row via a small slot in the test section door (the disk did not enter the test section).

The experiments performed using this apparatus involved spinning the rotor to 20,000 RPM for up to 0.4 seconds. The turbine used to power the RBM was insufficient to overcome the drag on the bars in ambient air. Therefore, the test section was evacuated before accelerating the rotor. After the rotor reached a desired overspeed, the tunnel was started and the inertia of the disk was used to minimize the decay of rotational speed.

1.2 Present Research

The experiments at Virginia Tech will require the RBM to be spun at a rate of up to 21,000 RPM and to maintain this speed for 30 seconds. During this operating time, the rotor will be exposed to heated air (up to 300° F). Each 30 second run will be followed by a 20 to 30 minute cool down period. The extended operating time of the Virginia Tech experiments (as compared with Oxford's) will result in additional design problems such as heating of the disk and bearings.

Since the wind tunnel at Oxford is contained in externally shielded bunker, Doorly was able to design the disk with a safety factor (approximately 1.3 - 1.4 for yield)

that is unacceptably low for the Virginia Tech installation. Although Doorly's wake generator was used as a conceptual model, the differences in experimental operating conditions for the current research necessitated a unique design for the RBM. The wake generator developed at Virginia Tech is composed of: a ten-inch diameter titanium disk; sixteen titanium dovetail pieces (to retain the flexible cable bars) attached to the rim of the disk; a stainless steel shaft supported by high-speed, ceramic hybrid, angular contact bearings; a carbon steel bearing housing; a carbon steel disk housing; and a carbon steel turbine mounting housing. A cross-sectional view of the RBM is illustrated in Figure 1.3.

1.3 Thesis Objective and Contents

The purpose of this thesis is to describe some of the design and testing considerations employed in fabricating an experimental rotary device. The device required a considerable amount of analysis due to it's relatively high operating speed and unique design.

The body of this thesis describes the design of two of the more intricate RBM components, the disk and shaft. Chapter 2 covers the initial design considerations and finite element analysis applied to the fabrication of the shaft and disk. In Chapter 3, the rotordynamic analysis of the coupled shaft and disk is discussed. Next, the experimental testing procedures and results of a 23,000 RPM spin test of the RBM are presented in Chapter 4. The conclusions and recommendations for future work are examined in Chapter 5. Appendix A details the stress calculations for a preliminary disk profile. In

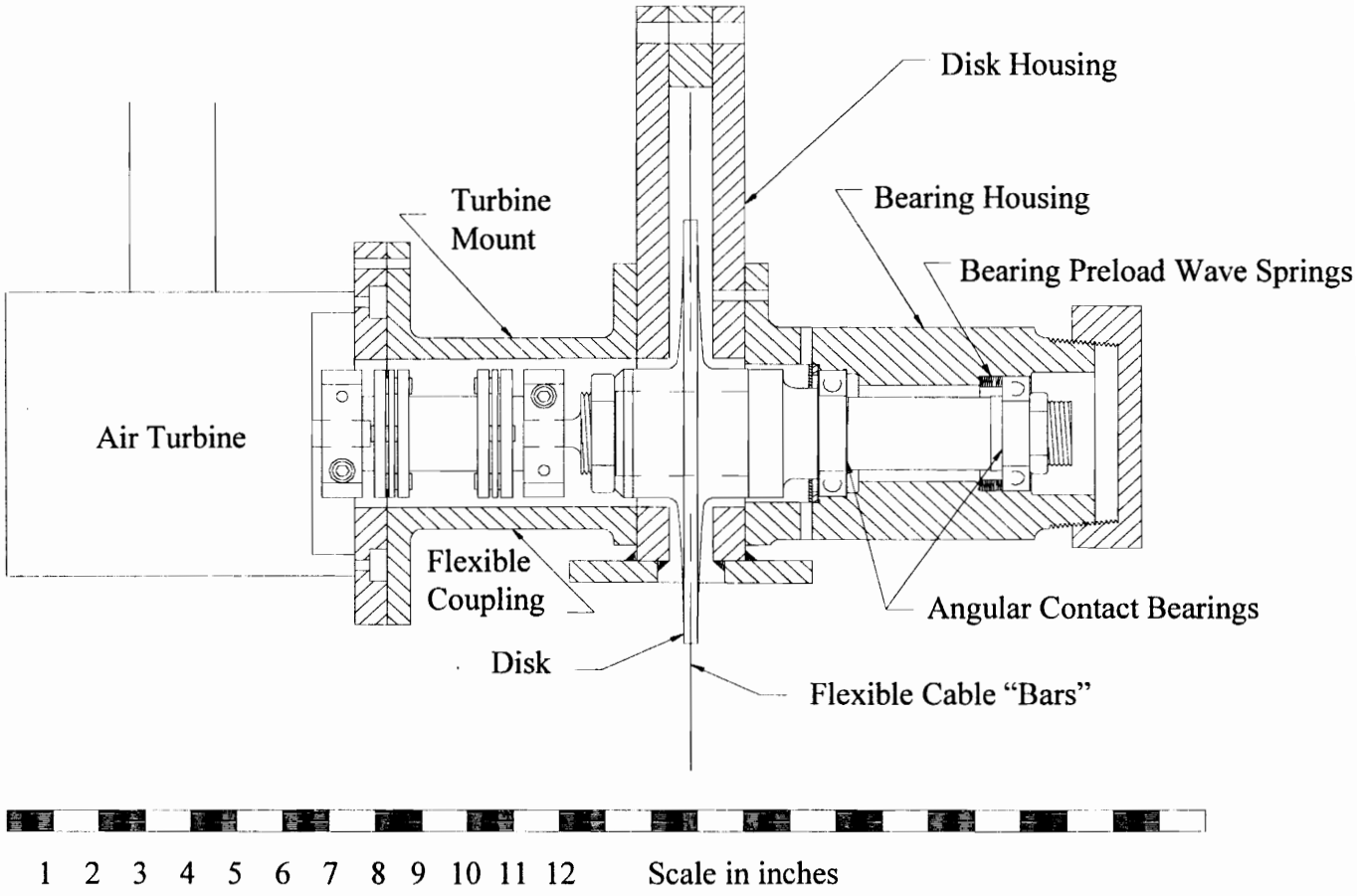

Figure 1.3: Rotating Bar Mechanism Cross Section

Appendix B, the finite element analysis of the disk, dovetail pieces, and shaft/disk coupling are presented. The critical speed program CRTSPD input and output are detailed in Appendix C. Kinetic energy estimations for the disk operating at 24,000 RPM are presented in Appendix D.

2.0 Disk and Shaft Design

The mechanical design of the disk and shaft was performed simultaneously because the two components had to be integrated for the rotor dynamic analysis. The size, mass distribution, and relative position of both components affect the critical speed of the rotor.

2.1 Disk Design

The experimental design criteria dictates that shock waves of velocity Mach 1.2 should be generated at an approximate frequency of 5600 Hz. The disk diameter was selected after considering several design parameters including: drag on the cable bars, air turbine output torque (to overcome the drag at operating speed), maximum tangential stress at the disk hub, and required operating speed to achieve the required bar-relative velocity and shock-passing frequency. Each of these factors is discussed in detail in this chapter.

2.1.1 Aerodynamic Drag on the Flexible Bars

The greatest limiting factor in the RBM design was the aerodynamic drag on the flexible cable bars. The aerodynamic drag was calculated as the sum of resistance to the bars translating through the tunnel cascade test section, the resistance to the bars translating though the disk housing, and the drag on the face of the disk. Based on the velocity triangle depicted in Figure 2.1, the drag calculation may be expressed as:

$$\text{Drag} = N_h\left(\tfrac{1}{2}C_{Dh}\,\rho dl r_m \mathbf{U}^2\right) + N_c\left(\tfrac{1}{2}C_{Dc}\,\rho dl r_m(\mathbf{V}\cos\alpha)^2\right) + D_t \qquad (2.1)$$

Equation 2.1 is based on elementary drag equations for a cylinder in cross flow.

A computer program was created to estimate the RBM speed performance based on the preceding equation. The program calculates the values of V, U, and α based on rotor speed. The drag coefficients are then curve fitted from composite curves of Mach number versus C_D for a cylinder in cross flow (Hoerner, 1965). The drag on the bars is calculated (using equation 2.1) and compared with the air turbine output torque (also curve fit). Once the drag on the bars exceeds the turbine output, the code predicts the speed reduction based on the conservation of angular momentum. Based on this code, a maximum speed of 22,500 RPM was predicted for a 5-inch radius disk with 16 3/64-inch diameter bars. The determination of the disk radius is discussed in the following section.

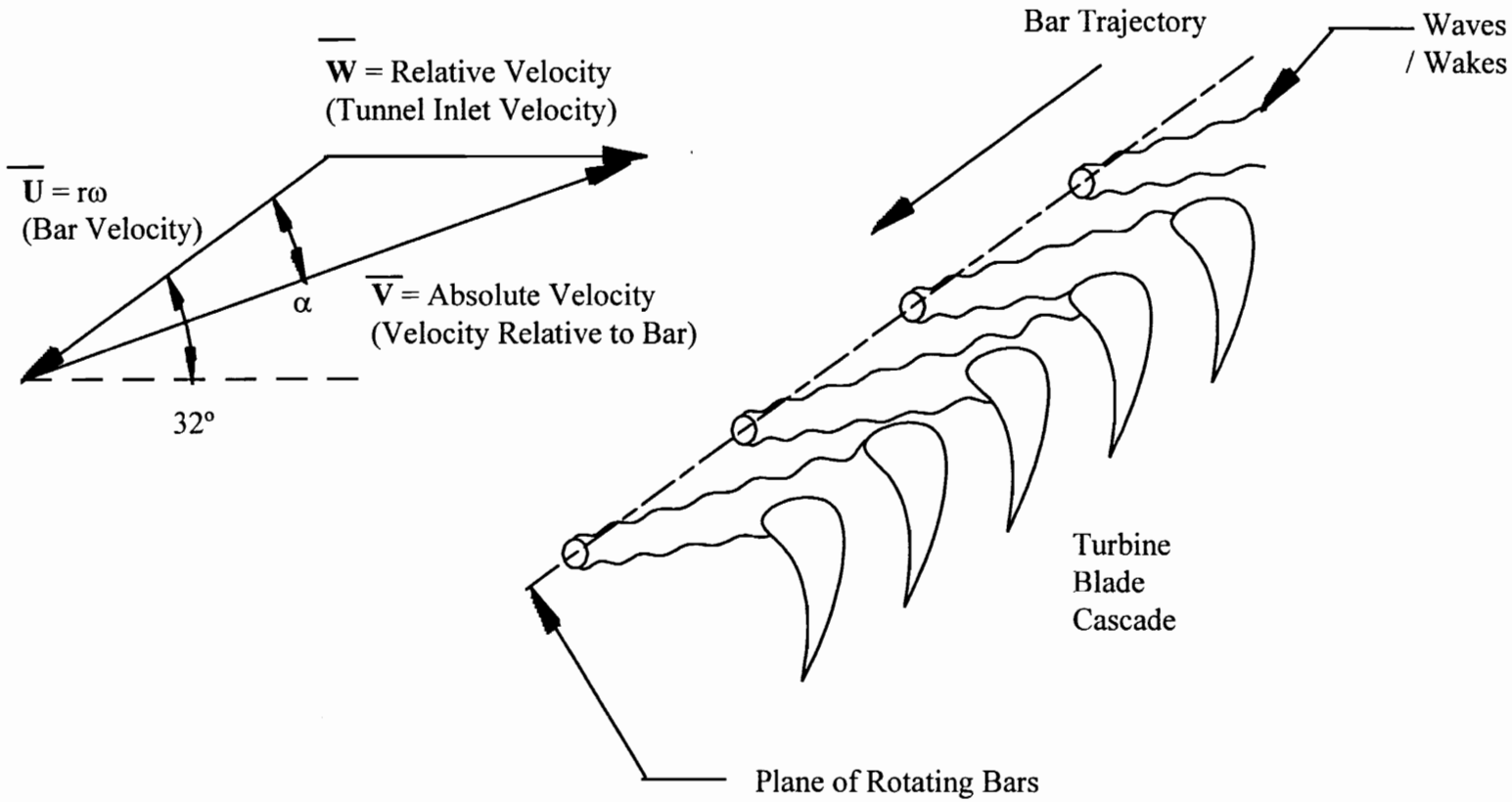

Figure 2.1: Simulation of Wave / Wake Passing In Front of a Stationary Turbine Row

2.1.2 Disk Radius Determination

The preceding drag calculation was used to find an optimum disk radius. The optimization process involved analyzing a generic disk profile with constant thickness versus varying radii. By using the constant ratios indicated in Figure 2.2, disks of radii from 3 to 10 inches were analyzed to determine the maximum aerodynamic drag on the bars and the operating speed required for a bar-passing frequency of 5600 Hz.

2.1.2.1 Disk Operating Speed

As the disk radius increases, the operating speed required to produce a constant bar-passing frequency decreases. The required operating speed was calculated for each disk radii by the following relationship.

$$\omega = U/r_m \qquad \text{and} \qquad r_m = l/2 + R_o \tag{2.2}$$

where, R_o = Disk Radius

The number of bars required to generate a constant bar-passing frequency increases with increasing disk radius. The number of bars required for each radii were calculated from the following expression:

$$N = f_B \cdot 2\pi / \omega \tag{2.3}$$

where, N = Number of bars

f_B = Bar-passing frequency

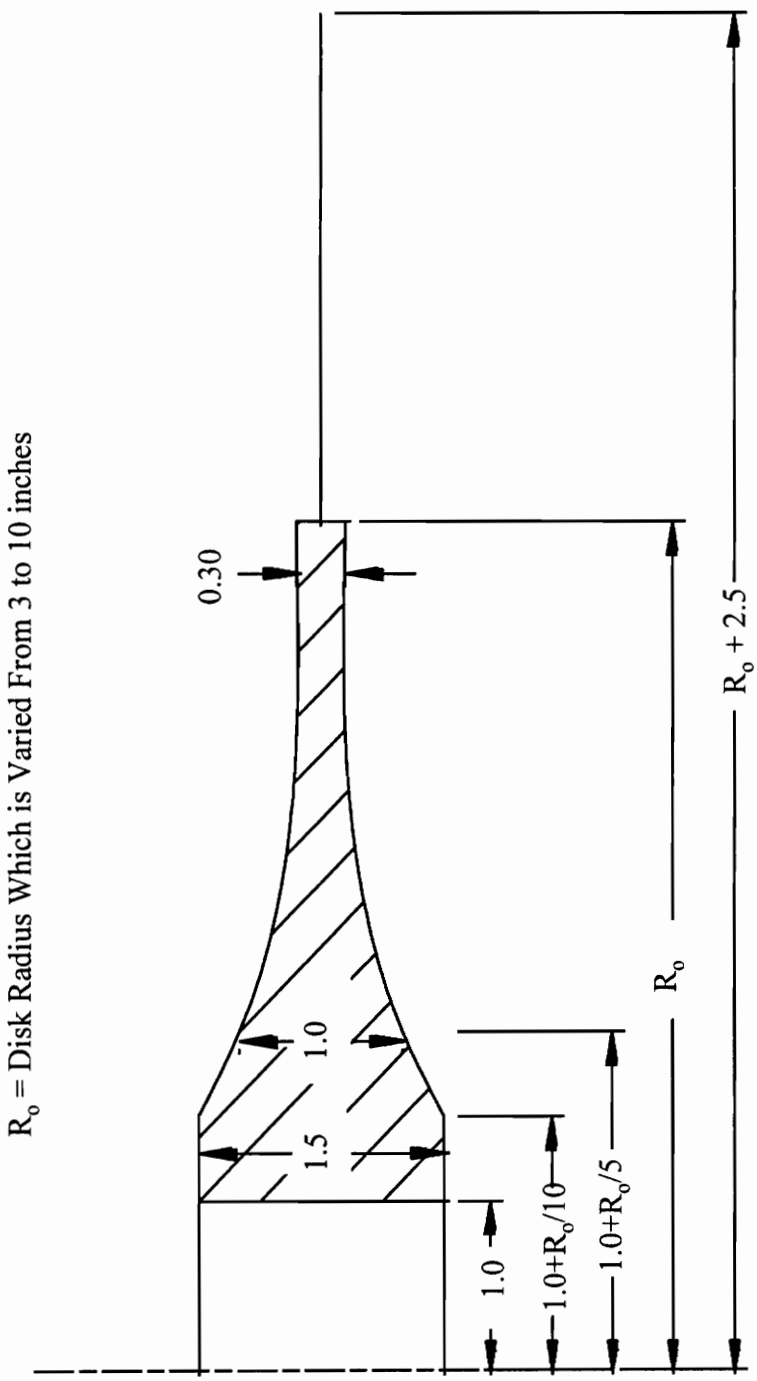

Figure 2.2: Generic Disk Profile

Experimental design dictates that the bar velocity, U, be equal to Mach 0.9 (1145 ft/s at an air temperature of 280° F). The bar-passing frequency of 5600 Hz was also imposed by experimental design. The bar length, L, was set at 2.5 inches due to geometrical constraints of the test section. Using these values with equations 2.2 and 2.3, Table 2.1 was created. The data was also used to perform drag calculations for each disk radius. The results of the drag calculations are listed in Table 2.2. Figure 2.3 contains a plot of the data from Tables 2.1 and 2.2.

Table 2.1: Operating Speed and Number of Bars versus Disk Radius

Disk Radius (inches)	Bar radius$_{cg}$ (inches)	Speed (RPM)	Number of Bars
3	4.25	30,900	11
4	5.25	25,000	13
5	6.25	21,000	16
6	7.25	18,100	18
7	8.25	15,900	21
8	9.25	14,185	23
9	10.25	12,800	26
10	11.25	11,700	28

Table 2.2: Drag on bars and Air Turbine Output versus Disk Radius

Disk Radius (Inches)	Speed (RPM)	Drag On Bars (Ft-Lbf)	*Air Turbine Output (Ft-Lbf)
3	30,900	13.67	25.03
4	25,000	19.31	29.41
5	21,000	27.33	32.17
6	18,100	35.07	34.07
7	15,900	45.62	35.46
8	14,185	55.45	36.50
9	12,800	68.58	37.32
10	11,700	80.85	37.95

* Air Turbine Output data from manufacturer's HP curves at 150 psi inlet pressure

As indicated by the chart in Figure 2.3, the maximum disk radius that could be used to sustain the RBM at the proper bar-passing frequency is 5 inches. The air turbine (Model TDI 50A-21) cannot provide adequate output torque to sustain the operating speed for any disk of larger radius. The chart also indicates that the minimum disk radius is 5 inches as any smaller disk size would require an operating speed greater than 25,000 RPM (the maximum speed rating for the flexible coupling). After establishing the disk radius at 5 inches, a stress analysis of a preliminary disk profile was performed. The next section details the stress determination.

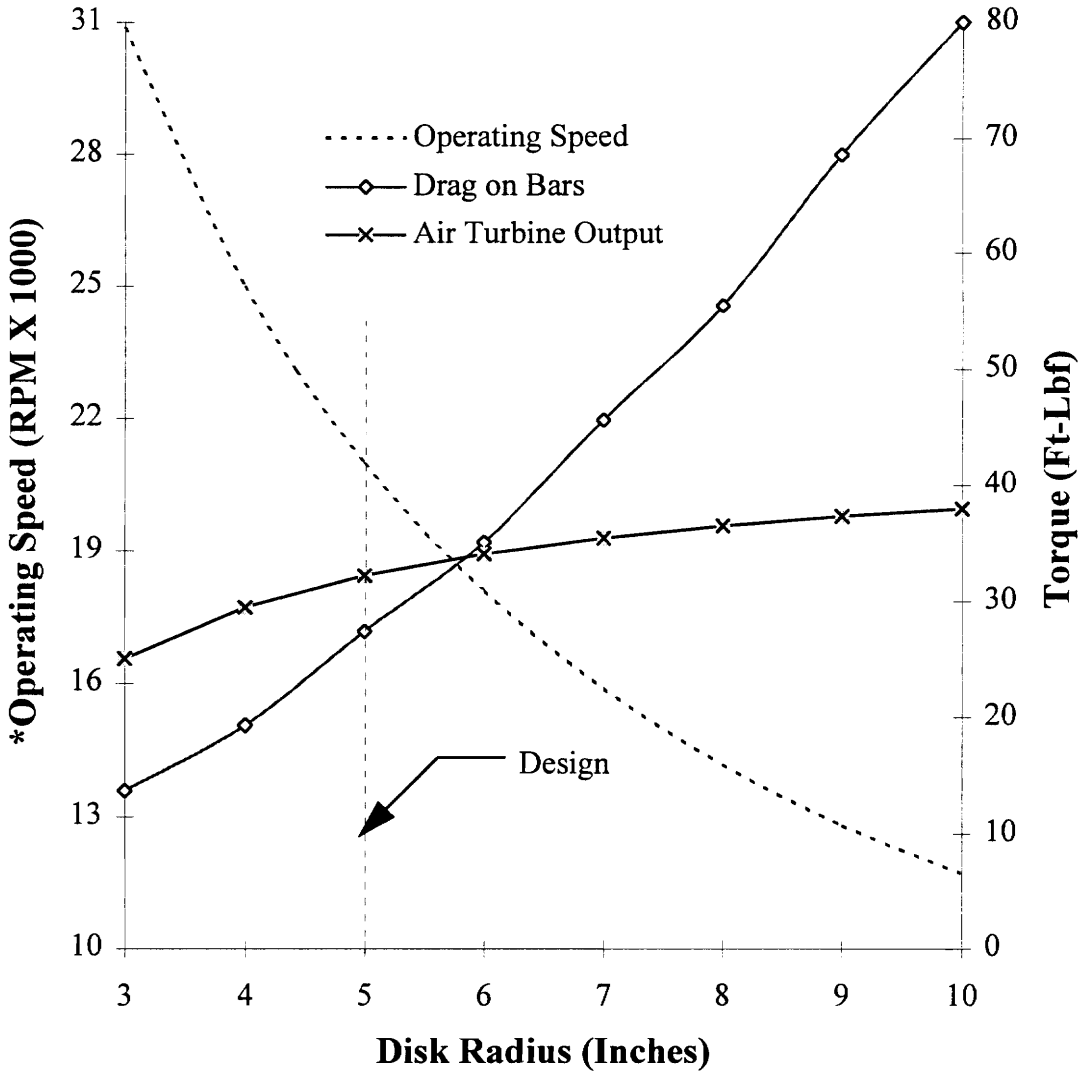

*Operating Speed Corresponds to a Bar-Passing Frequency of 5600 Hz

Figure 2.3: Operating Speed, Drag on Bars, and Output Torque vs. Disk Radius

2.1.3 Preliminary Disk Profile Design

A disk profile (similar to one depicted in Figure 2.2) was analyzed to determine the maximum radial and tangential stresses at the hub. The stress analysis was based on an approximation method outlined by Timoshenko (1976). This method replaces a contoured disk with a series of constant-thickness, concentric ring elements. The radial and tangential (uniform) stresses in the disk elements are calculated. Next, the change in stresses at the interface of elements of differing thickness is calculated. These values are used to calculate a uniform stress at the disk hub. A maximum stress of 23,700 psi was calculated for a titanium disk operating at 24,000 RPM.

Assuming the disk is attached to the shaft using axial pins, a stress concentration factor of 3 can be applied to the pin grooves in the disk. The stress concentration value was estimated by assuming the disk grooves are analogous to an infinite plate with semi-circular holes (Peterson, 1971). The adjusted stress value of 71,100 psi corresponds to a safety factor of 1.7. These calculations are described in more detail in Appendix A.

It should be noted that the approximation method outlined in this section yields an average stress value. The actual stress profile would indicate a maximum tangential stress at the center of the disk hub in excess of the average value. Therefore, the actual safety factor is lower than 1.7. After completing the preliminary stress analysis, it was decided to perform a finite element analysis in an attempt to improve the low safety factor. The next section discusses the results of the finite element analysis.

2.2 Finite Element Analysis

A finite element analysis was performed on the disk, shaft, and dovetail retaining pieces by Dr. Tibor Kiss (Virginia Tech). A full report of this analysis is included in Appendix B. The design considerations outlined in the report will be summarized in this section.

2.2.1 Flexible Cable "Bars"

Based on recommendations from the Oxford study, flexible cable bars were chosen over rigid bars. As discussed in Section 4 of Appendix B, initial calculations indicate that the moment of drag force on the bars is extremely high at the base of the bar. Rigid bars may fail if used at tunnel test conditions. However, stranded cables can withstand the drag forces due to their relatively low bending stiffness.

The flexible bars were made of 3/64", 7X7, stranded, stainless steel, aircraft cable swaged into a ball and shank fitting. The manufacturer performed a breaking test on twelve of the swaged ball and cable fittings. The minimum breaking strength of the assemblies was reported at 218 pounds. This correlates to a minimum safety factor of 2 under test conditions at 24,000 RPM. The next section details the mounting of the cable bars to the disk rim.

2.2.2 Dovetail Mounting Components

To facilitate bars of different diameters, it was decided to use interchangeable dovetail components to mount the bars to the disk rim. The titanium dovetail pieces, depicted in Figure 2.4, were designed with an internal cavity to sheath the cable bar assemblies. The cavity was designed around the dimensions of a 0.20 inch-diameter spherical ball and shank cable fitting. Since several different diameter cable assemblies use this size fitting, the dovetail retainer design allows the use of more than one size cable.

By the nature of their design, the dovetail retainers can slide out of the disk's dovetail slots only in the axial direction. Almost all of the forces acting on the rotor exist in the radial plane, except a small axial component of the aerodynamic drag on the bar (10 lb.). Operating at 24,000 RPM, the contact pressure between the dovetail retainers and the disk slot peaks at 49,000 psi. Therefore, once the rotor begins spinning, it would require a large axial force to overcome the friction forces due to the contact pressure. The dovetail pieces were retained in the mating disk slots by small stainless steel tabs, shown in Figure 2.5. The retaining tab method is widely used in the turbomachinery industry.

The profile of the dovetail components was determined through finite element analysis. A 2D axisymmetric model was constructed of the dovetail retainer and disk using plane stress elements. The results of the analysis indicate a maximum von Mises

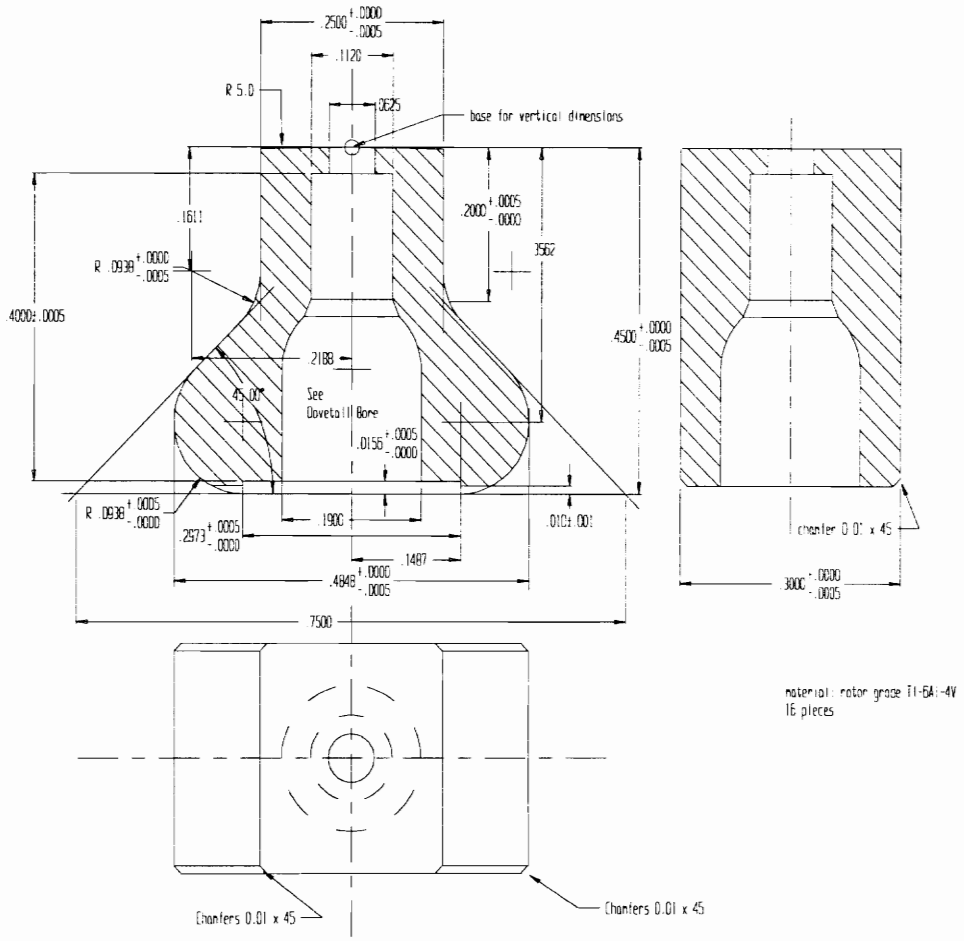

Figure 2.4: Dovetail Retaining Component

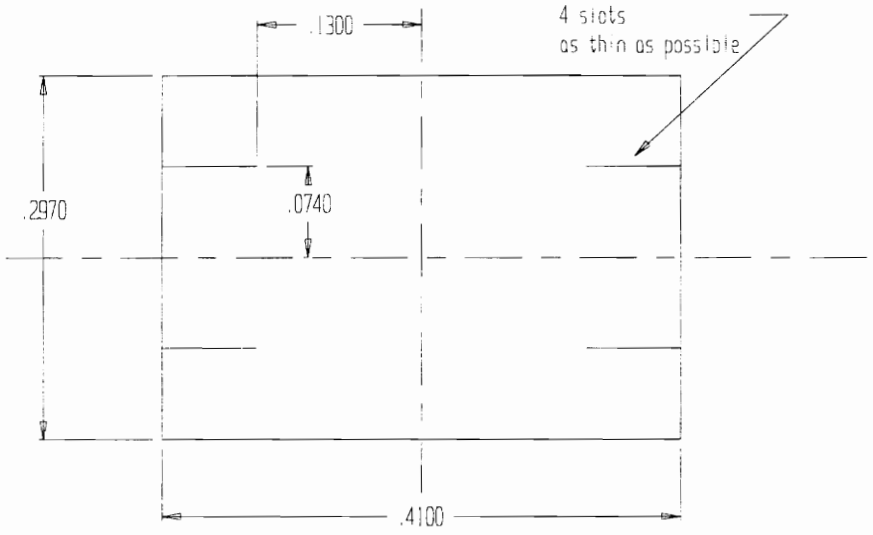

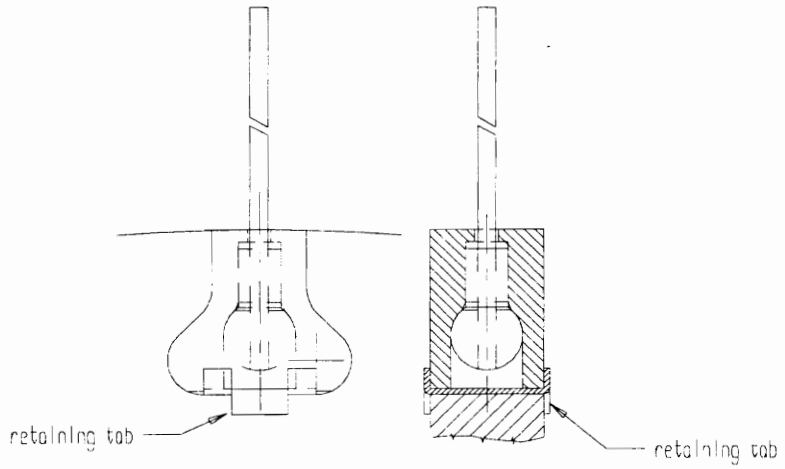

Figure 2.5: Dovetail Retaining Tab

stress of 48,990 psi (safety factor of 2.4) for the dovetail component. The analysis is discussed in further detail in Appendix B-G.

2.2.3 Final Disk Profile Design

The initial disk profile discussed in section 2.1.3 was used as starting point in the finite element analysis. The hub length was increased after initial calculations suggested that radial growth of the hub could be greatly reduced by using a 2.5 inch long hub. The radial growth of the 2.5 inch hub can be offset with a slight interference fit.

However, the actual shaft coupling method involves using 6 axial pins to retain the disk and does not rely on the inference fit. Utilizing the elongated hub length, it was possible to design the disk such that the pin grooves were cut only in the outer edges of the hub. The 3/8 inch long pin grooves were cut on both edges of the disk hub (see Figures 2.6 and 2.7). Based on a 2D axisymmetric finite element model (see Appendix B-F), the maximum von Mises stress in the pin groove region is 13,050 psi versus the maximum stress of 32,658 psi at the hub center. Based on the hub center value, a safety factor of 3.67 was calculated for the disk.

A stress concentration factor for the axial retaining pins was determined with two separate 2D axisymmetric models. The models were used to determine stress concentration due to centrifugal loading and stress concentration due to torque transfer at the hub. The analysis revealed a maximum stress concentration factor of 1.7 for the

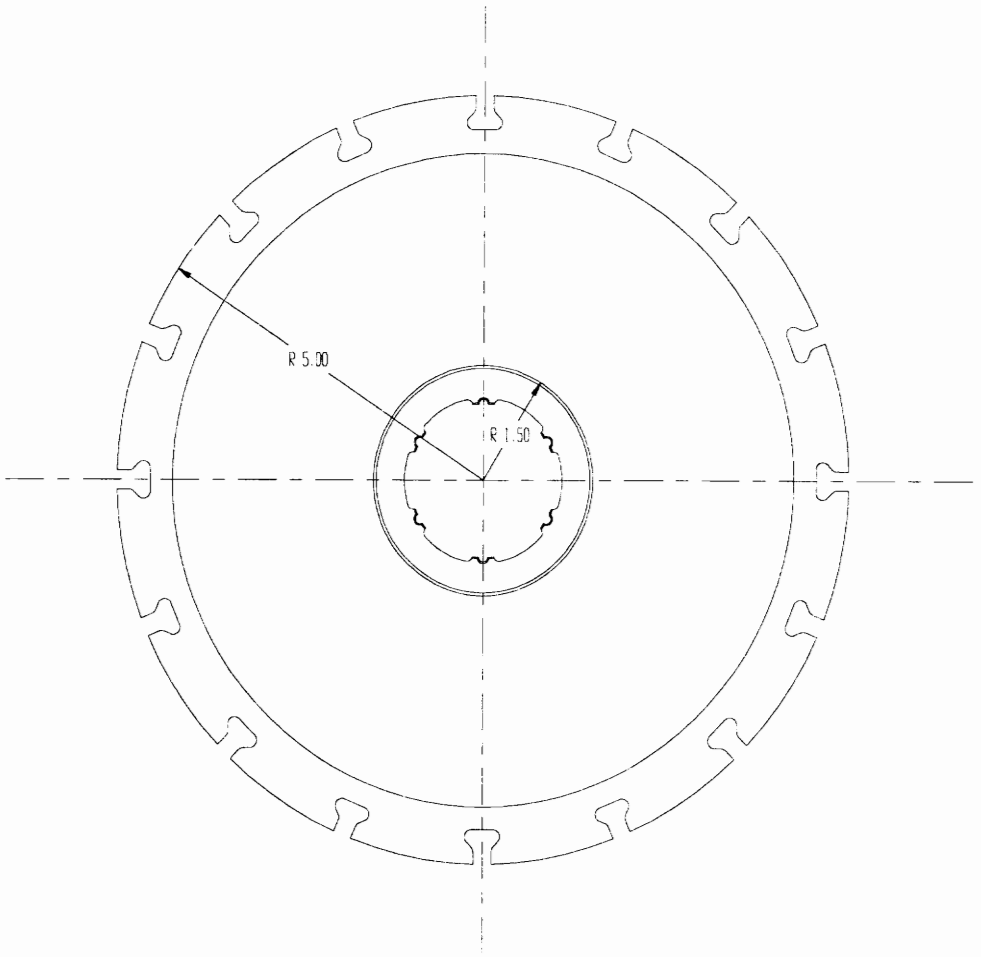

Figure 2.6: Axial View of Titanium 6AL-4V Disk

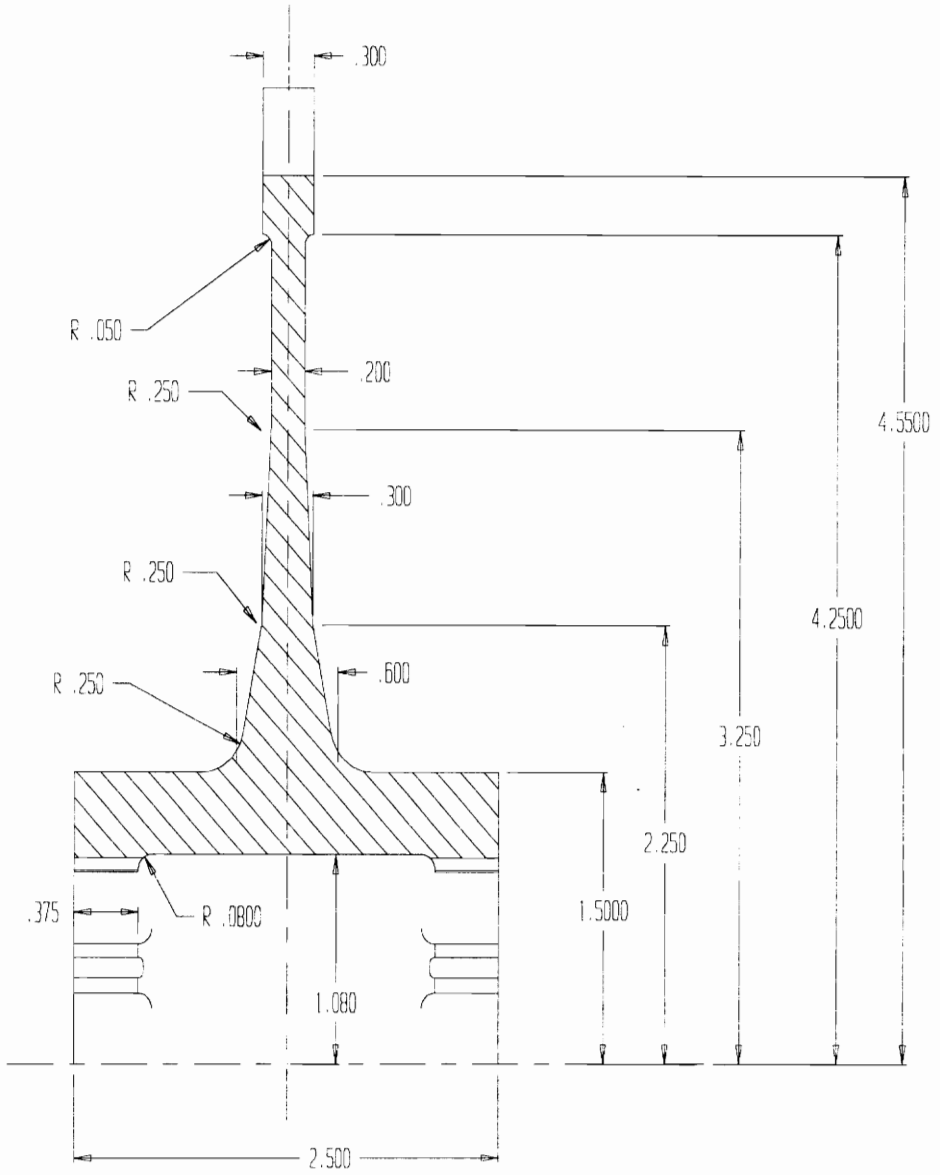

Figure 2.7: Radial Cross Section of Disk

models. Based on this value, a safety factor of 5.36 was calculated for the pin grooves. The models are discussed in further detail in Appendices B-H and B-I.

The rotor developed at Oxford was very similar in design to the generic disk profile displayed in Figure 2.2. The Oxford rotor was secured to the shaft with axial pins that extended the entire length of the hub. The stress concentration factor for this design was determined to 2.875 by finite element modeling. Using Doorly's reported maximum disk stress of approximately 30,000 psi and the stress concentration factor, a safety factor of 1.4 can be estimated for the Oxford design. The unique pinning method of the Virginia Tech rotor more than doubled the overall disk safety factor of the Oxford design.

2.3 Shaft Design

The main design goal was to maximize the shaft diameter in an attempt to minimize the effects of any rotor imbalance. The first step in the shaft design was to select angular contact ball bearings suitable for testing conditions. The largest bearings capable of operating at 24,000 RPM with a grease lubricant have a 45 mm bore. A grease lubricant was chosen to avoid the possible contamination of the wind tunnel test section. An oil lubricant in the pressurized wind tunnel could by-pass the labyrinth seal of the bearing housing and invade the test section.

After determining the shaft outer diameter dimensions imposed by the bearings and the disk, the shaft length was optimized using rotordynamic analysis. The analysis is discussed in Chapter 3.

The vast majority of shaft loading is due to the aerodynamic drag on the bars and the air turbine (torsional loading). A small axial aerodynamic drag component (1.14 lb. as calculated in Appendix B-C) also exists. In addition, there is a 50 lb. tension load between the bearings. Neglecting the small axial loads, a safety factor was calculated for the maximum torsional loading in the following manner:

$$\tau_{xy} = \frac{16T}{\pi d^3}$$

where, τ_{xy} = torsional stress

T = torsional moment

d = shaft diameter

For the case of a shaft subjected to pure torsion, the von Mises stress is calculated as

$$\sigma' = \sqrt{3\tau_{xy}^2}$$

and the safety factor is calculated as

$$\text{Safety Factor} = \text{Yield Strength} / \sigma'. \qquad (2.4)$$

The minimum shaft safety factor of 4.35 was calculated using equation 2.4 and the following conditions:

T	= 504 in-lbf	(maximum air turbine output torque)
d	= 0.625 inches	(minimum shaft diameter)
Yield	= 95,000 psi	(annealed stainless steel 432)

The safety factor was adjusted by a stress concentration factor of 1.2. The stress concentration factor was estimated from charts (Peterson) for a shaft under torsional loading. This stress concentration occurs at Fillet 1 as shown in the shaft diagram of Figure 2.8

A picture of the shaft is included in Figure 2.9. A picture of the RBM rotor (shaft, disk, dovetail retaining components, and cable bars) is included in Figure 2.10.

2.4 RBM Operating Life

A fatigue analysis was not performed on the RBM since the device will be used a limited number of times. The proposed testing schedule involves operating the mechanism less than 500 times (30-40 seconds per run). The RBM rotor will be disassembled and inspected for stress fractures approximately once every 50 runs.

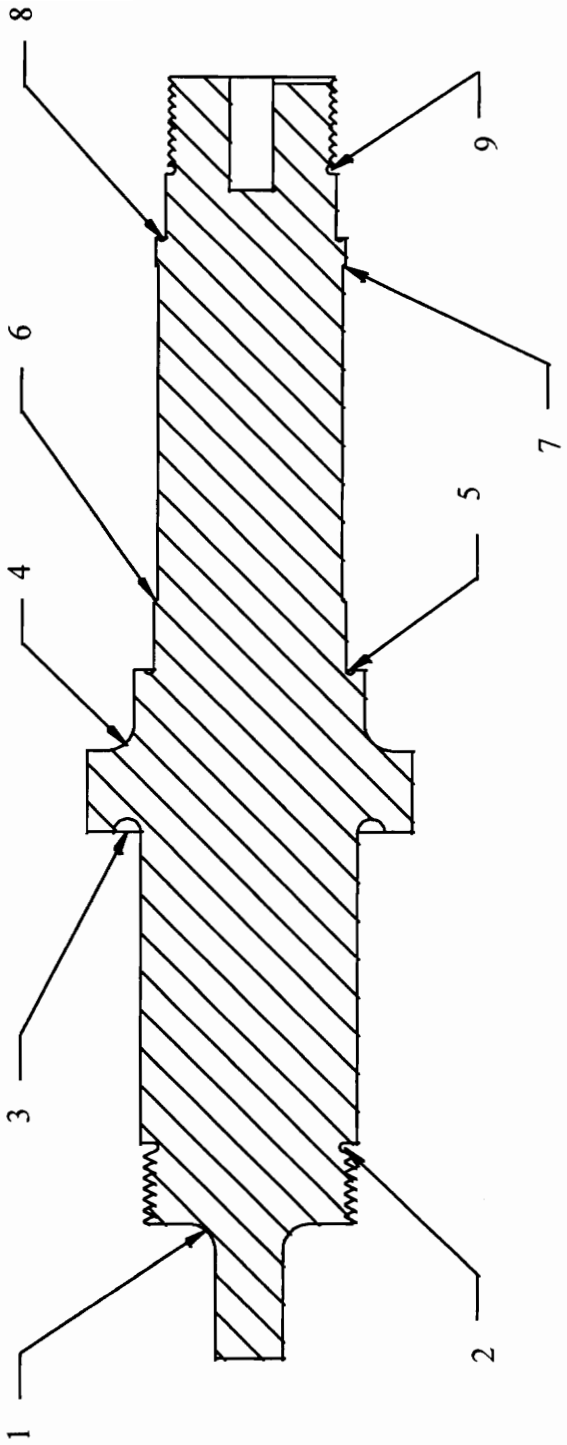

Figure 2.8: Shaft Cross Section Showing Fillet Locations

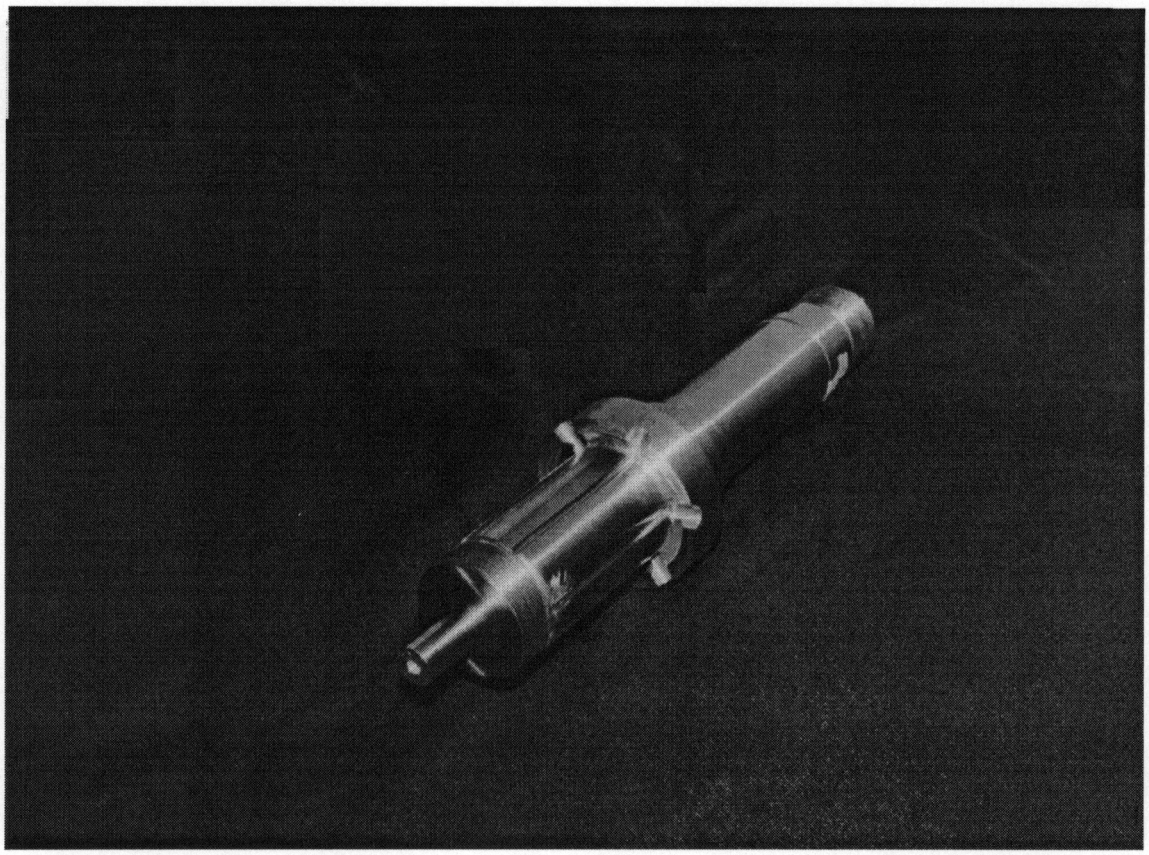

Figure 2.9: Annealed 432 Stainless Steel Shaft

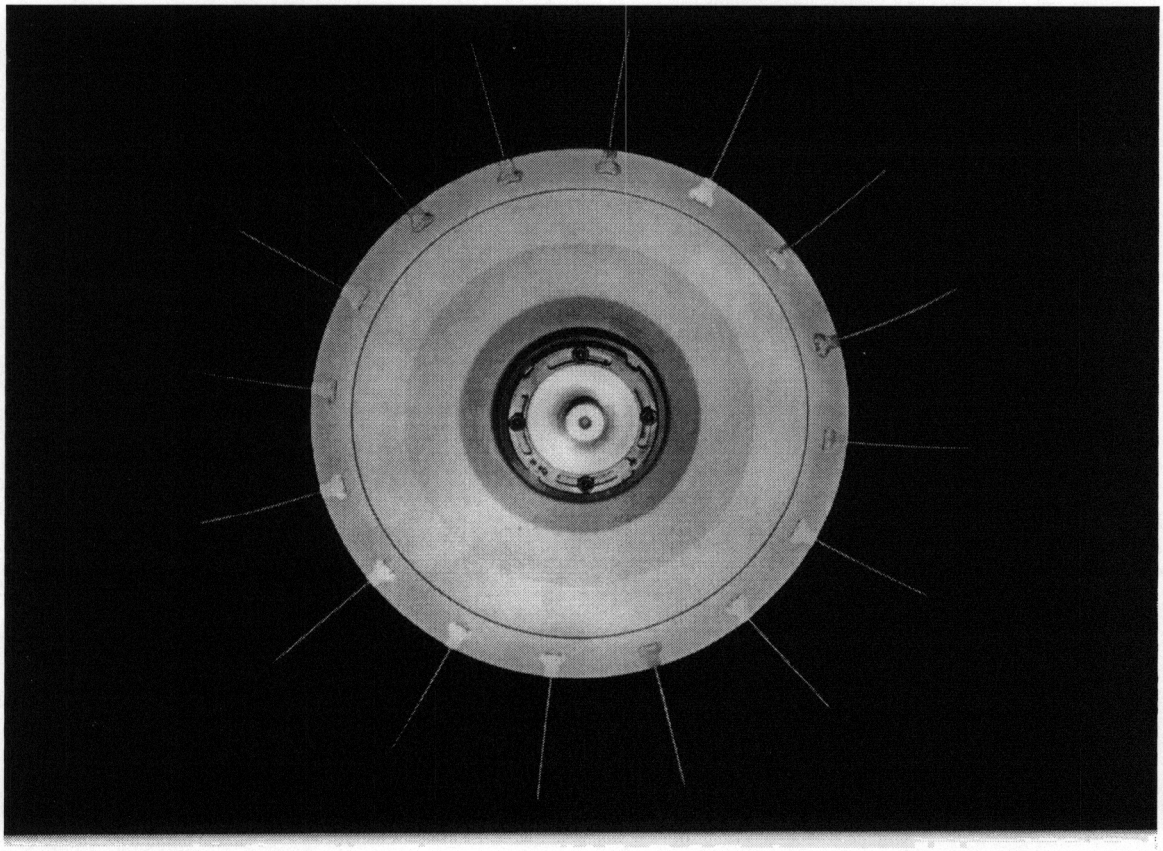

Figure 2.10: Axial View of RBM Rotor

3.0 Rotordynamic Study

A rotordynamic analysis of the disk and shaft was performed using a computer program supplied by Dr. R. G. Kirk of Virginia Tech. The program, CRTSPD, is based on the transfer matrix method for computing natural bending critical speeds of shafts. The general equations for the transfer matrix method, taken from Rao (1991), are discussed in the next section.

3.1 Transfer Matrix Method

The rotor is replaced by a series of lumped masses connected by massless, flexible beam elements. Breaking the rotor into n sections, there are n lumped masses and n cantilever beam elements. Figure 3.1 (a) depicts a simplified model of the RBM rotor with accompanying station points used to indicate where the mass elements occur. The simplified rotor is portrayed as a series of mass and beam elements in Figure 3.1 (b).

At each mass element, 1 through n, equations of state are calculated at points immediately preceding and immediately following the lumped mass (designated as S_L and S_R, respectively). These equations are vectors containing the shear force, applied moment, displacement, and slope (Q, M, δ, and θ, respectively). The equations of state

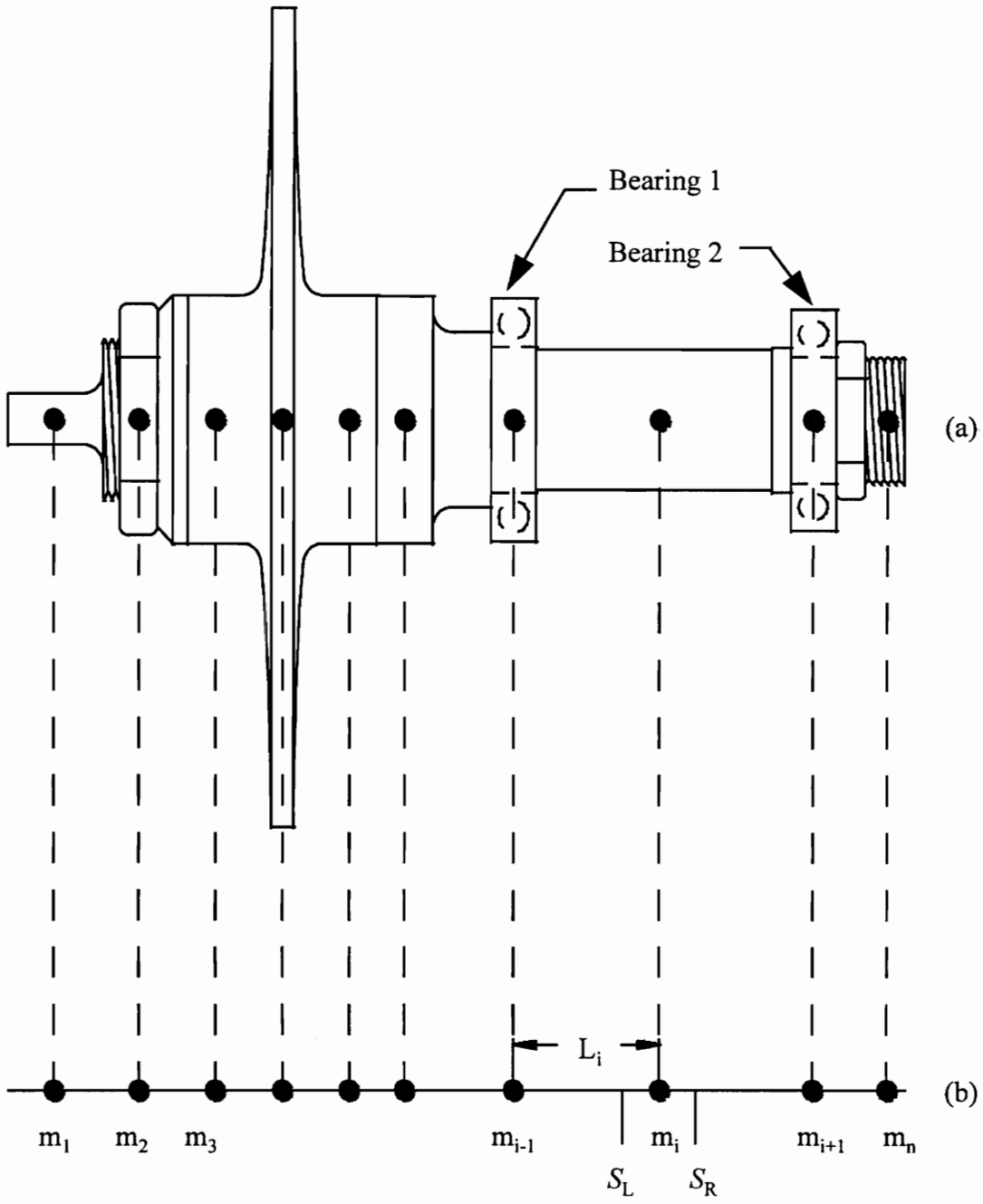

Figure 3.1: Simplified Transfer Matrix Method Rotor Model

are illustrated at the *i*th element of the series in Figure 3.1 (b). The equations for the mass element are expressed in the following form:

$$
\begin{aligned}
Q_i^L &= Q_{i-1}^R \\
M_i^L &= M_{i-1}^R + Q_i^L \bullet L_i \\
\theta_i^L &= \theta_{i-1}^R + M_{i-1}^R \bullet \frac{L_i}{EI_i} + Q_{i-1}^R \bullet \frac{L_i^2}{2EI_i} \\
\delta_i^L &= \delta_{i-1}^R - \theta_{i-1}^R \bullet L_i - M_{i-1}^R \bullet \frac{L_i^2}{2EI_i} - Q_{i-1}^R \bullet \frac{L_i^3}{6EI_i}
\end{aligned}
\tag{3.1}
$$

where the relationships for deflection δ and slope θ are derived from cantilever beam equations,

$$
\begin{aligned}
\delta &= -\frac{ML^2}{2EI} + \frac{QL^3}{3EI} \\
\theta &= \frac{ML}{EI} - \frac{QL^2}{2EI}
\end{aligned}
\tag{3.2}
$$

These relationships are plotted for the *i*-1th and *i*th lumped masses in Figure 3.2.

Equations 3.1 define the massless shaft segment reactions. When written in the following matrix form, these equations form the field transfer matrix.

$$
\begin{Bmatrix} -\delta \\ \theta \\ M \\ Q \end{Bmatrix}_i^L = \begin{bmatrix} 1 & L & \frac{L^2}{2EI} & \frac{L^3}{6EI} \\ 0 & 1 & \frac{L}{EI} & \frac{L^2}{2EI} \\ 0 & 0 & 1 & L \\ 0 & 0 & 0 & 1 \end{bmatrix}_i \begin{Bmatrix} -\delta \\ \theta \\ M \\ Q \end{Bmatrix}_{i-1}^R \tag{3.3}
$$

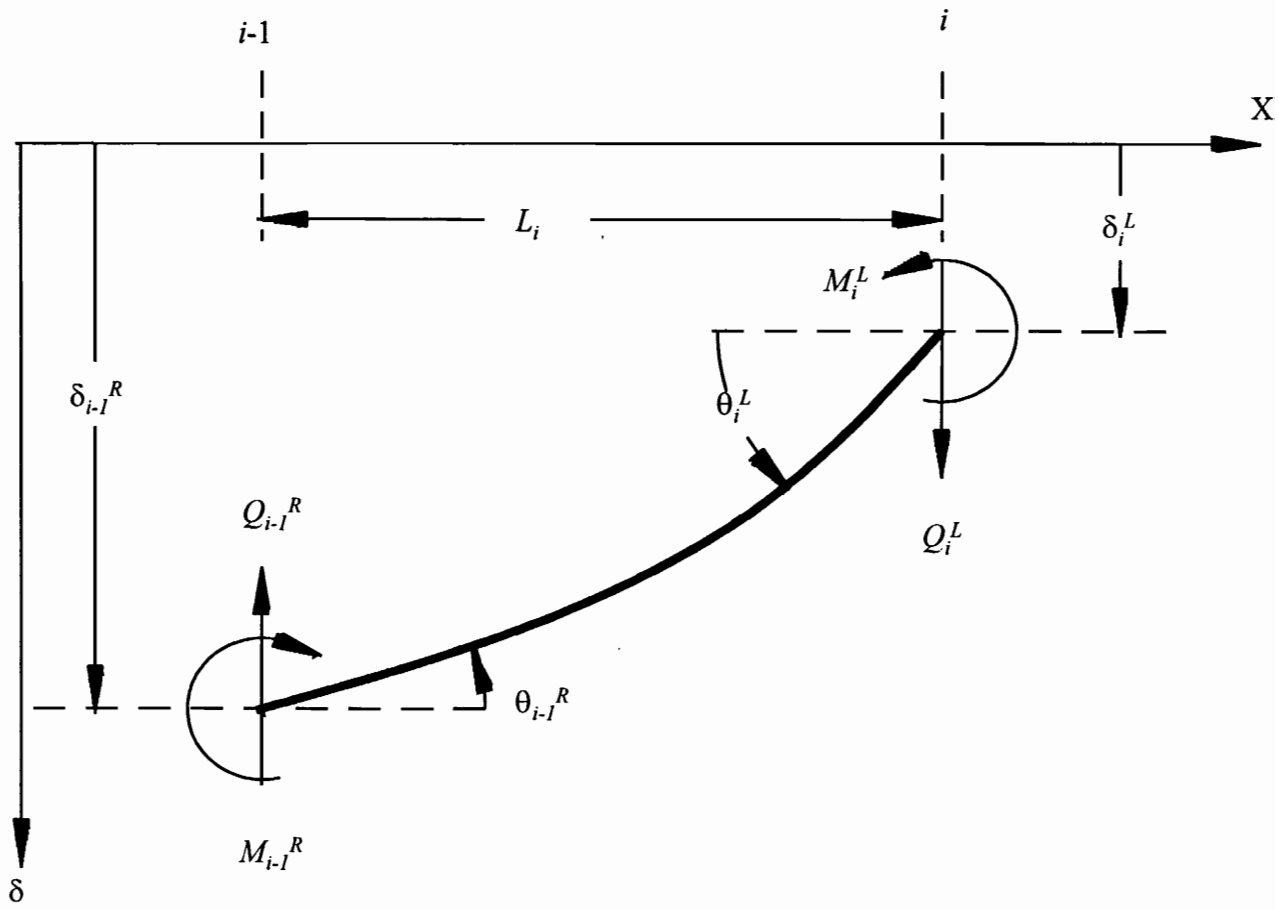

Figure 3.2: Field Transfer Matrix Model

The set of equations that define the reactions of the lumped masses form the point transfer matrix. The relationships between the equations are illustrated in Figure 3.3. These equations may be expressed in the following form

$$\begin{aligned} Q_i^R &= Q_i^L - \delta_i^L \bullet m \bullet p^2 \\ M_i^R &= M_i^L \\ \theta_i^R &= \theta_i^L \\ \delta_i^R &= \delta_i^L \end{aligned} \tag{3.4}$$

where m is the lumped mass and p is the vibrating frequency of the mass. Equations 3.3 form the point mass transfer matrix when expressed in the following form:

$$\begin{Bmatrix} -\delta \\ \theta \\ M \\ Q \end{Bmatrix}_i^R = \begin{bmatrix} 1 & 0 & 0 & 0 \\ 0 & 1 & 0 & 0 \\ 0 & 0 & 1 & 0 \\ mp^2 & 0 & 0 & 1 \end{bmatrix}_i \begin{Bmatrix} -\delta \\ \theta \\ M \\ Q \end{Bmatrix}_i^L \tag{3.5}$$

The computer code uses the transfer matrices listed in Equations 3.3 and 3.5 to progress across the rotor, from left to right, calculating Q, M, θ, and δ at each section. The product of all field matrices and point matrices is then calculated in the following manner.

$$\begin{aligned} \{S\}_1^L &= [F]_1 \{S\}_0 \\ \{S\}_1^R &= [P]_1 \{S\}_1^L = [P]_1 [F]_1 \{S\}_0 \\ \{S\}_2^L &= [F]_2 \{S\}_1^R = [F]_2 [P]_1 [F]_1 \{S\}_0 \\ &\cdots \cdots \cdots \cdots \cdots \cdots \cdots \cdots \cdots \\ \{S\}_{n+1} &= [F]_{n+1} \{S\}_n^R = [F]_{n+1} [P]_n [F]_n [P]_{n-1} \cdots [F]_1 \{S\}_0 \end{aligned} \tag{3.6}$$

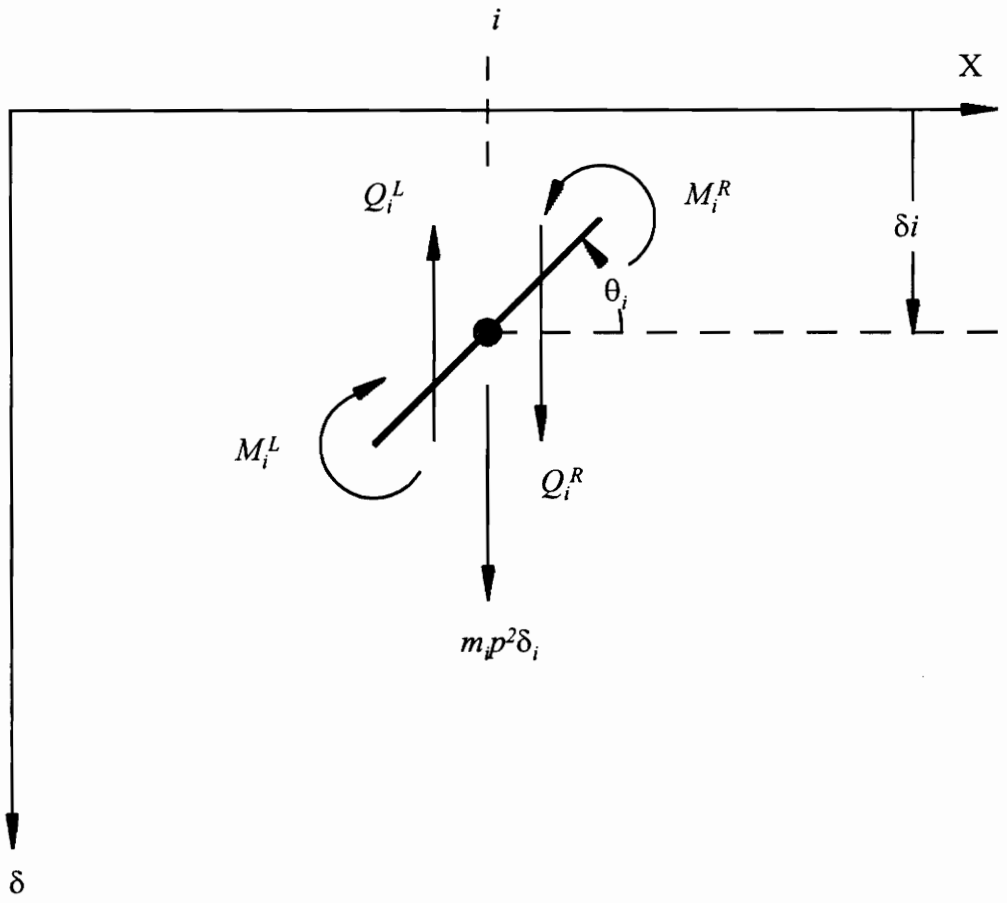

Figure 3.3: Point Transfer Matrix Model

The last matrix relationship in equation 3.6 may be written as,

$$\{S\}_{n+1} = [U]\{S\}_o \tag{3.7}$$

where, $\{S\}$ is the state vector and $[U]$ is the overall transfer matrix (product of all field matrices and point matrices). Equation 3.7 may be expanded as,

$$\begin{Bmatrix} -\delta \\ \theta \\ M \\ Q \end{Bmatrix}_{n+1} = \begin{bmatrix} u_{11} & u_{12} & u_{13} & u_{14} \\ u_{21} & u_{22} & u_{23} & u_{24} \\ u_{31} & u_{32} & u_{33} & u_{34} \\ u_{41} & u_{42} & u_{43} & u_{44} \end{bmatrix} \begin{Bmatrix} -\delta \\ \theta \\ M \\ Q \end{Bmatrix}_0 \tag{3.8}$$

Imposing boundary conditions of M=0 and Q=0 at stations 0 and n+1, the following determinate is obtained from Equation 3.8.

$$\Delta = \begin{vmatrix} u_{31} & u_{32} \\ u_{41} & u_{42} \end{vmatrix} = 0 \tag{3.9}$$

A root searching method is then used to determine the natural frequency value that satisfies Equation 3.9. Assuming a unit deflection at station 0, it is possible to define the value of θ at that station. The normalized mode shape is then determined by defining the value of δ at each station 1 to n. The bearing stiffness is incorporated in the model by modifying the shear load, Q, at the bearing supports.

3.2 CRTSPD Rotor Model

The RBM rotor, bearings, and flexible coupling were modeled to determine the critical speeds for the RBM. The rotordynamics of the driving air turbine play an

important role in the critical speed estimation of the system. Unfortunately, the required rotordynamic information for the turbine is not available from the manufacturer.

One method to compensate for the lack of turbine design data involves dividing the system into two separate entities at the mid-point of the flexible coupling. This method ("half-mass approximation") assumes that the turbine can the support half of the mass effects of the coupling and remain rotordynamically stable through the operating speed range. After making this assumption, only the rotor and half of the flexible coupling need to be modeled. For modeling purposes, the mass effects of the coupling half are concentrated at the end of the shaft. After creating the model with the appropriate geometry and mass effects, the next step is to determine the system bearing stiffness.

The bearing stiffness is a function of operating speed and bearing preload force. A plot of bearing stiffness versus operating speed and preload force is displayed in Figure 3.4. The forward bearing (Bearing 1 in Figure 3.1) is a 45 mm bore, angular contact bearing. The rear bearing (Bearing 2 in Figure 3.1) is a 40 mm bore, ceramic hybrid, angular contact bearing. Both bearings are lubricated with a high-speed grease.

The computer code is able to calculate system natural frequencies at only one stiffness value for each bearing. Therefore, it is necessary to run several cases with different bearing stiffness values to create a critical speed map. The results of the rotordynamic analysis are discussed in the following section.

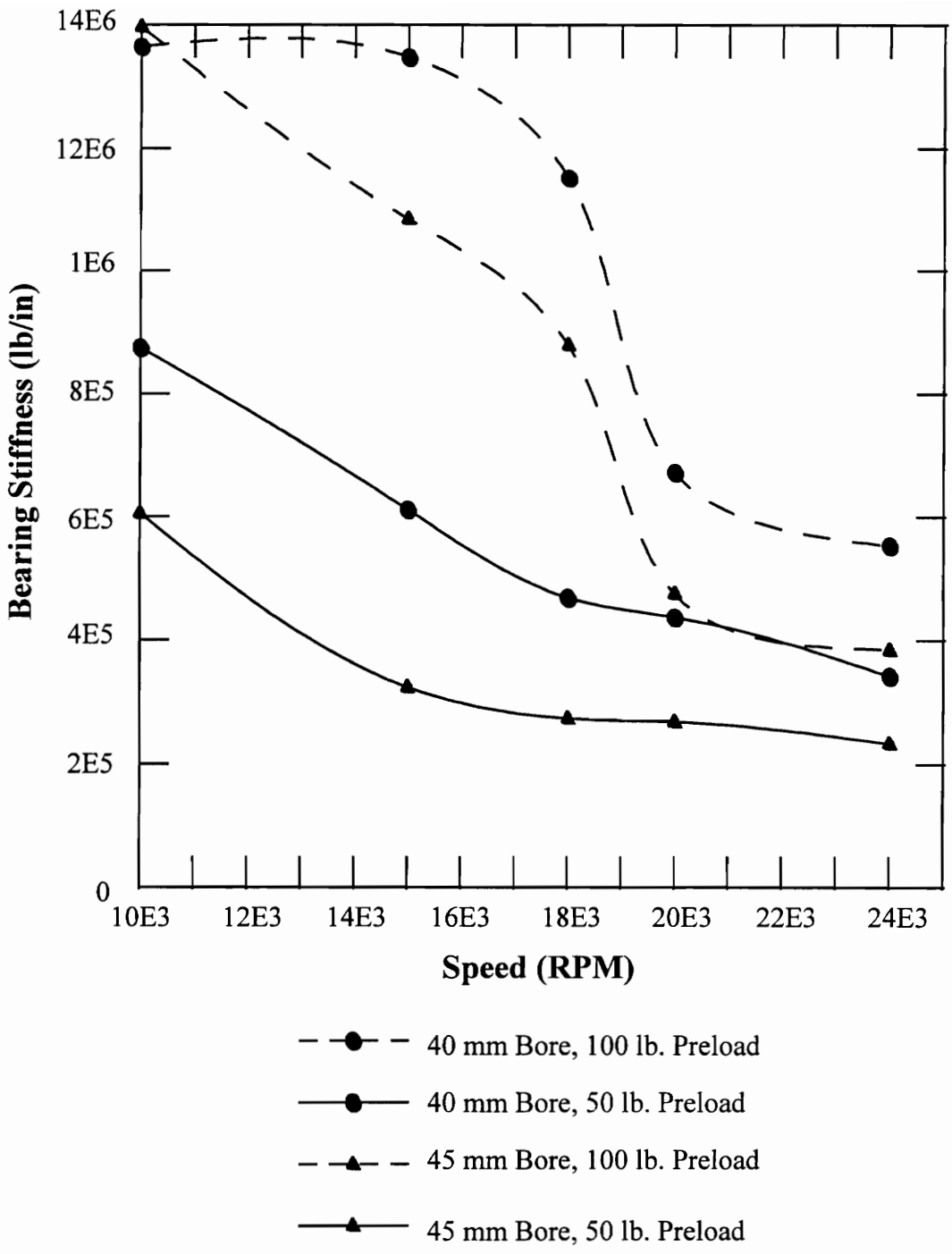

Figure 3.4: Bearing Stiffness versus Operating Speed

3.3 Rotordynamic Design

Sensitivity cases were run to determine the overall shaft length and system critical speeds. Using the bearing manufacturer's suggested preload of 50 - 75 lbs., it was not possible to design a rotor with the first critical speed above the operating speed (21,000 RPM). After determining this limitation, it was decided to design the rotor with the first critical speed at approximately 75% of the operating speed. This design places the operating speed half-way between the first and second integer multiples of the critical speed. It is necessary to avoid operating at any integer multiple of the critical speed since adverse vibrations can occur at any of these speed multiples.

The final shaft design was obtained using a 50 pound bearing preload and an overall shaft length of 11.875 inches (bearing spacing of 4 inches). System critical speeds were generated by running 9 bearing stiffness cases with the CRTSPD code. A critical speed map was generated in Figure 3.5 by overlaying the natural frequencies on the bearing stiffness curve (Figure 3.4). Based on the map, a critical speed of 14,000 RPM was estimated for the system. It should be noted that only the first critical speeds were plotted in Figure 3.5. The second critical speed profile did not intersect the bearing stiffness curves in the speed range of interest.

The mode shapes for the first and second critical speeds are illustrated in Figure 3.6. The mode shapes indicate the typical rigid shaft response of synchronous whirl orbits. The response at the first critical speed is a conical whirl. And the second critical speed induces a translatory whirl response. The whirl orbits will be used to estimate

vibration levels for the RBM in Chapter 4. The program input and output are listed in Appendix C.

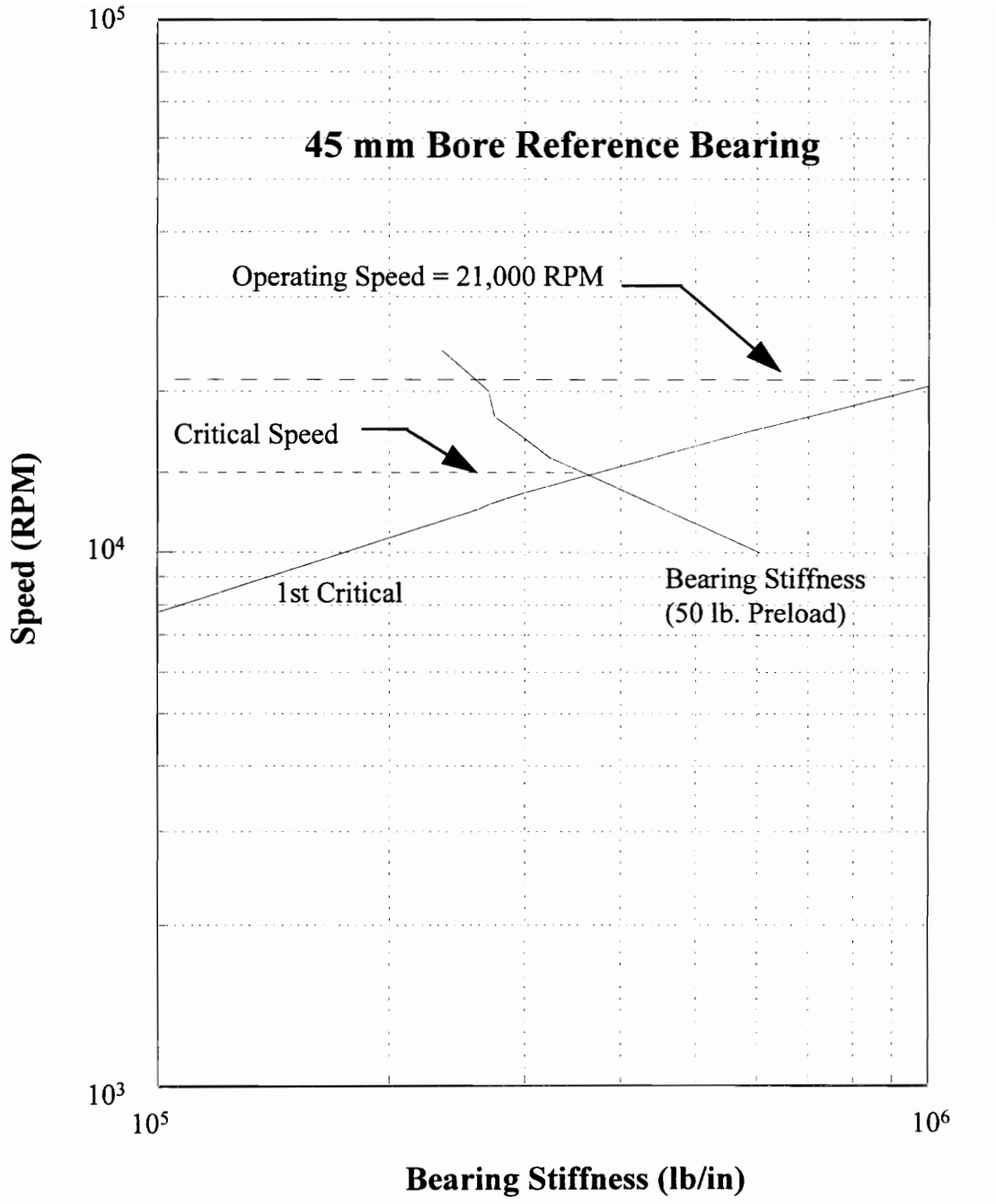

Figure 3.5: Critical Speed Map

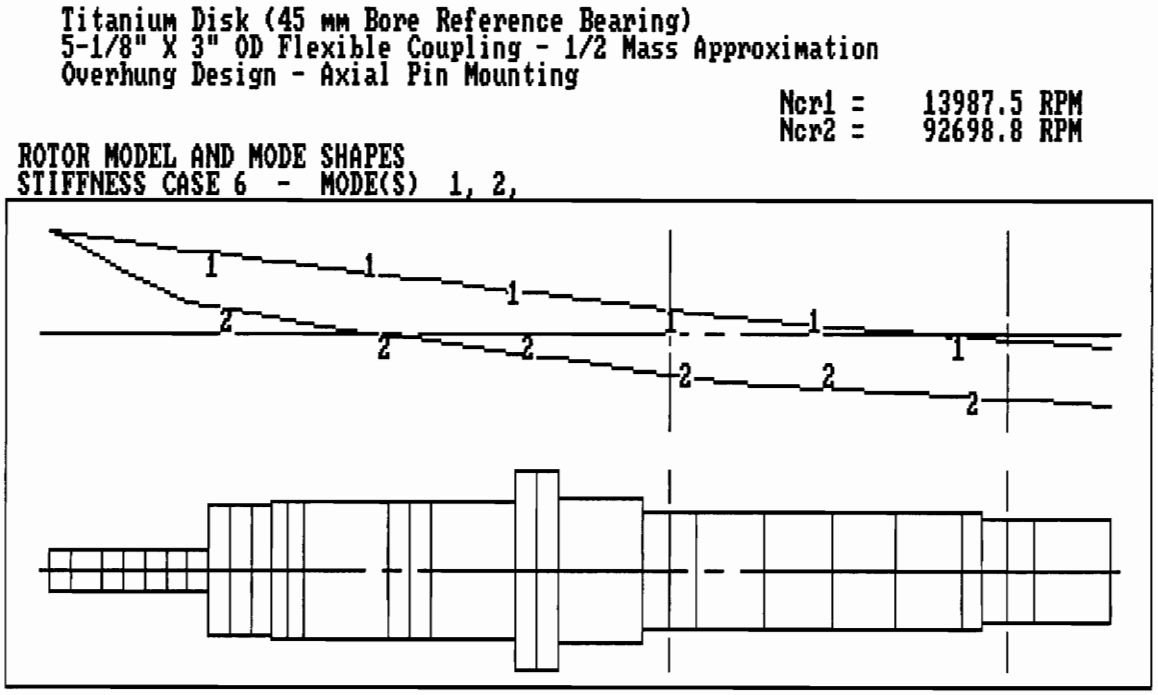

Figure 3.6: Mode Shapes for Reference Bearing Stiffness of 360,000 lb/in (Graphic Output from CRTSPD Program)

4.0 Testing of Rotating Bar Mechanism

This chapter details the post-fabrication inspections and spin tests performed on the RBM. The purpose of the spin tests was to validate the RBM design and to determine if the device was suitable for further testing prior to installation in the wind tunnel.

4.1 Post-Fabrication Inspection

Prior to assembling the RBM components, the disk and shaft were inspected using X-rays and penetrant invasion methods. The tests revealed that there were no flaws or stress fractures in either component. After the post-fabrication inspection, the rotor (disk, shaft, dovetail retaining pieces, and flexible cable assemblies) was assembled. The rotor was then balanced by Test Devices, Inc. using a high-speed balancing machine. The rotor was balanced as a Grade G 0.4 rigid rotor (maximum acceptable residual unbalance / unit mass $\approx$ 0.125 g•mm/kg at 24,000 RPM) as suggested by Muster and Flores (1969).

After being balanced, the rotor was subjected to an overspeed test. The rotor was tested to 27,000 RPM (approximately 130% of wind tunnel operating speed) in an evacuated spin pit. The vibration levels were recorded through the operating speed range. The results indicated that the rotor did not pass through any critical speeds.

4.2 Full-Speed RBM Test

After the overspeed test, the rotor was assembled with the rest of the RBM. It was decided to perform a full-speed test of the RBM with all of the components, including the driving air turbine, in the spin pit. The main goal of the test was to verify the equipment design by ensuring that the RBM could be accelerated to wind tunnel testing speeds and decelerated without incident. The parameters being tested included maximum rotational speed, bearing heating, and vibration levels.

It would be desirable to duplicate the actual tunnel operating conditions in the spin pit to determine a baseline case for later comparison with tunnel runs. However, the cross flow from the wind tunnel and the structural dampening of the tunnel foundation could not be duplicated in the spin pit. It was decided to perform a "worst case scenario" for the test with the expectation that the RBM would perform better under actual tunnel operating conditions.

To achieve worst case conditions, the test design involved creating drag on the bars in excess of those values encountered in tunnel operating conditions. The increased drag would be generated by increasing the fluid density in the pit to 0.14 lbm/ft^3 (using argon at room temperature and 20 psia). This represents a 20% increase in drag over tunnel operating conditions. The bearing heating parameter was worsened by extended running times. The test design called for running times of up to 3 minutes (versus 30 - 40 seconds for the tunnel tests). The vibration levels were augmented by using a rigid foundation to mount the RBM to the spin pit lid. The vibration levels were monitored

using an accelerometer. Since the RBM accelerates through the first critical speed, it was important to verify the predicted natural frequency and to monitor the reaction of the RBM at this frequency.

The test was performed to the maximum attainable speed of the RBM in an inert gas. The test required modifying a spin pit at Test Devices, Inc. to allow air inlet and exhaust hoses for the driving air turbine. The RBM was attached to an angle iron test stand, depicted in Figure 4.1. The test stand was then suspended from the spin pit lid via 4-1/2 inch bolts. A 2 inch NPT flexible hose (used for air turbine intake) and a 4 inch NPT pipe (air turbine exhaust) was run through the spin pit lid. Wires for the monitoring equipment were also run through the lid. The speed, bearing temperature, and vibration levels (accelerometer) were monitored during the tests. The air turbine was operated with a compressor capable of producing 2500 SCFM at 125 psi. Due to the modifications in the spin pit lid, it was not possible to pressurize the pit.

4.2.1 Test Results

Five runs were performed with the RBM in the spin pit. Prior to the testing, the air in the pit was displaced with argon. Test Devices, Inc. required that the pit be filled with an inert gas in the event of a structural failure in the RBM. Argon was selected as the inert gas because it's density (0.105 lbm/ft^3) is approximately the same as that of air at wind tunnel operating conditions. The first two runs involved accelerating the RBM to 5000 RPM for 30 seconds. These runs were used primarily to ensure that all monitoring

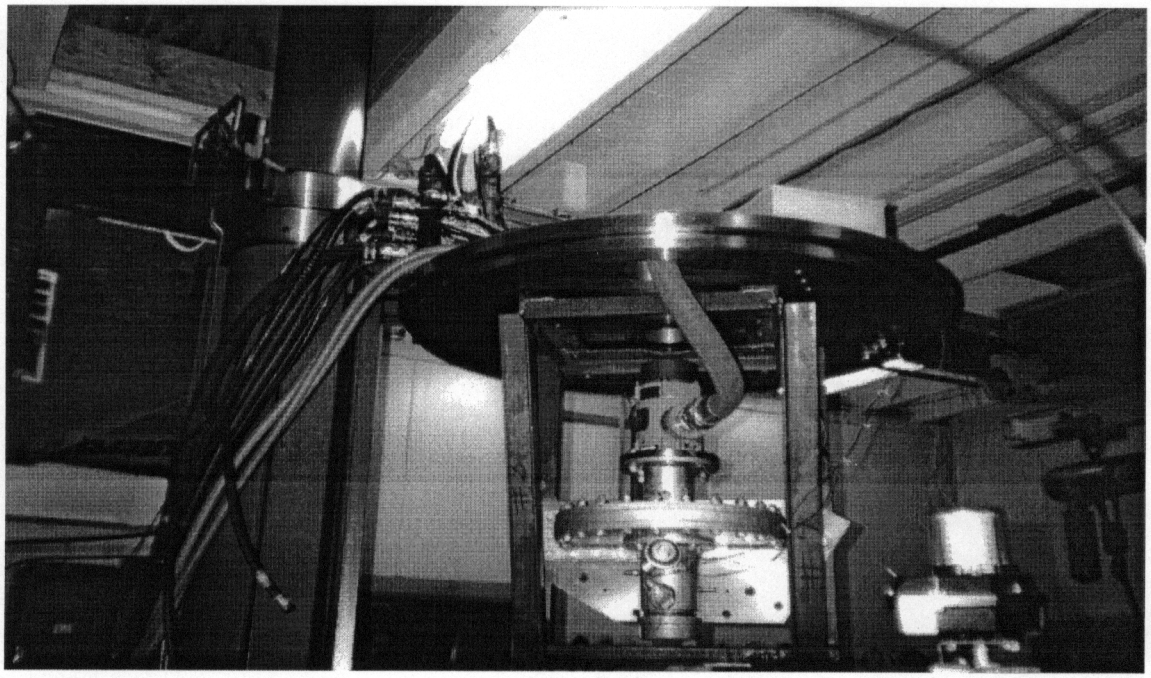

Figure 4.1 (a): RBM Mounted to Spin Pit Lid - Front View

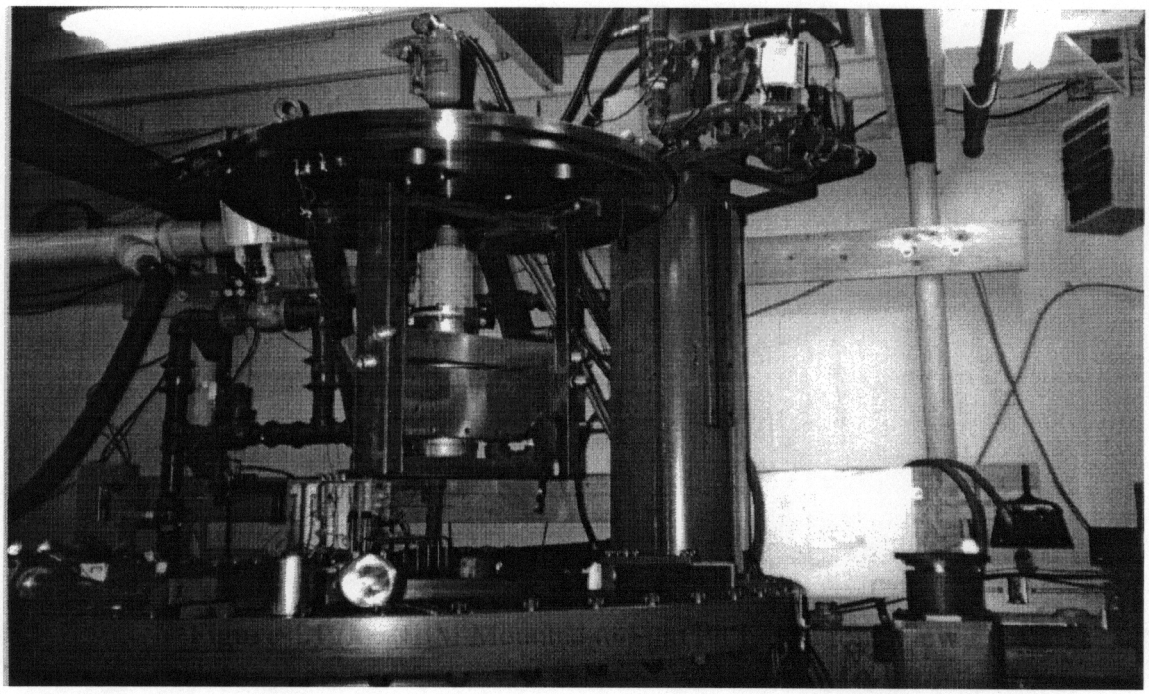

Figure 4.1 (b): RBM Mounted to Spin Pit Lid - Rear View

equipment was operating properly. During the first proving run, it was discovered that the accelerometer output signal was incompatible with Test Devices, Inc.'s signal analyzer. The accelerometer output was observed with an oscilloscope for all proving runs. The results of the last three tests are summarized in the following table:

Table 4.1: Spin Test Results

			Accelerometer Output	
Test Number	Test Duration	Bearing Temp. Increase	Speed Range (RPM)	Maximum P-P Acceleration
3	3 Minutes	13.2 °F	0-12,000 12,000-15,000 15,000-21,000	2g 8g 1.5g
4	3 Minutes	18.0 °F	0-12,000 12,000-15,000 15,000-23,000	2g 8g 1.5g
5	2 Minutes	9.1 °F	0-12,000 12,000-15,000 15,000-23,000	2g 8g 1.5g

One of the major goals of the spin test was to confirm the predicted critical speed of 14,000 RPM. During the testing, the RBM was accelerated rapidly through the speed range of 12,000 - 15,000 RPM. The accelerometer output peaked sharply around 14,000 RPM, confirming the critical speed estimate.

Due to mechanical problems, it was not possible to integrate the accelerometer output with a signal analyzer (to determine vibration levels). However, vibration estimates can be made using the maximum peak-to-peak acceleration levels and the accompanying rotational speeds. It is then possible to compare these levels with

published vibrational severity charts to determine if the RBM is operating within acceptable limits.

It is necessary to assume a synchronous whirl orbit at all speeds to begin the vibration level estimate. As indicated in Chapter 3, the mode shapes from the rotordynamic analysis suggest synchronous whirl orbits at the first and second critical speeds. The velocity can then be estimated using the following kinematic equation for circular motion,

$$a = v \bullet \omega \tag{4.1}$$

where, a = acceleration and ω = frequency. At the wind tunnel operating speed of 21,000 RPM, the RBM has an estimated peak vibration level of 0.132 in/s. A peak vibration level less than 0.16 in/s is satisfactory under the guidelines of the Erskine vibration severity chart (Ehrich, 1992). This chart is based on casing vibration levels for a wide variety of rotating machines.

4.2.2 Predicted Versus Actual Performance

Based on aerodynamic drag calculations discussed in Chapter 2, the RBM's performance was predicted and compared with the actual test data in Run 4. The comparison is plotted in Figure 4.2. The predicted speed data was forced to match the actual test data until the maximum predicted speed (22,500 RPM) was reached. The close agreement between the actual and predicted speeds suggests that almost all of the power consumption of the RBM is attributable to the drag on the bars.

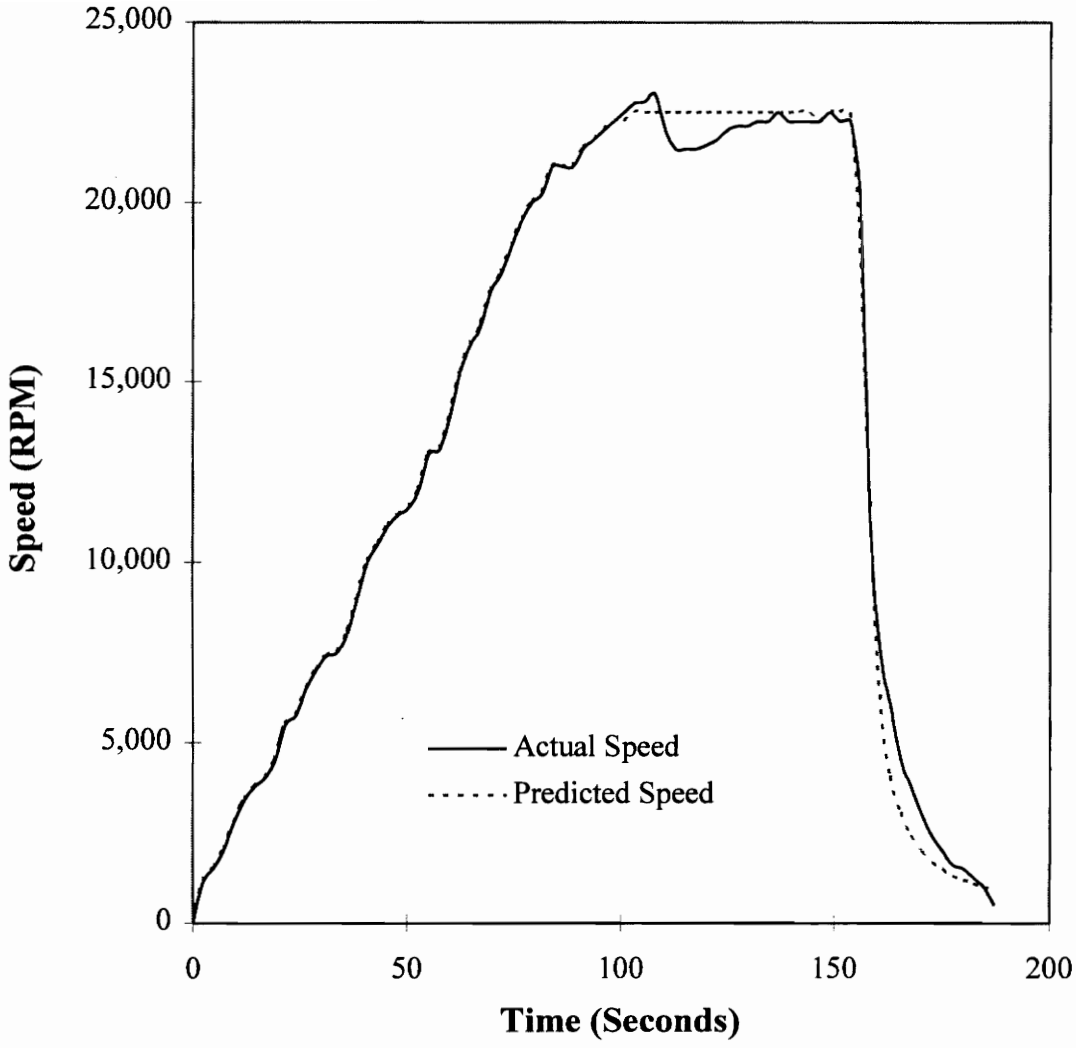

Figure 4.2 Actual vs. Predicted Speed of RBM in Argon (Data from Run 4)

As previously indicated, the computer code reduces the predicted speed of the RBM (based on conservation of angular momentum) if the drag on the bars exceeds the turbine output torque. The inertia of the disk is used to offset the speed decay resulting from the drag on the bars. The close agreement between the predicted and actual speeds after shut-down (approximately 155 seconds in Figure 4.2 plot) suggests that angular momentum assumptions are correct.

5.0 Conclusions and Recommendations

The purpose of this thesis was to describe some of the design features involved in creating a unique rotating bar mechanism capable of being operated at wind tunnel testing conditions. The body of this work detailed the stress analysis and rotordynamic analysis of a high-speed rotor. The design was verified through a series of tests. The results of a "worst case scenario" spin test were presented.

The final design of the RBM was similar to the rotary device developed and successfully operated at Oxford University. Where applicable, improvements over the device designed at Oxford were discussed.

The specific conclusions resulting from this research are:

1. The RBM can successfully be accelerated to an operating speed of 21,000 RPM and decelerated without adverse effects.
2. The RBM exhibits satisfactory vibration levels at the operating speed.
3. The speed prediction program created to estimate the maximum speed of the RBM was validated.

4. The unique disk/shaft mounting used in the RBM rotor more than doubled the disk safety factor (as compared with the Oxford design).
5. Heating of the bearings during operation of the RBM is not excessive.
6. Additional testing of the RBM is required to obtain a base line set of operating parameters (prior to installing the RBM in the wind tunnel).

After examination of the results from the spin test, the following recommendations are made for further research:

1. Consider replacing the existing disk with a composite material disk to reduce the kinetic energy.
2. If bars of larger diameter are to be used in the future, it will be necessary to reduce the drag of the bars passing through the disk housing by narrowing the disk housing passage.
3. Test the RBM at expected wind tunnel operating temperatures (approximately 150° F) to determine the additional effects of bearing heating.

Appendix A: Disk Stress Calculations

The initial disk profile was determined using a stress analysis method outlined by Timoshenko (1976). This method is an approximation based on replacing the actual disk profile with a series of uniform disk elements. First, the stresses in each of the uniform disk elements are calculated in the following manner:

$$\sigma_r = A + \frac{B}{r^2} - \beta_1 \omega^2 r^2$$
$$\sigma_t = A - \frac{B}{r^2} - \beta \omega^2 r^2 \qquad \text{(A.1)}$$

where,

$$\beta_1 = \frac{\gamma}{g}\frac{3+\mu}{8}; \qquad \beta = \frac{\gamma}{g}\frac{1+3\mu}{8}$$

and A and B are constants of integration. By using the following transformation,

$$s = \sigma_r + \beta_1 \omega^2 r^2,$$
$$t = \sigma_t + \beta \omega^2 r^2 \qquad \text{(A.2)}$$
$$w = 1/r^2$$

equations A.1 become

$$s=A+Bw; \qquad t=A-Bw \tag{A.3}$$

If the values of s and t are known at any point on the disk element, their values may be calculated for any other point on the disk element. This may be accomplished by setting A equal to the average of the known values of s and t and calculating the value of B. When viewed in graphic form, equations A.3 are represented as straight lines with a point of intersection at s,t = A and w = 0. The lines have a slope of ± B. Equations A.3 are plotted in Figure A.1.

Next, the change in radial and tangential stresses at the interface of elements of differing thickness must be calculated. Assuming the thickness changes from y to y + Δy at the interface, the change in radial stress, $\Delta\sigma_r$ may be represented by the following equation

$$\sigma_r y = (\sigma_r + \Delta\sigma_r)(y + \Delta y)$$

assuming the stresses are uniformly distributed over the disk, $\Delta\sigma_r$ may be found as

$$\Delta\sigma_r = -\frac{\Delta y}{y + \Delta y}\sigma_r \tag{A.4}$$

The change in tangential stress is based on the unit strain condition that circumferential displacement for a stress element be equal to the radial displacement for the same element, therefore

$$\epsilon_t = u / r$$

and,

$$\Delta\sigma_t = \mu\Delta\sigma_r. \tag{A.5}$$

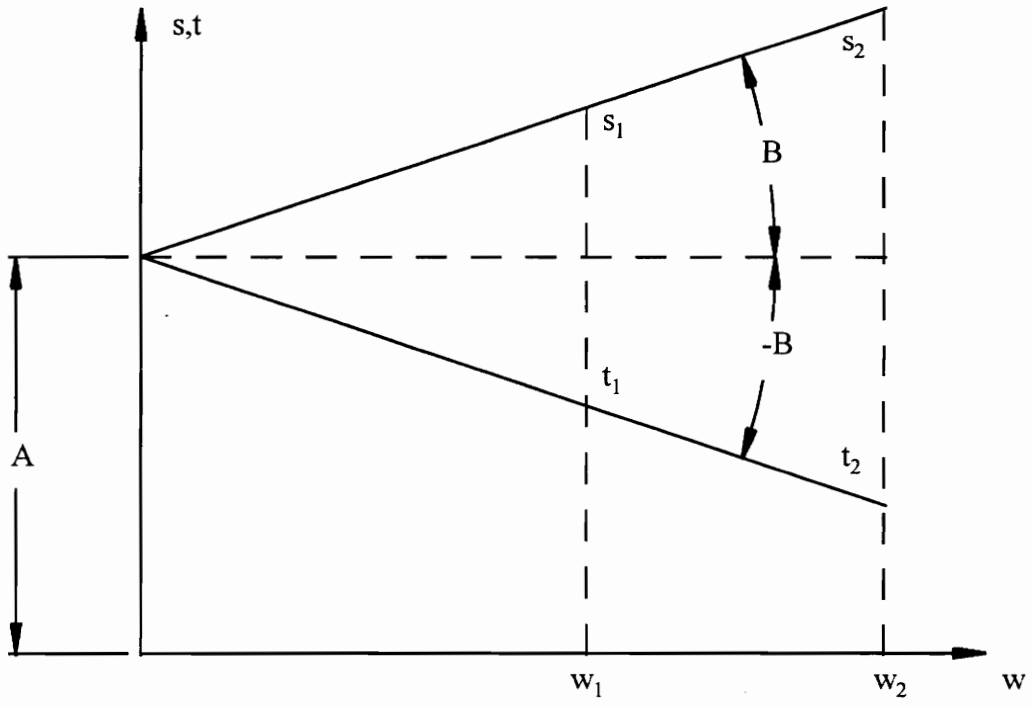

Figure A.1: Graphic View of Equations A.3

Using the transformations listed in equation A.2, equations A.4 and A.5 become,

$$\Delta s = \Delta\sigma_r = -\frac{\Delta y}{y + \Delta y}\sigma_r, \qquad \Delta t = \Delta\sigma_t = \mu\Delta s \tag{A.6}$$

It is important to note that the section of the disk containing the dovetail slots cannot support tangential stresses. The analysis assumes that the outer edge of the disk is located at the interface of the dovetail slots (effective edge shown in Figure A.2). However, the material between the dovetail slots does contribute to the radial stress. The radial stress at the effective outer edge is calculated from the centrifugal force of the material between the effective edge and the actual outer edge.

To begin the analysis, it is necessary to assume a non-zero value for the tangential stress at the effective edge of the disk. A value of σ_t was chosen to make s and t equal,

$$\sigma_{t1} = \sigma_{r1} + \beta 1\omega^2 r^2 - \beta\omega^2 r^2.$$

Next, the values of s_1, t_1, s_2, t_2, σ_{r2}, and σ_{t2} were calculated using equations A.3. Then, the values of Δs_2 and Δt_2 were calculated using equation A.6. These values were used to reindex the values of s_2 and t_2 and the procedure was repeated for the entire disk.

Since the value for σ_{t1} was arbitrarily assigned, the boundary condition ($\sigma_r = 0$) at the inner edge of the disk will not be met. To meet this condition, the entire calculation is repeated with the disk stationary ($\omega = 0$, $\sigma_{r1} = 0$). The actual solution to the approximation is obtained by superposing the stresses from both iterations with the following equations:

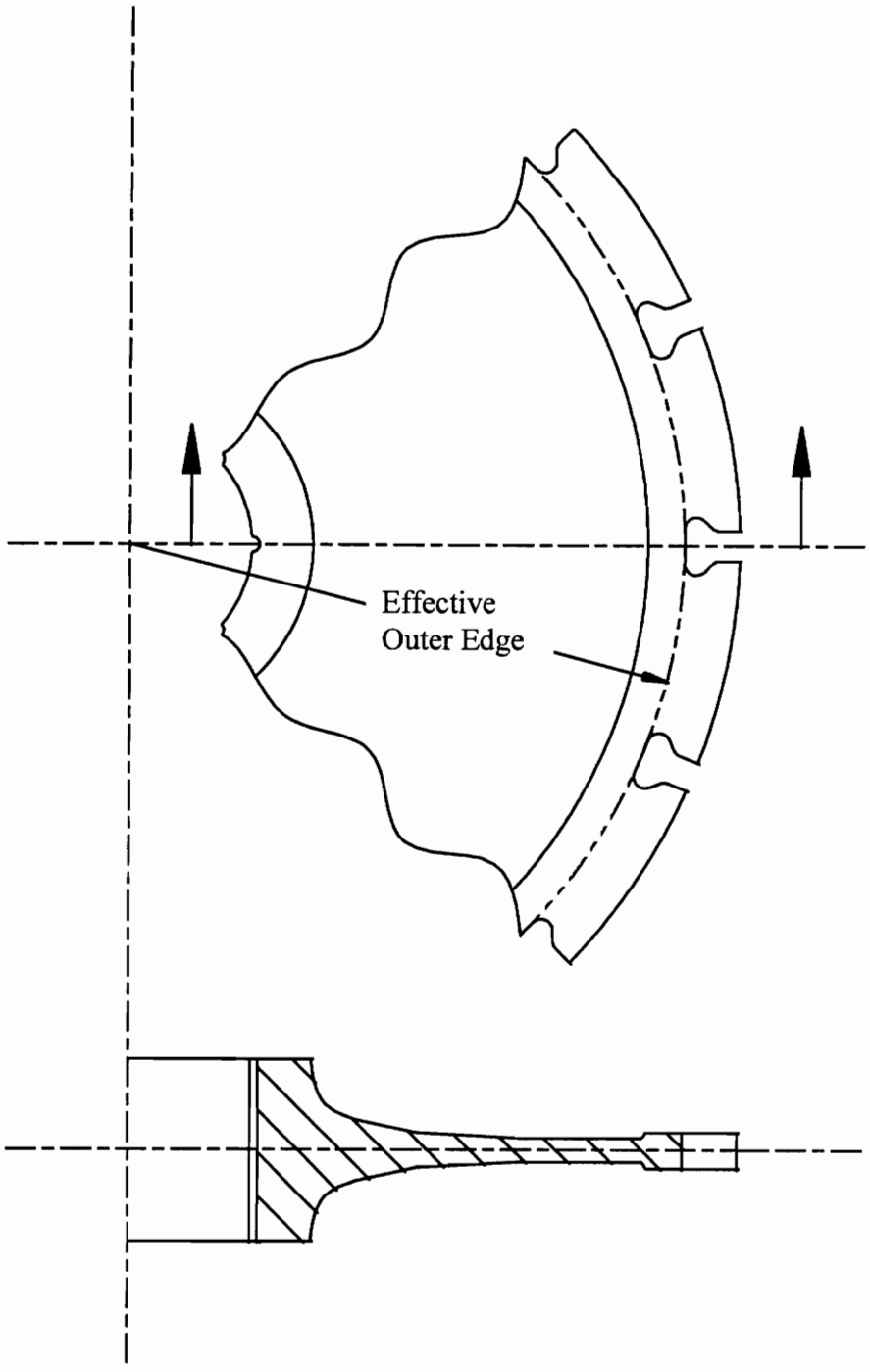

Figure A.2: Preliminary Disk Profile

$$\sigma_{r,total} = (\sigma_r + \frac{\Delta s}{2}) + n(\sigma_r' + \frac{\Delta s'}{2}),$$

$$\sigma_{t,total} = (\sigma_t + \frac{\Delta t}{2}) + n(\sigma_t' + \frac{\Delta t'}{2})$$

where,

$\sigma_{r,total}$ = actual radial stress

σ_r = radial stress from first iteration

$\sigma_{r'}$ = radial stress from second iteration

Δs = from equation A.6, first iteration

$\Delta s'$ = from equation A.6, second iteration

$\sigma_{t,total}$ = actual tangential stress

σ_t = tangential stress from first iteration

$\sigma_{t'}$ = tangential stress from second iteration

Δt = from equation A.6, first iteration

$\Delta t'$ = from equation A.6, second iteration

and,

$$n = \frac{(\sigma_{r,total})_{hub} - (\sigma_r)_{hub}}{(\sigma_r')_{hub}}$$

This method was used to analyze the tentative disk profile shown in Figure A.2. A plot of the radial and tangential stresses is included in Figure A.3. A maximum tangential stress of 23,700 psi was estimated at the disk hub. Using a stress concentration factor of 3 for the axial pin grooves in the disk hub, a maximum stress of 71,000 psi can be estimated. The stress concentration factor was estimated by assuming the disk could be

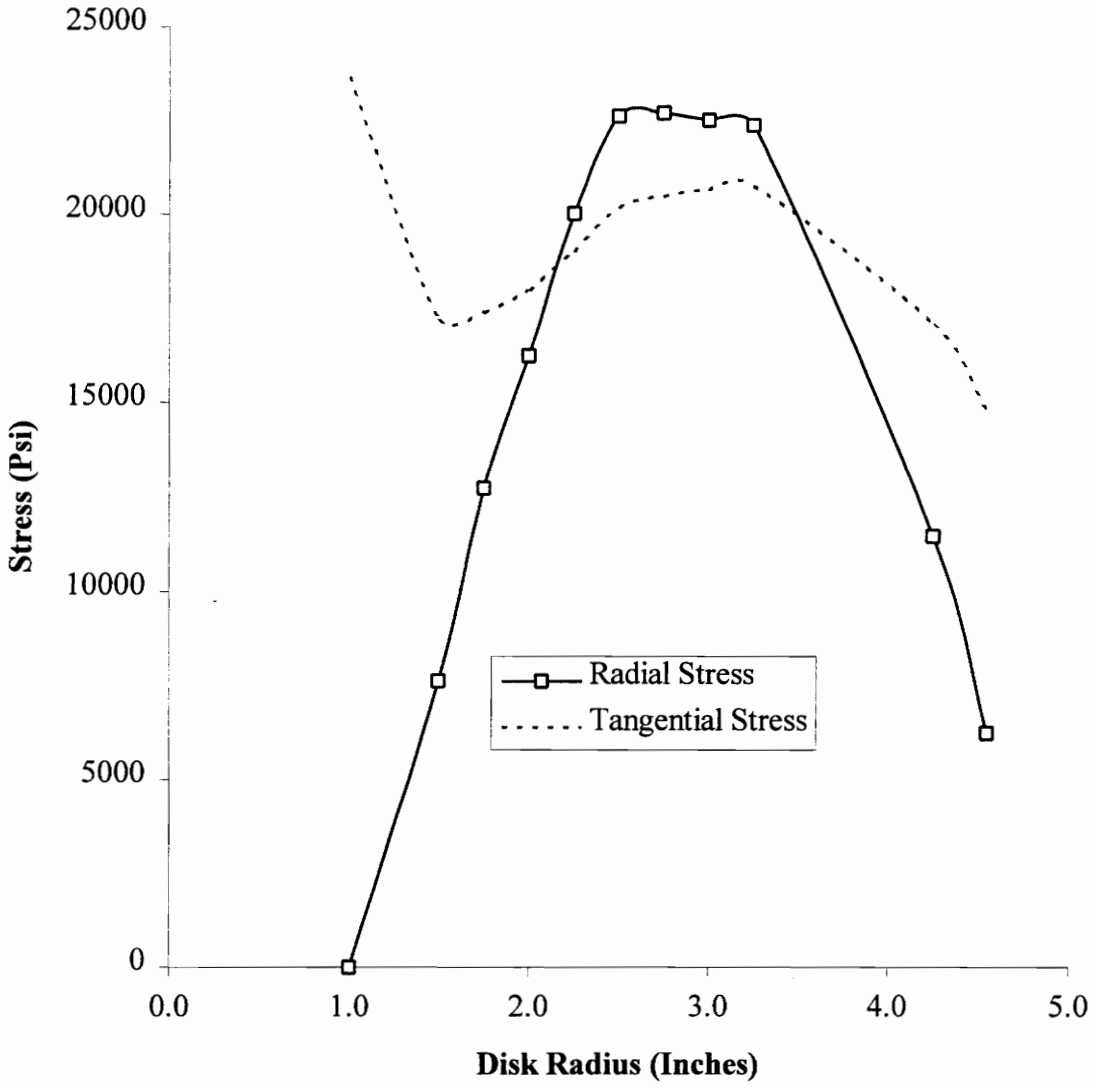

Figure A.3: Stress Plot for Preliminary Disk Profile

represented as an infinite plate with semi-circular holes (Peterson, 1971). It should be noted that the approximation method outlined in this section yields an average stress value. The actual stress profile indicates that the maximum tangential stress occurs at the center of the hub and is in excess of the average value. Therefore, the maximum safety factor (from this approximation technique) for the disk hub may be calculated as:

$$\text{Safety Factor} = \text{Yield Strength} / \sigma_{t,max} = 120{,}000 / 71{,}000 = 1.7$$

where, the yield strength of Titanium 6AL-4V = 120,000 psi.

Appendix B: Finite Element Analysis Report

The following report was prepared by Dr. Tibor Kiss, Research Associate at Virginia Tech. The report was reformatted, with the permission of Dr. Kiss, to conform with the appendices of this thesis. The reformatting involved renumbering the pages of the report and renaming the appendices of the report. The original report contained Appendices A through I. These appendix labels now contain the prefix "B-".

STRESS ANALYSIS OF A HIGH-SPEED ROTOR DISK WITH DOVETAILS AND BARS

Equipment to be used in the project

Unsteady Aerodynamic and Heat Transfer Studies in a Highly-Loaded Transonic Turbine Rotor Cascade with Simulated Shock/Wake Passing

Sponsor: AFOSR

W.F. Ng and **T.E. Diller**
Professors, Principal Investigators

Prepared by
Tibor Kiss
Research Associate

August 30, 1994
Department of Mechanical Engineering
Virginia Polytechnic Institute and State University
Blacksburg, Virginia

SUMMARY OF THE CRITICAL SAFETY FACTORS

This summary serves as a quick reference on the level of safety achieved by the design detailed in this documentation. Each critical location in the following list has a serial number,which is also shown in the accompanying figure for easy identification. For an in depth understanding and proper interpretation of the following safety factors the details of the calculations must be understood, and the accompanying discussion must be reviewed.

Safety factors for areas where yielding in material leads to failure:

1. Center of the disk hub:	3.7
2. At bottom of dovetail slot	2.4
3. Inner radius of disk rim:	5.7
4. Bottom of coupling pin-grooves:	5.5

Safety factors for areas where passing ultimate strength leads to failure:

5. Stranded cable - bar terminal interface:	2
6. Bar terminals, for shearing ball off:	10
7. Coupling pins for shear:	44
8. Bosses on inner hub, for shear:	87

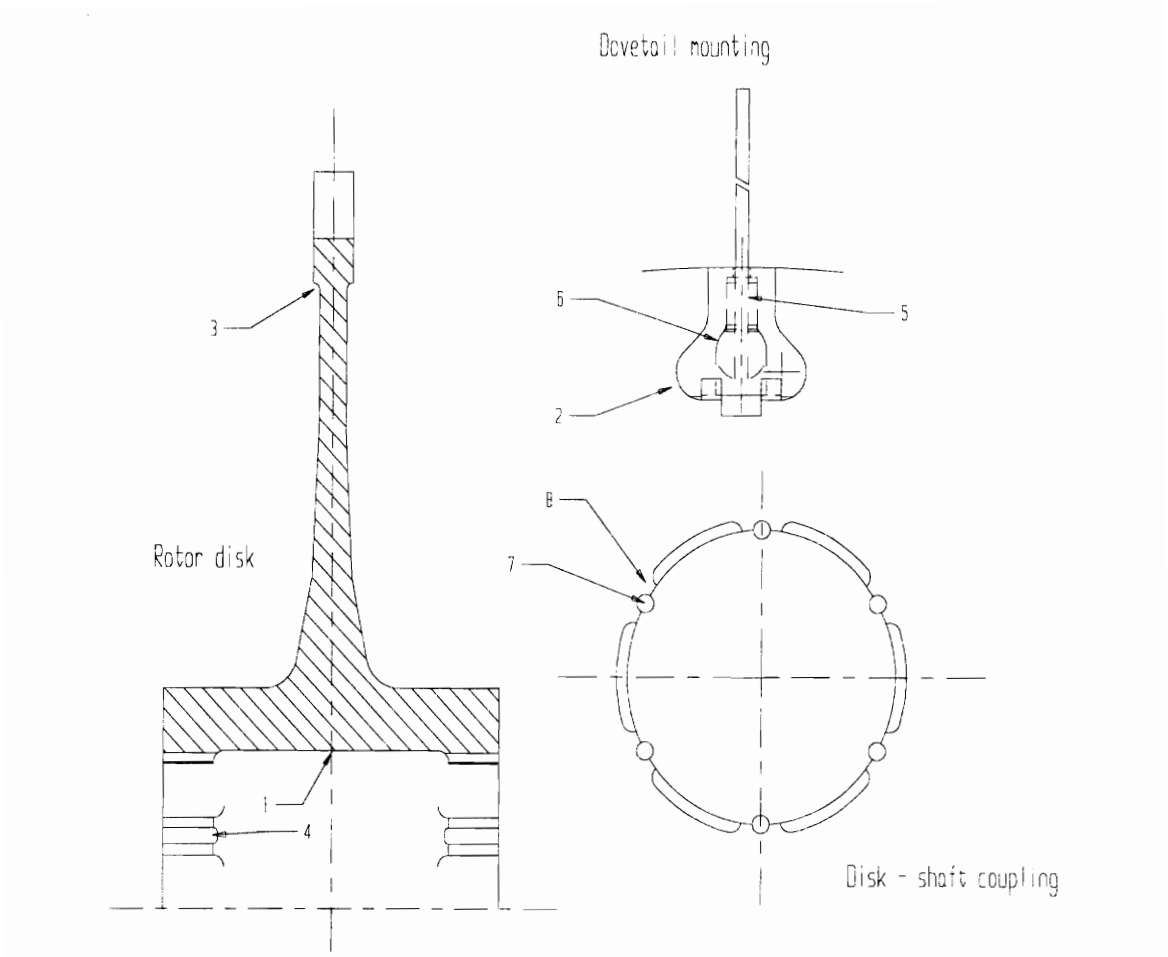

Critical locations of stress concentration

Table of Contents

Appendices

1. Introduction

This is a documentation on a rotor disk that will be used in the test section of the Cascade Tunnel of Virginia Tech. Details of the design that are given here include the exact configuration, the working conditions, the determination of the loads, the stress and deformation calculations, the interpretation of the results and conclusions about safety. Information not included here is the rotordynamics study, which will be part of a documentation on the whole rotor assembly. Fatigue issues are also not addressed, partly because of the low level of fluctuating loads and partly because of the lack of adequate methods.

The purpose of the rotor is to generate shocks/wakes upstream of a cascade of transonic turbine blades placed in the test section of the Cascade Tunnel of Virginia Tech. These shocks/wakes simulate the shocks/wakes coming from the trailing edges of nozzle guide vanes in a real transonic turbine. There are 16 bars attached to the outer edge of the disk via 16 dovetail pieces. The rotor disk is mounted on a shaft, and together they constitute the rotor. The rotor is mounted on the door of the wind tunnel and it is spinning on a plane parallel to the plane of the leading edges of the blades in the cascade. The disk itself is outside of the tunnel, but the bars enter and leave the inlet flow periodically. Unsteady heat transfer and pressure measurements will be carried out on the cascade blades, where the unsteadiness is due to the periodically passing shocks/wakes generated by the rotor. For one measurement, that is for one tunnel run, the rotor would be running for a maximum of 30 seconds. The first 2-5 seconds of this time will be used for attaining the required RPM. It is estimated that the rotor will be used for up to 1000 runs.

The strength of the generated shocks is an important factor for the measurements. The shock strength is dependent on the Mach number that the bars reach relative to the inlet flow (from now on bar relative Mach number). Two-dimensionality and periodicity considerations along with the available driving power determine the disc diameter (10 in.) and the bar length (2.5 in.). A spin rate of 21,100 RPM is required for the bar relative Mach number to reach 1.2 for this configuration. For higher shock strength higher bar relative Mach number may be desired. The upper limit of the operation is set at a bar relative Mach number of 1.3 which occurs at 23,500 RPM. The inlet flow conditions, velocity triangles and bar relative Mach number versus rotational speed are discussed in detail in Appendix B-A.

In case of overspeed, the system would be shut down by a safety instrumentation. The safety trigger would be set such that even with some time lag the rotational speed would never exceed 24,000 RPM. Therefore the system will be designed for a maximum RPM of 24,000.

The finite element calculations were carried out with CAEDS finite element modeler which is essentially the I-DEAS finite element software. The problems described here were saved on the enclosed data tape under the names PROBLEM1 through PROBLEM4. The dimension system lb-in was used for all problems. In the text the SI system was used as well.

2. Comparison with the Oxford Rotor Design

A rotor for similar purposes was built at Oxford University in the early 80's. Some of the design ideas applied at Oxford can be directly transferred to the present problem. However, the conditions for the experiments at Oxford were different, and that had to be accounted for. The main differences between the two experiments that affected the rotor design are:

1.) At Oxford, the experiments were carried out in a little building, which nobody, except the operators occupied. The operators were in an shielded bunker while the rotor was running. The safety factor (about 1.3-1.4 for yield) at Oxford was considered unacceptable for our experiments that will be carried out in a busy university building.

2.) In the short duration experiments at Oxford considerable heat transfer to the rotor could not take place. In our experiments one run may take 30 seconds, which means some heating of the edge of the rotor disk had to be taken into account.

3.) In Oxford, the rotor was speeded up in vacuum, therefore the aerodynamic drag on the rotor was not a critical issue. In our case, the rotor was going to be speeded up in ambient air, and the reduction of the drag was critical to achieve the design speed.

4.) Oxford needed a heavy rotor with a high moment of inertia, because the inertia helped maintain the rotor's rotational speed when the tunnel was running. In our case, the speed of the rotor is continuously maintained by the driving turbine, therefore there is no need for a high moment of inertia. Just the opposite, a light rotor is more advantageous, because the stored kinetic energy is lower, and a lighter outer protective shield is sufficient.

5.) Oxford did not do FEM analysis of the rotor disk. Therefore, certain geometries could not be considered because of the lack of simple stress calculation method.

3. Rotor and Shaft Material Selection

The suitable material for the rotor has to have high yield stress, low density and high toughness (large plastic deformation before breaking). The Ti-6Al-4V alloy satisfies all three criteria, and is readily available and fairly inexpensive. This material was therefore chosen for the disk. The material selected for the shaft is annealed 432 stainless steel. The relevant properties of these two materials are as follows:

	Ti-6Al-4V	A432
Modulus of Elasticity:	16,500 ksi	28,000 ksi
Poisson ratio:	0.31	0.29
Coefficient of thermal expansion:	$5.3\times10^{-6}/^{o}F$	$9.6\times10^{-6}/^{o}F$
Yield Strength:	120 ksi	95 ksi
Ultimate Strength:	130 ksi	125 ksi

4. The Selection of the Bars

Preliminary calculations showed that the centrifugal force on the bars reach very high values for the design RPM, therefore great care had to be taken in the bar selection. Also, a number of other design considerations had to be taken into account. Since it was our purpose to try bars of different thicknesses, the bars had to be exchangeable. For the same reason, configurations with threaded holes were undesirable, since stripping those threads during assembly of the rotor would destroy the whole rotor. There was a need to mount the bars such that the smoothness of the disk surface would be preserved and thereby the aerodynamic drag on the disk would be reduced. The edge thickness of the disk had to be kept as low as possible to lower the accumulated kinetic energy of the rotor, and therefore lowering the demand on the strength of the protective shielding. At the same time of course, adequate thickness for safe mounting of the bars had to be preserved.

It turned out during preliminary calculations, that the moment of the drag force on the bars at their roots is so high, that bars made of rigid material would fail. Therefore flexible aircraft stranded cable was selected for bar material. The stiffness of the stranded cable for bending is very low compared to that of a solid bar. Then, the inertia forces prevent the cable from bending enough for yielding. The strength of the bar, on the other hand, is increased when using stranded cable, because the very thin wire components are close to single crystal state and therefore extremely strong. Because the cables are loaded at about half of their breaking strength at design RPM, it was decided that their mounting to the disk would be achieved through a swaged terminal piece. The swaging is done by the supplier of the stranded cable, and the strength of the swage interface is certified. This way the most critical interface in the bar mounting is a design that has a proven good performance. The terminals are large compared to the diameter of the stranded cable and therefore the stresses on the terminal-disk interface are greatly reduced.

The strongest available cables and fittings had to be selected. A sketch and some characteristics of these pieces can be seen in Fig.B-1. For a given RPM and inlet flow

conditions the radial, tangential and axial loads on the bars can be calculated. The radial load comes from the centrifugal force and at 24,000 RPM it is 108.4 lb. The details of the calculation can be found in Appendix.B-B. The tangential and axial loads come from the aerodynamic drag. They are 10.84 lb and 1.14 lb, respectively, according to the calculation in Appendix B-C. These are maximum values, that occur when the bars are in the tunnel. The minimum axial and tangential loads are not known, since it is hard to estimate what the relative velocity of the bars to the air in the rotor housing would be. However, these fluctuating forces are neglected due to the flexibility of the bars as explained in Appendix B-D. Appendix B-D also gives some ideas about the deformation of the bars due to the periodic drag forces.

As a final result taken from Appendix B-B, a safety factor of 2.01 is achieved for the failure of the bar assembly at the swaged contact. This fairly low safety factor cannot be improved until the assembly is made of a different material, possibly some titanium alloy. Unfortunately, stranded cable and terminal made of titanium is not available off the shelf, and the cost of custom making these items was found to be extremely high.

5. Mounting the Bars on the Edge of the Disk - The dovetails

From now on, the stranded cable pieces with the swaged terminals will be simply called bars. Two factors need to be considered in the problem of mounting the bars on the rotor disk. First, the dimensions of the swaged terminal pieces are quite imprecise, tolerances are specified on the ±0.01" level. Second, the terminals are made from stainless steel as opposed to the titanium alloy that the disk is made of, which may present a problem when heating of the rotor takes place. For these two reasons rigid interference fitting of the terminals into a slot in the edge of the disk was not a feasible solution. Also, exchangeable bars with different diameters had to be allowed by the design, and that ruled out the possibility of cutting a slot for the bar terminal directly on the disk edge. Instead, titanium alloy dovetail pieces were designed that can be seen in Figs.B.2 and B.3. The dovetail pieces are exchangeable, and therefore different dovetail pieces can be manufactured for different bar terminals, if the need arises in the future. The cavity for the terminal is larger than the high limit dimensions for the terminal, therefore the terminal would sit slightly loose in the cavity. Then, different expansions of the materials due to heat causes no or low additional stresses. The bar assembly cannot fall out once the dovetail piece is slid into the dovetail slot. However, now the dovetail piece itself has to be prevented from sliding out axially from the slot. The axial force that could push a dovetail piece out from its slot is the axial component of the aerodynamic drag force on the bars. It is shown in Appendix B-C that this force in fact is very low. Also, once the rotor is spinning, there is a high pressure on the contact surface between the dovetail piece and the dovetail slot. The resulting friction force cannot be overcome by the low drag force. However, during the acceleration and deceleration periods, when a critical

rotational speed of the rotor may be passed, vibrations may occur with unpredictable effects. An interference fit between the dovetail piece and the dovetail slot without any reinforcement did not seem safe enough considering the damage that a loose dovetail piece would cause. The dovetail pieces therefore were secured in their slots by small retaining plates (See Fig.B-4). These plates are made of annealed 304 stainless steel and will be simply bent over the dovetail piece. This method of retainment is widely used, and the idea was obtained from Test Devices, Inc.

6. Selection of the Major Dimensions of the Rotor Disk

The outer diameter of the disk was determined by its function in the wind tunnel experience, and that parameter could not be varied. The thickness of the disk at the outer edge was desired to be as low as possible for reducing the mass of the disk, however, there was a limitation by the minimum thickness required for the bar mounting. Once the design of bar mounting was completed, the edge thickness of the disk was fixed at 0.3 in.

The selection of the hub diameter is the next issue. In fact, for some time we considered a disk that had no shaft but it was one solid piece attached to two flanged half shafts. The idea was very attractive from the viewpoint of reducing the stress levels to achieve an overall safety factor of about 6. However, the idea had to be dropped finally because of the anticipated problems with the alignment of the three pieces, a problem that is not present with a through shaft design. The selection of the hub diameter was determined by the minimum safe diameter of the shaft. In the shaft diameter selection, off center load considerations played an important role. It was seen earlier, that the bars will be operated with a fairly low safety factor, and the loss of a bar therefore could not be ruled out. The rest of the system had to survive the sudden off balance load that exists until the turbine shuts down and the rotor decelerates considerably. The shaft diameter was selected at 2 in., and this design parameter was considered fixed from there on.

Another major dimension is the hub length. Preliminary calculations showed that the disk's hub diameter may grow as much as 0.002 in. under the centrifugal load in case the hub is short (about 1 in.). Then press fitting of the disk on the shaft that would still hold at high RPM would require such a high prestressing, that yielding could not be safely avoided. If the interference between the disk and the shaft is not high enough, the growth of the disk hub may result in the loss of the spin balance of the rotor disk. With a long hub (2.5 in.), the outer edges of the hub would grow only 0.0001 - 0.0002 in., which is sufficient to keep the rotor in balance, as long as there was a slight interference before spinning. Another advantage of a long hub is that the axial contraction of the hub is much less than that for a short hub, again on the order of 0.0001 in. A locknut can be used then to safely secure the rotor axially. The third major advantage of the long hub is

that the coupling to the shaft can be done at the axial ends of the hub, where the stress levels from the centrifugal force load are low. The stresses due to the disk-shaft coupling are superimposed on these low stresses, making the combined stress levels still acceptable. The hub length, after thorough FEM studies with different geometries, was selected to be 2.5 inches.

7. Disk - Shaft Coupling

At normal steady operation the coupling load should not exceed the maximum torque that the turbine is capable of. In case the drag on the disk suddenly increases due to a density increase in the test section, the torque can rise higher than that. The density increase can be a result of the failure of the tunnel control, when the upstream total pressure rises. Since the safety system shuts down the tunnel at about 40 psia, the density rise is limited and the drag rise can be calculated. In Appendix B-E the calculation of the maximum coupling load is detailed, and a final result of 63.4 lb·ft is obtained.

The next issue is how to transfer this torque from the shaft onto the disk. Two coupling methods were considered, an interference and a special key coupling method. In the key coupling method six cylindrical pins were used as keys, and the method will be called from here on as pin coupling. The advantages and disadvantages of both methods were thoroughly investigated. The pin coupling would definitely prevent the rotor from rotating relative to the shaft, however it leads to high local stress concentration, that is difficult to predict. Small inaccuracies in the final manufactured pieces have a great effect on the stress concentration. Local yielding around the pin grooves and maybe in the pins is very possible. This mounting is also more complicated, more expensive to implement. The interference coupling method is simpler, less expensive, has lower stress concentrations and can be modelled axisymmetrically. However, the safety factor for local yielding is low, and when this result was obtained, the shaft - rotor interface could not be modeled with a great accuracy. The mounting and dismounting of the rotor may be troublesome. If yield occurs contrary to the calculations, the yield may affect an annulus on the circumference of the shaft or the disk hub. Also this yield may be a propagating one; yielding does not lead to loading previously unloaded regions as it would be the case with the pin coupling. After considering all circumstances, the pin coupling was chosen.

In the detailed design of the pin coupling we had to consider a number of factors. Because of the high stress levels, achieving low stress concentration factor was very important even at the cost of making the rotor more complicated and expensive. From tables, the stress concentration factor could only be estimated for the geometry with no bosses. The case that could be used for this estimation was an infinite bar with infinite number of semicircular grooves, and the bar being under axial tension. Obviously, this is

the limiting geometry when the hub's inner radius approaches infinity. Since for our case both the hub radius and the distance between the grooves are quite large compared to the groove radius, the analogy between the two cases is good. Therefore the value of 3 given for the case of infinite bar gives a good estimation. This value of the stress concentration factor was also verified as part of the present project by FEM using plane stress elements and an actual hub with rotational acceleration load. Then, an attempt was made to lower the stress concentration factor by choosing a different geometry. In the new geometry, the grooves were placed in bosses in the inner hub. One can also look at it as if some material between the grooves had been removed. The removed material is no longer pulling on the bottom of the grooves and the result is a much lower stress concentration. The situation can also be considered with the application of the stress-flow analogy. Then, the design with the pin grooves in bosses is equivalent with flow over two cavities in row, and the design with grooves only is equivalent with flow over a cylinder. Obviously, the first configuration results in more parallel streamlines, that is, it results in lower stress concentration. The concept was verified with FEM, again using plane stress elements. The details of this calculation will be discussed later. The final result for the stress concentration factor is reduced to about 1.5 when the optimum boss height and width was selected for the given groove depth. For good contact of the bosses with the shaft, six pins and bosses equally spaced around the shaft were implemented. Also, from the center of the disk hub the bosses were completely removed, so that no stress concentration at all would be present at the part of the rotor with the highest stress levels. Drawings giving the exact geometry of the rotor disk are given in Figs. B.5-B.9.

8. FEM Problem 1: Axisymmetric Analysis

The axisymmetric profile of the disk was designed with the help of axisymmetric finite element analysis. The axisymmetric model is quasi 2D and therefore it has the advantage of saving a lot of disk space and computational time as opposed to a full 3D analysis. The three dimensional details of the disk, such as the dovetails and the coupling pins, obviously could not be modelled accurately with this model. However, the 3D effects could be estimated later with applying stress concentration factors over the axisymmetric results.

The outer edge of the disk is obviously three-dimensional. For an axisymmetric analysis, the three-dimensional part had to be substituted with some axisymmetric equivalent. The solution obtained this way lacked accuracy close to where the three-dimensional region was, but with proper substitution the solution was accurate further away from that region. For a proper substitution, the material between the dovetail slots was removed, that is, the outer radius of the wheel was reduced to the bottom of the dovetail slots. The resultant of the tangential load from the removed material is zero due to the symmetry. The axial load from the drag on the bars is negligible. The radial load, which is in fact the

centrifugal force on the removed material distributed on the new edge, is substantial. This load is calculated in Appendix B-F.

The other area of three dimensionality is the hub with the pin grooves. Since the bosses on the 1.08" radius represent little masses on a small radius, the radial load from them on the rest of the disk is negligible. The net axial and tangential loads are again zero just like they were for the disk outer edge. Therefore, the axisymmetric model for the hub region is simply obtained by removing the hub bosses, that is considering the hub as circular with 1.08 in. radius.

Details of the axisymmetric study are shown in Appendix B-F. The maximum stress levels were obtained near the center of the inner hub, as was expected. Here both the tangential and axial tension is significant. In the pin coupling region, the Von Mises stress is almost the same as the tangential stress which shows that the axial and radial stresses are negligible. The small axial contraction and small radial growth of the hub assure that the rotor disk will become loose on the shaft neither axially nor radially. Summary of the quantified results are as follow:

SUMMARY OF RESULTS:

(See Fig. B-F.2. for notations)

Axial contraction at Point A:	$\Delta z = -1.55\times10^{-4}$
Radial expansion at Point B:	$\Delta x = 1.50\times10^{-4}$
Maximum Von Mises stress (Point D):	32,658 psi
Maximum tangential stress in the coupling region (Point C):	13,050 psi
Radial translation of Point E:	$\Delta x = 3.28\times10^{-3}$
Radial tensile stress at Point E:	20,820 psi

9. FEM Problem 2: Dovetail Piece and the Disk Edge

The most three-dimensional part of this region is the hole for the shank and ball of the bar terminal in the dovetail piece. However, as was pointed out before, the impreciseness of the bar terminal dimensions are really high, and the actual local stress concentrations cannot really be modelled even with a 3D analysis. Instead, the ball material would be allowed to yield somewhat, and take on a shape that greatly reduces the stress concentrations. Therefore around the bar-terminal dovetail interface only the average stresses were of interest. In Appendix B-B the average compression in the bar terminal was already calculated and here it can be claimed that the compression in the matching surface of the dovetail piece is the same. This stress is 10 times lower than the yield strength of the titanium alloy. For the rest of the edge region, a two-dimensional model was adequate to estimate the stress levels. In the 2D model, plane stress elements were used, since the axial faces were not loaded. An 11.25° section of annulus was chosen for

computational domain. This way the radial boundary planes were symmetry planes. The inner radius boundary was selected at 3.5 in. On this surface, results from the axisymmetric model could be used for boundary conditions. The applied loads were the centrifugal load, the load from the bar-terminal assembly as a single force vector, and the distributed load on the dovetail from the centrifugal force on the retaining tab. The interface between the dovetail piece and matching surfaces of the dovetail slot were modelled by using gap finite elements. These elements allow for frictionless sliding of the surfaces on each other, but do not allow for penetration of one surface into the other. The modeling is not conservative, because the friction that is present would increase the stresses. However, the model is still adequate, since the real high stresses are found at the root of the dovetail slots, and the stresses there are not affected much by the presence and magnitude of the friction forces.

Details of the calculation and contour plots of the results are shown in Appendix B-G. The relevant results are quantified in the following summary. Note, that the radial tensile stress at r=3.5 obtained from Problem 1 is recovered here, as it should be for proper modeling.

SUMMARY OF RESULTS:
(See Fig.B-G.2. for notations)

Maximum Von Mises stress at contact (Point A):	39,890 psi
Maximum Von Mises stress in the dovetail slot root (Point B):	48,990 psi
Average radial tensile stress at the inner radius (at r=3.5")	20,910 psi

10. FEM Problem 3: Hub Stress Concentration due to Centrifugal Load

A 3D model would have had to be applied on a very course grid due to the limitations of the available computer power. Therefore, it was concluded that finding a stress concentration factor with a 2D model on a refined grid, and applying it with the axisymmetric result would give better final results. Utilizing the symmetry, a 30 degree section of the hub cross section was used for the 2D computational domain for both problems. We saw earlier from the axisymmetric analysis that in the region where the bosses were going to be placed the only significant stress component was the tangential tension. Therefore, a tangential tension over the bosses had to be imposed for calculating appropriate stress concentration factors. This was achieved the easiest way by using rotational acceleration load. Note, that the magnitude of this tangential tension was insignificant. It just had to be known what it would be if no bosses were present. Therefore a reference problem with no bosses had to be solved with the same loading conditions. The details of the calculations are shown in Appendix B-H, and the relevant results are given here:

SUMMARY OF THE RESULTS:
(See Fig.B-H.2 for identifying locations)

Stress concentration factor in the bottom of the pinhole (Point A):	1.638
Stress concentration factor at Point B:	1.601
Stress concentration factor for Oxford's design:	2.850

It should be mentioned, that the stress concentration factor found for the Oxford design agrees well with stress concentration factor of 3 found in tables for the similar case of an infinite bar with semicircular groves under pure tension. In conclusion, putting the pin-grooves into bosses resulted in a great reduction of the stress concentration factor compared to the earlier Oxford's design.

11. FEM Problem 4: Hub Stress Concentration due to Torque Transfer

In this study, the rotational acceleration load was not considered, but the shaft, pins and the rotor hub as a working unit under the torque load was investigated. The goal of these calculations was to assess the stress concentrations (the average stresses were already shown in Appendix B-E to be within safe levels). The reason why this problem had to be addressed with finite element analysis was that even the most authorative stress concentrations tables do not contain data for the present case.

A major problem with the pin coupling is that the stresses in the pins and around the pin-grooves are very dependent on the inaccuracies of the geometry. Unless some unrealistic tolerance level is prescribed for the geometry, one cannot assume that more than one pin will actually take part in the torque transfer. The situation is further complicated by the fact that pulled by the centrifugal force on the disk, the hub on the z=0 symmetry plane expands radially, and therefore the inner radius of the hub is growing towards the center of the rotor. The pin has contact with the rotor disk only over a small length, that is only on a small portion of the bosses. Under these circumstances it can be expected that the stress concentrations may exceed the yield limits of the disk and shaft materials. However, it is also obvious that when this happens a very small yield will result in the loading of another pin. It can be stated, that if the accumulative inaccuracies in the pin - groove contacts are, say 0.0001 in., then local yields less then 0.0001 in. occur until the stress is everywhere reduced to about the yield strength or less.

The above discussion warns to be cautious when interpreting the results obtained with finite element method for the pin coupling. The study however, definitely gives a good idea about the extent of yielding that may take place. Just like for FEM Problem 2, node to node gap elements were used to model the interfaces. The study again was not conservative, since it did not allow for friction forces between the sliding contact

surfaces. Details of the calculation are shown in Appendix B-I, and the relevant results are summarized as follows.

SUMMARY OF RESULTS:
Max Von Mises stresses with the notation of Fig.B-I.3:

Point A:	32,320 psi
Point B:	83,770 psi
Point C:	67,650 psi
Point D:	40,000 psi
Point E:	77,040 psi
Point F:	84,310 psi
Point G:	17,920 psi

12. Conclusions

Safety factors for different types of failure can be extracted from the presented results. Some of the safety factors have to be calculated with the yield strength, and some with the ultimate strength of the material, depending on what the effect of a slight yield might be. For example, for the pin coupling region deformations on the order of 0.0001 in. completely change the load distribution, and the magnitude of the stresses. Local yielding is possible, still there is a huge safety factor for ultimate failure. It would not be wise to treat this region the same way as for example the dovetail slot, where yielding will not result in large stress reduction, and where yielding can lead quickly to ultimate failure.

Summary of the safety factors in case of maximum RPM and maximum drag load (Von Mises stresses used) is given as follows:

Summary of safety factors for areas where yield is not allowed:

Rim, at bottom of dovetail slots:	2.4
Rim, at inner radius contraction:	5.7
Hub center:	3.6
Hub, bottom of pin groove only acceleration load:	5.5
Hub, bottom of pin groove, only torque transfer	3.0

Summary of safety factors for areas where ultimate strength is the relevant limit:

The bars at their connection to the terminals:	2
Terminals, for shearing the ball off	10
Pins for shear:	44
Bosses on inner hub, for shear:	87

Summary of safety factors for local yielding on contact surfaces:

Rim and dovetail piece at contact surface:	3.01
Hub, edge of pin groove, torque transfer only:	1.43
Shaft, edge of pin groove, torque transfer only:	1.13

Care should be taken in the interpretation of these results. A full consideration of the details of the calculations is necessary to arrive at the correct conclusions concerning the safety of the operation of the rotor disk.

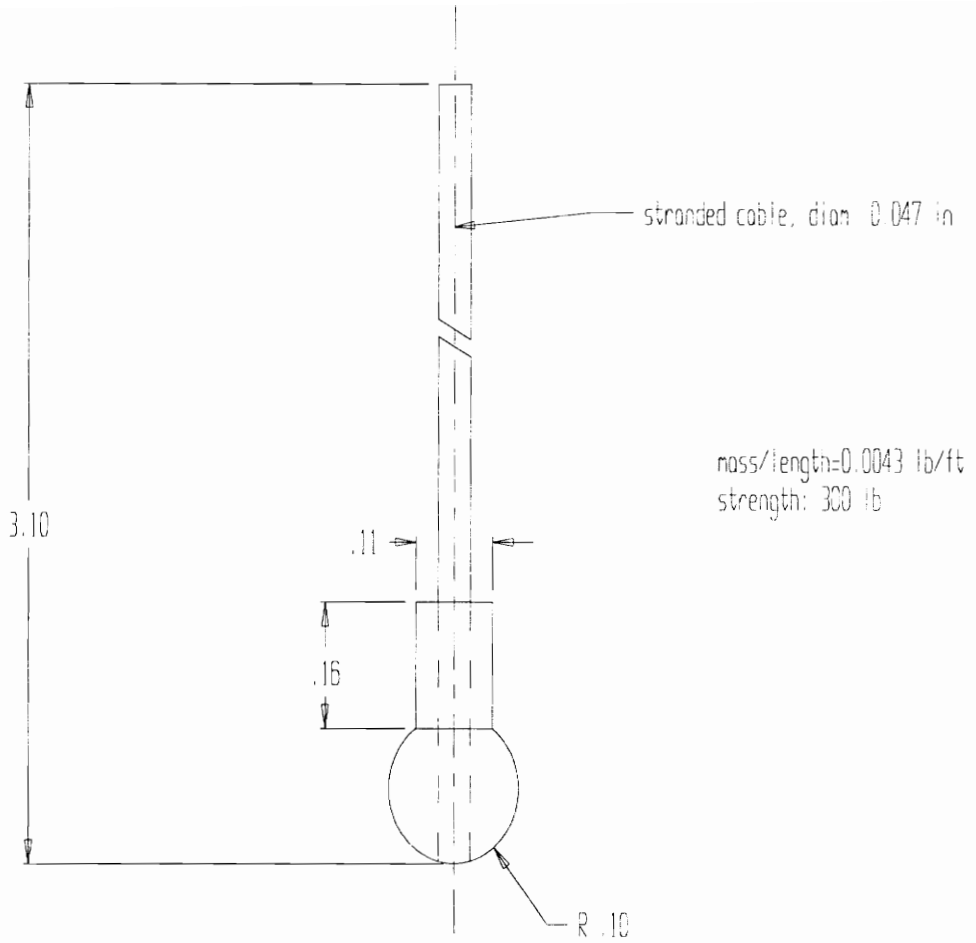

Fig.B-1. The geometry and some other characteristics of the bars

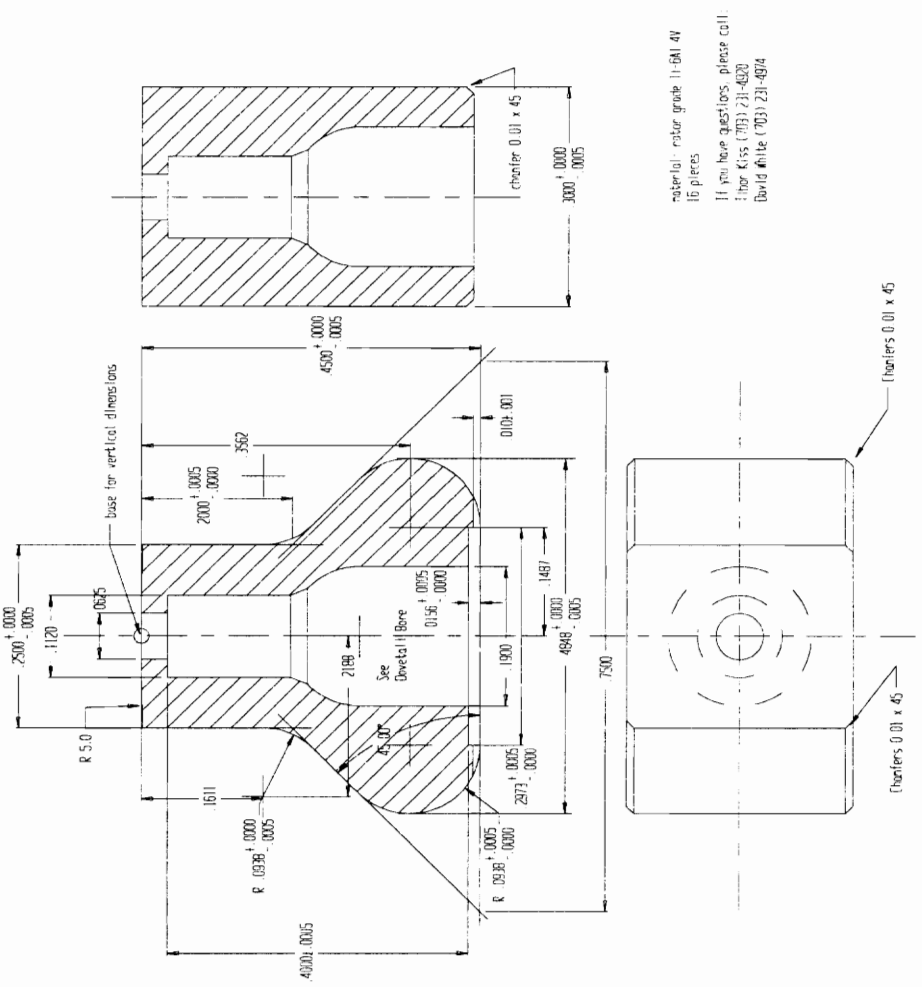

Fig.B-2. Dovetail piece

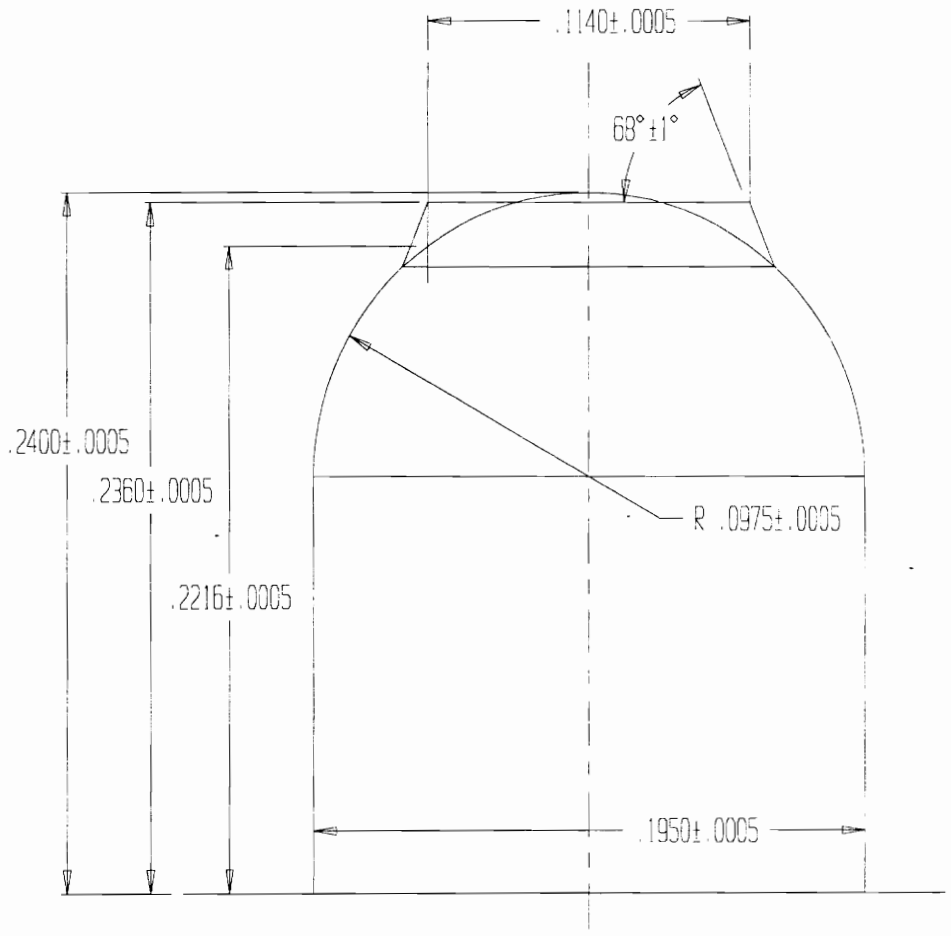

Fig.B-3. Cavity in dovetail pieces for the bar terminal

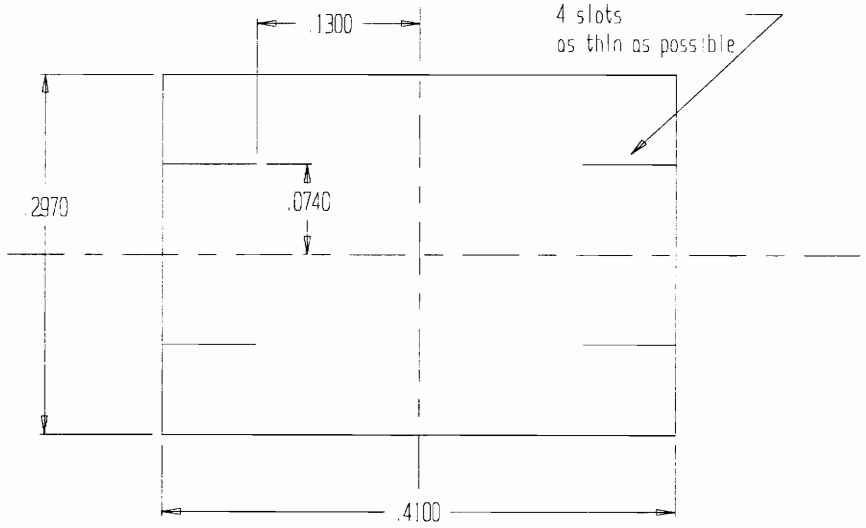

Stainless steel 304 annealed, 1/64 thick
50 pieces
tolerances: +0.0003, -0.0000

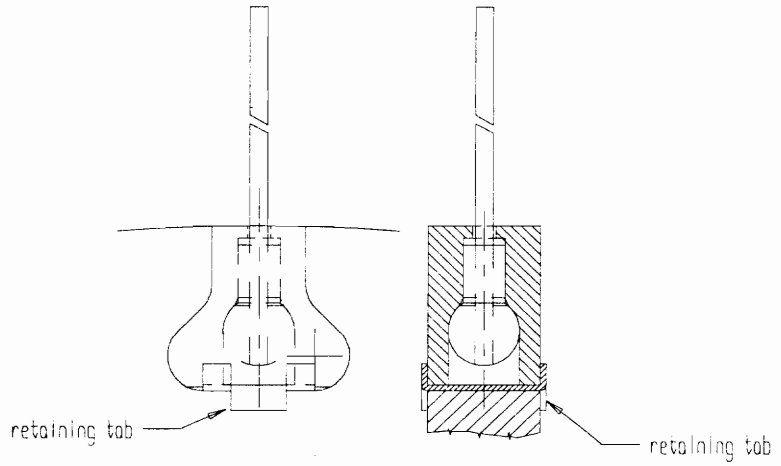

Fig.B-4. Dovetail retaining tab and its usage

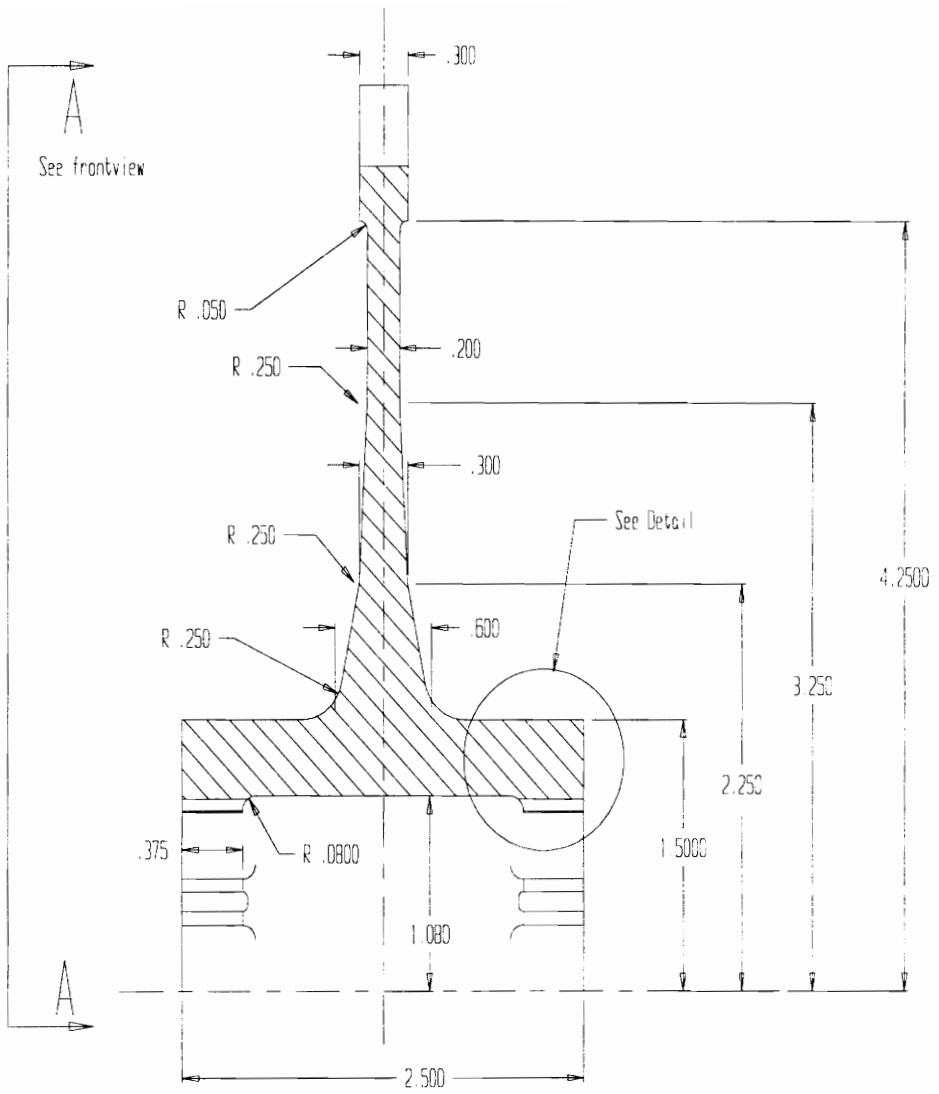

Fig.B-5. Rotor disk - side view

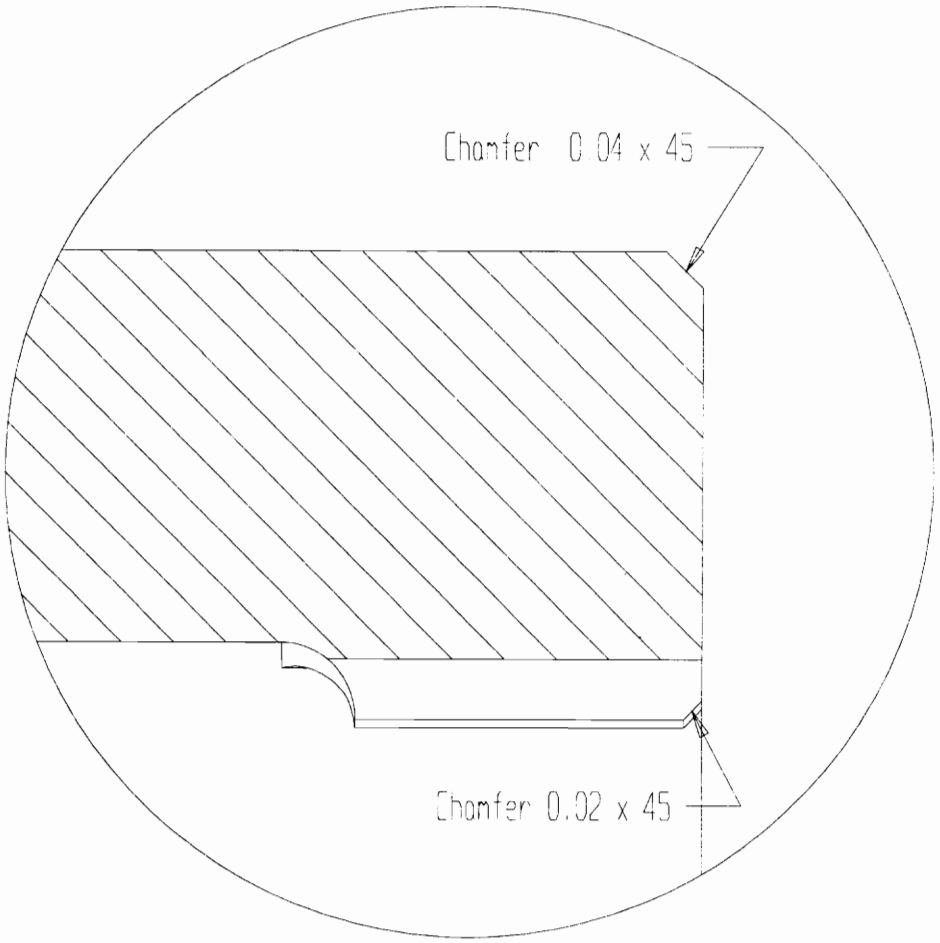

Fig.B-6. Detail in Fig.B-4.

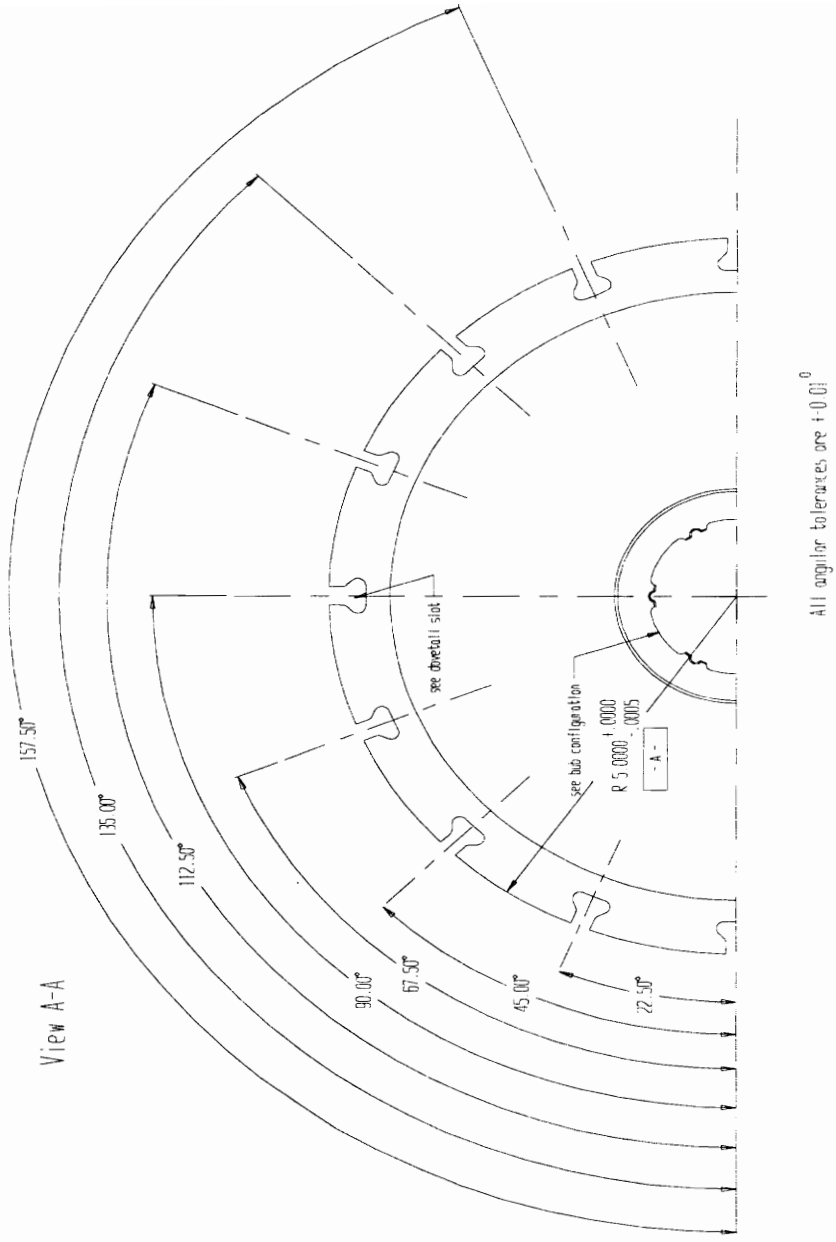

Fig.B-7. Rotor disk - front view

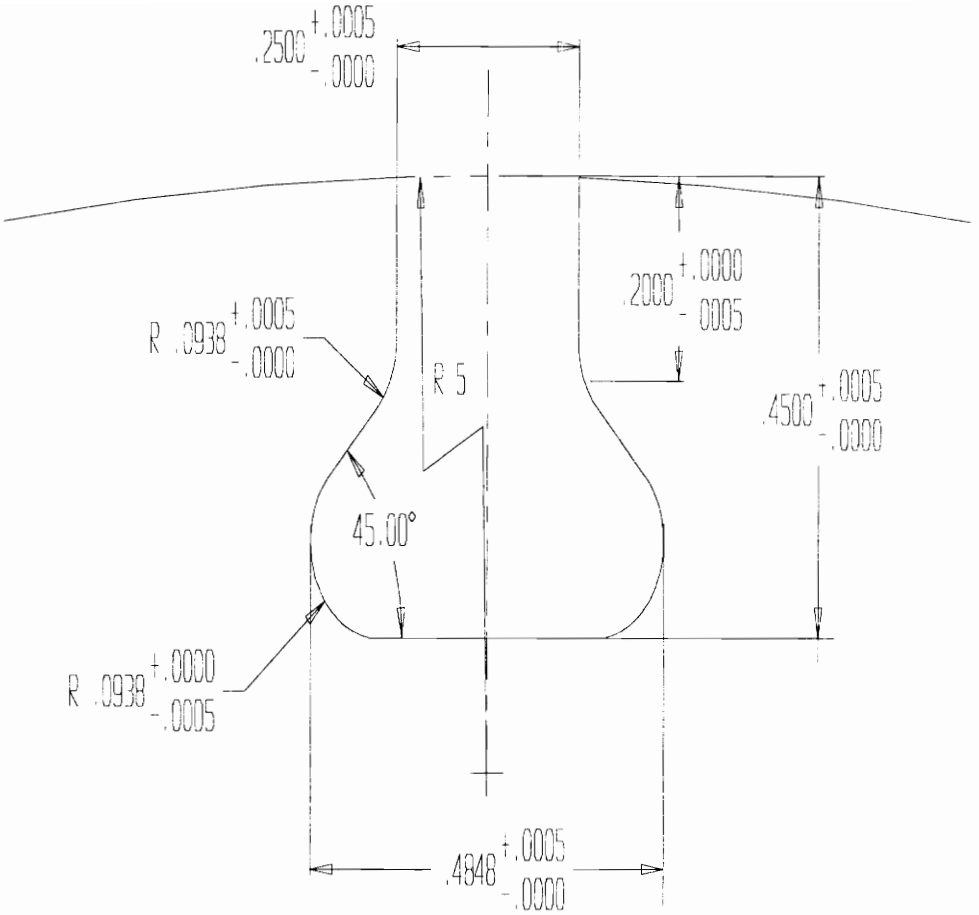

Fig.B-8. Rotor disk - details of the dovetail slots

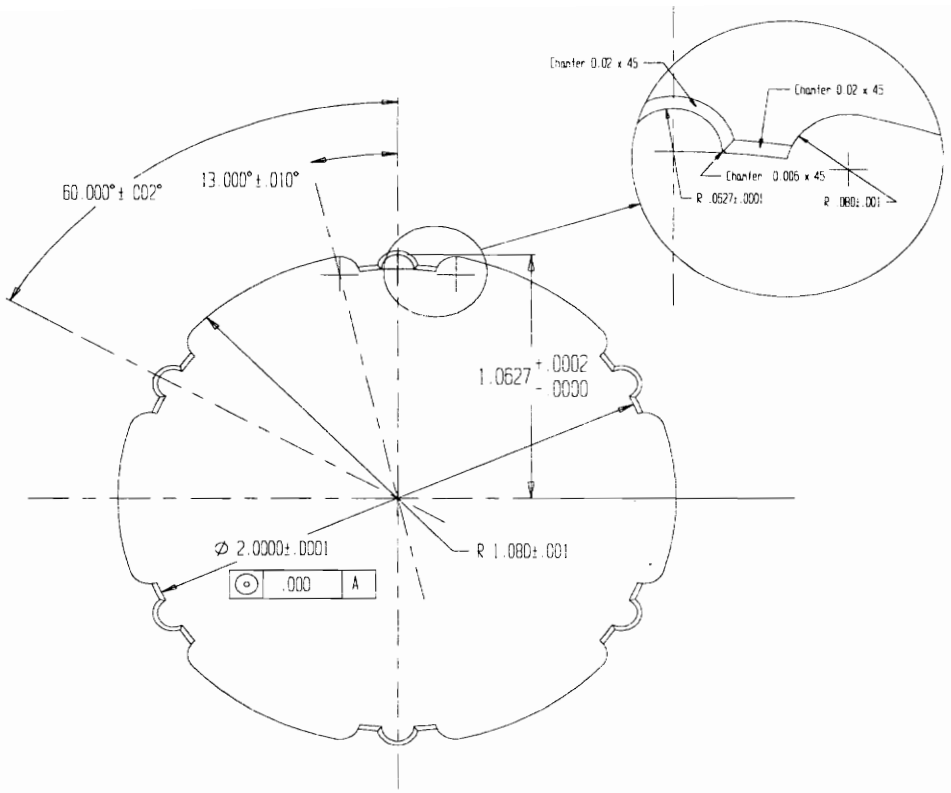

Fig.B-9. Rotor disk - hub geometry

Appendix B-A.

Inlet Flow Conditions and Bar Relative Mach Number

The inlet flow conditions and cascade geometry were obtained from GE Aircraft Engines. These parameters listed here are taken from their letter of April 22, 1993, signed by Ron Bunker etc.:

Inlet Mach number:	$M_{in} = 0.36$
Inlet flow angle:	$b_{in} = 58^{\circ}$
Exit flow angle:	$b_{exit} = 71^{\circ}$
Inlet total temperature:	$T_{0,in} = 760\ ^{\circ}\text{R} = 422.2\ ^{\circ}\text{K}$
Exit Mach number:	$M_{exit} = 1.26$

They also specified the inlet total pressure, however, in the actual tunnel environment the exit Mach number and exit static pressure determine that quantity. Therefore, from measurements

Inlet total pressure: $p_{0,in} = 33$ psia $= 2.28\times10^{5}$ Pa

With the inlet total pressure the following design inlet conditions can be calculated:

Inlet pressure:	$p_{in} = 30.2$ psia $= 2.08\times10^{5}$ Pa
Inlet temperature:	$T_{in} = 411.3\ ^{\circ}\text{K}$
Inlet density:	$r_{in} = 1.763$ kg/m^3
Inlet speed of sound:	$a_{in} = 406.5$ m/sec
Inlet velocity:	$V_{in} = 146.3$ m/sec
Inlet viscosity:	$m_{in} = 2.33\times10^{-5}$
Mass flow rate:	$m_{in} = 2.65$ kg/sec

The failure of the tunnel upstream total pressure control could result in a sudden pressure rise. This pressure rise is limited to 40 psia by the tunnel safety shut-down system. Since tunnel runs are planned also with no heating of the main flow, the temperature of the incoming air flow on a winter day may be as low as 270°K. Then, the maximum inlet density that may occur can be calculated to be

$$r_{max} = 3.56 \text{ kg/m}^3$$

The strength of the shocks generated by the rotating bars are determined by the bar relative Mach number, $M_{b,rel}$. The bar relative Mach number is the free stream Mach number observed in a coordinate system attached to and moving with a bar. The bar

relative Mach number in the test section is therefore the resultant of two components; one component is from the inlet air velocity the other is from the movement of the bars. The conditions are explained with the help of Fig. B-A.1.

At 20,700 RPM the bar relative Mach number is 1.2 according to the followings: The angular velocity is:

$$\omega = (RPM / 60) \bullet 2\pi = 2168 rad / \sec$$

The radius of the point on a bar at midspan is not less than the radius of the disc plus the cascade wall thickness plus the half of the span:

$$r_{mid} = 5in. + 0.5in. + 1in. = 6.5in.$$

The speed of the midspan point is then

$$V_b = \omega \bullet r_{mid} = 2168 \text{rad/ sec} \bullet 6.5 \text{in} \bullet 0.0254 \text{m/ in} = 357.8 \text{m/ s}$$

This and the velocity of the incoming air will determine the relative Mach number of the midspan point of the bar according to Fig.B-A.1:

$$M_{b,rel} = \sqrt{V_{in}^2 + V_b^2 - 2 \bullet V_{in} \bullet V_b \bullet \cos(148^o)} / a_{in} = 1.2$$

The same way it can be shown that at 23,050 RPM the bar relative Mach number is 1.3.

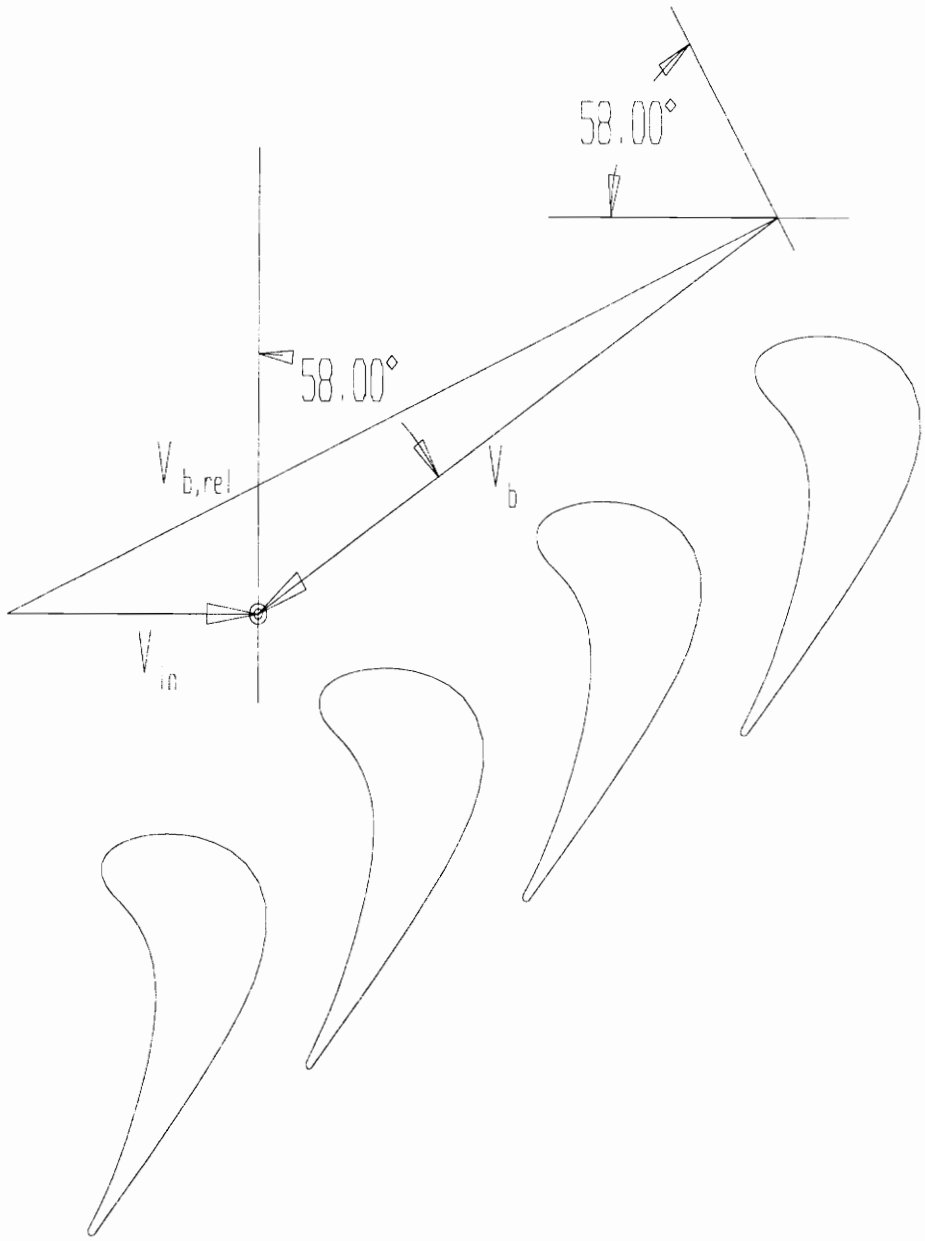

Fig.B-A.1. The bar relative velocity

Appendix B-B.

Centrifugal Load on the Bar-Terminal Assembly

The bar (stranded cable + swaged terminal) geometry was shown in Fig.B-1. Weight and strength specifications were supplied by the vendor. The force acting on a bar positioned radially, with inner end at r_0 and the outer end at r_1 , and spinning at w rad/sec is

$$F = \int_{r_0}^{r_1} r\omega^2 dm = \rho\omega^2 \int_{r_0}^{r_1} r dr$$

$$F = \frac{\rho\omega^2}{2}(r_1^2 - r_0^2)$$

$$F = m(r_1 + r_0)/2 \bullet \omega^2$$

where m is the total mass of the bar, and r the weight per length of the bar. Substituting ω_{max}=24,000/60·2·π=2513/sec, r=0.0043 lb/foot, r_0=4.6" and r_1=7.625" we obtain

$$F_{\text{cable}} = 108.4 \text{ lb}$$

With the specified braking strength of 300 lb this would mean a safety factor of 2.77. However, we had the manufacturer conduct a test on a sample of 12 bars, to verify the strength specification. This test resulted in an average breaking strength of 265 lb, with the weakest bar breaking at 218 lb. Therefore it was more appropriate to calculate the safety factor with the minimum breaking strength of 218 lb. The safety factor obtained with that is 2.01.

The maximum volume of the terminal is

$$V_{term} = 0.122^2/4 \cdot \pi \cdot 0.16 + 4 \cdot 0.1^3 \cdot \pi/3 - (3/64)^2/4 \cdot \pi \cdot 0.36 = 0.00544 \text{ [in}^3\text{]}$$

The terminal is made of stainless steel, therefore its mass is

$$m_{term} = \rho \cdot V_{term} = 0.286 \cdot 0.00544 = 0.00155 \text{ lb}$$

The maximum centrifugal force on the terminal is

$$F_{term} = m_{term} \cdot r_{max} \cdot \omega^2 = 0.00155 \cdot 5 \cdot 2513^2/386.22 = 126.4 \text{ lb}$$

The maximum combined centrifugal force on the bar is then

$$F_{bar} = F_{cable} + F_{terminal} = 108.4 \text{ lb} + 126.4 \text{ lb} = 234.8 \text{ lb}$$

To fail, the terminal has to shear at the radius of the hole provided for the shank. The average shearing stress can be calculated as

$$\tau_{ave} = F_{bar} / (d_{shank} \cdot \pi \cdot d_{ball}) = 234.8 / (0.122 \cdot \pi \cdot 0.20) = 3061 \text{ [psi]}$$

This shear stress is so low, that even with local yielding on the contact surface due to stress concentration the terminal will safely stay in the dovetail piece.

An average compressive stress can also be calculated using F_{bar} and an annular ring area

$$\sigma_{ave} = F_{comb} / ((d_{ball}^2 - d_{shank}^2) / 4 \bullet \pi)$$
$$\sigma_{ave} = 234.8 / ((0.19^2 - 0.122^2) / 4 \bullet \pi)$$
$$\sigma_{ave} = 14.1 [ksi]$$

This value is fairly low, however, due to local stress concentration, the terminal will probably yield slightly until good contact with the dovetail piece is achieved. (The terminals come with a high tolerance, therefore good matching of the contact surfaces cannot be expected)

Appendix B-C.

Periodic Drag Load on the Bar-Terminal Assembly

Periodic load will occur on the bars due to the drag rise taking place every time the bar enters the test section. The maximum drag force on one bar occurs when the tunnel is not heated (T_{in}=270°K), the pressure is at its maximum (p_{max}=40psia) and the rotor is spinning at the maximum RPM (24,000). Then, the density of the inlet air is

$$\rho_{max} = 3.56 \text{ kg/m}^3$$

and the speed of sound is

$$a = 329.31 \text{ m/sec.}$$

Then the inlet velocity is

$$V_{in} = a_{in} \cdot 0.36 = 118.6 \text{ m/sec,}$$

and the velocity of the bar at its tip is

$$V_b = \omega_{max} \cdot r_{max} = 2513 \text{ rad/sec} \cdot 7.75 \text{ in} \cdot 0.0254 \text{ m/in} = 494.7 \text{ m/sec.}$$

From the velocity triangle in Fig.B-C.1

$$V_{b,rel} = 598.6 \text{ m/sec}$$
$$M_{b,rel} = 1.82$$

The drag coefficient is 1.3 for this bar relative Mach number and the maximum drag is

$$D = C_d \frac{\rho}{2} V_{b,rel}^2 L_d$$

$$D = 1.3 \bullet \frac{3.64 \text{kg/ m}^3}{2} 494.6^2 \text{m}^2/\text{sec}^2 \bullet 2.75 \text{in} \bullet 0.0254 \text{in/ m} \bullet 1.2 \bullet 10^{-3} \text{m}$$

$$D = 48.5 \text{N} = 10.9 \text{lb}$$

The axial and radial components of the drag are

$$D_a = D \cdot \sin\gamma$$
$$D_t = D \cdot \cos\gamma$$

The angle γ can be obtained from the velocity triangle of Fig. B-C.1 as

$$\sin\gamma = V_{in}/V_{b,rel} \cdot \sin 148$$
$$\gamma = 6.027^o$$

Then

$$D_a = 1.14 \text{ lb}$$
$$D_t = 10.84 \text{ lb}$$

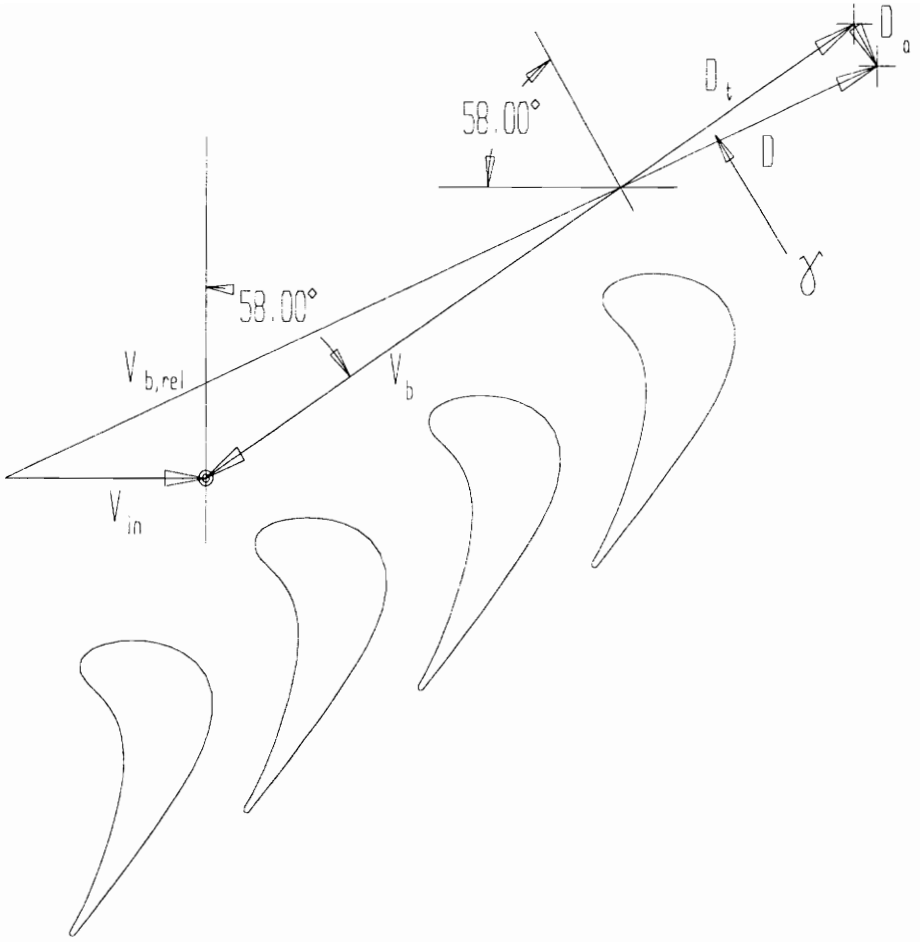

Fig.B-C.1. The drag components

Appendix B-D.

Periodic Loads on the Bar Terminals

In Appendix B-C. it was shown that there is a considerable drag load on the bars. One can take the bars as 1.2 mm diam. solid rods made of stainless steel and place the aerodynamic drag in the middle of the bar as a transverse load, and then at the terminal from just pure bending huge stresses result:

$$\sigma = \frac{M \bullet c}{I} = \frac{10.9\text{lb} \bullet 1.375\text{in} \bullet 0.0236\text{in}}{2.45 \bullet 10^{-7}\text{in}^2}$$

$$\sigma = 1445\text{Ksi}$$

This stress would obviously brake the bar. If the bar is flexible, it can bend a great deal before high stresses would arise. As an extreme, the bar can be considered to be rigid and connected to the terminal through a joint that cannot take any bending moment. A bar like that would take on a position in which the bending moment from the centrifugal force and the bending moment from the aerodynamic drag would just cancel out. With a simple calculation the angle of the bar to radial is easily obtained as 7.62°.

It is a different question, whether this large deflection can actually occur during the short time period that a bar spends in the tunnel test section under the aerodynamic drag load. The bar enters the test section from the housing where the drag is assumed to be zero, then looses speed due to the drag while in the test section. For simplicity, its motion is assumed to be on a straight line and the drag is imposed in the center of the bar. The time spent in the test section is about one third of the whole cycle time:

$$\Delta t = 1/400/3 = 8.33 \cdot 10^{-4} \text{ sec}$$

The deceleration of the bar can be obtained from the mass of the bar and the drag force:

$$a = D/m = 10.84 \text{ lb} / 3.37 \cdot 10^{-5} \text{ slug} = 321{,}740 \text{ ft/sec}^2 = 3.86 \cdot 10^{6} \text{ in/sec}^2$$

Then, the distance the center of the bar would fall back is

$$\Delta s = (a/2) \cdot (\Delta t^2) = 1.34 \text{ in}$$

which is large compared to the length of the bar, and large compared to sin $7.62^{o} \cdot 1.5" =$ 0.2" which is the lag of the bar center when the moments of the drag and the centrifugal forces balance out. The estimations were crude, but still it is clear that the inertia of the bars cannot prevent full deformation of the bars to reach the equilibrium of moments before leaving the test section.

Appendix B-E.

Disk-Rotor Coupling Forces

In Appendix B-C the maximum drag on one bar was calculated. As a very conservative estimate, the total moment of the drag forces is simply the tangential component of the drag multiplied by the number of bars and the tip radius:

$$M_d = 10.9 \text{ lb} \cdot 16 \cdot 0.646 \text{ ft} = 112.6 \text{ lb}$$

The maximum torque that the turbine is capable of in the 0-24,000 RPM range is

$$M_t = 41 \text{ lb} \cdot \text{ft}$$

The following equations can be written for the angular acceleration of the driving turbine - shaft assembly and for the angular acceleration of the disc:

$$M_c - M_d = \beta \cdot \Theta_d$$
$$M_t - M_c = \beta \cdot \Theta_t$$

where b is the angular acceleration (same for turbine+shaft and disc), Q_d and Q_t are the moment of inertia for the disk and for the turbine-shaft assembly, respectively, and M_c is the torque of the coupling forces. M_c can be expressed from these two equations as

$$M_c = (1 - \Theta_d/(\Theta_d + \Theta_t)) \cdot M_d + M_t$$

It can be shown from the geometry that $Q_d > 4 \times Q_t$,therefore the maximum coupling moment is

$$M_{c,max} = 63.4 \text{ lb} \cdot \text{ft}$$

At the radius of 1 in., where the coupling forces between the shaft and the rotor act, this torque means a maximum coupling force of

$$F_{c,max} = M_{c,max} / (1/12 \text{ ft}) = 761 \text{ lb}$$

The transmission of this force is done by 12 pieces of 1/8" diam. 3/8" long pins. First we consider the case when the load is equally distributed on all the pins. If we take the contact area for each pin as 1/4th of the pins cylindrical surface, the total contact area is

$$A_{contact} = 12 \cdot 0.375 \cdot 0.125 \cdot \pi/4 = 0.4418 \text{ [in}^2\text{]}$$

and the average compressive stress is

$$\sigma_{ave} = F_{c,max}/A_{contact} = 1.7 \text{ ksi}$$

The average shear stress can also be calculated. The area in consideration is then

$$A_{shear} = 0.375 \cdot 0.125 \cdot 12 = 0.5626 \text{ [in}^2\text{]}$$

And the resulting average shear stress is

$$\tau_{ave} = F_{c,max}/A_{shear} = 1.35 \text{ ksi}$$

However, the pin grooves cannot be manufactured precisely enough that the loads could be assumed to be evenly distributed between the pins. In fact, these average values are only good for showing that if some yielding is permitted, the coupling will still hold with a large safety factor. With low tolerances slight local yields would be enough to load enough pins to lower the stress levels well under safe limits.

As for the other extreme, we can assume that no yielding takes place and only one pin is loaded. The average compressive and shear stresses are simply 12 times the above values, that is

$$\sigma_{1,ave} = 20.4 \text{ ksi}$$
$$\tau_{1,ave} = 16.2 \text{ ksi}$$

which is far below the yield strength of the materials. Obviously, the maximum stresses will be higher than the average ones. As an attempt to quantify them, an FEM analysis had to be carried out, and will be discussed later.

Appendix B-F

Details of FEM Problem 1

The radial load on the rim:

Any mass of the rotor disk that is situated at greater radius than the bottom of the dovetail slots cannot take tangential load. Therefore the material between the slots is simply replaced with the centrifugal load acting on it. The volume of the annulus that is removed is

$$(r_2^2 - r_i^2) \bullet \pi \bullet w_e = (5^2 - 4.55^2) \bullet \pi \bullet 0.3 = 4.05\, in^3$$

Reduced with the volume of the terminals:

$$V = 4.05 - 16 \cdot 0.00544 = 3.96\ [in^3]$$

The mass is

$$m = V \cdot \rho = 3.96\ in^3 \cdot 0.1611\ lb/in^3 = 0.639\ lb$$

The total radial force is then

$$F_r = m \cdot r_{mid} \cdot \omega^2 = 0.639\ lb \cdot 4.775\ in \cdot 2513^2/sec^2 \,/\, 386.22\ in/sec^2 = 49{,}883\ lb$$

The radial forces on the bar-terminal assemblies are added to this force:

$$F = 49{,}883\ lb + 16 \cdot 234.8\ lb = 53{,}640\ lb$$

The uniformly distributed load on the disk edge for the axisymmetric model is then

$$53{,}640\ lb \,/\, (0.3\ in \cdot 2 \cdot \pi \cdot 4.55\ in) = 6254\ lb/in^2$$

and this load with a negative sign is placed as an edge pressure boundary condition on the outer edge of the model at 4.55" radius.

Computational domain:	See Fig B-F.1
Mesh elements:	Axisymmetric solid elements, parabolic quadrilateral
Mesh size:	See Fig. B-F.2
Material:	Ti-6Al-4V
Number of elements:	497
Number of nodes:	1686
Boundary conditions:	See Fig. B-F.2

Results from the finite element analysis are presented on Figs.B-F.3-6. The deformation is shown in Fig.B-F.3. It can be seen that the rotor disk is expanding a lot radially on the centerplane, however, near the axial end of the hub the expansion is low and so is the axial contraction of the hub.

Contour plots of the x and z tensile stresses are shown in Fig.B-F.4 and in Fig.B-F.5, respectively. The x (radial) tensile stress is nearly 0 on the inner hub, as it should be since that is a radial surface. The z (axial) tensile stress is also close to zero. Therefore, the only significant stress in the coupling region is the tangential tensile stress.

On Fig.B-F.6., the Von Mises stress contours can be seen. The maximum stress is at the inner radius of the hub on the centerplane (Point D in Fig.B-F.2). The Von Mises stress is low in the coupling area, and again, it is almost purely tangential tensile stress.

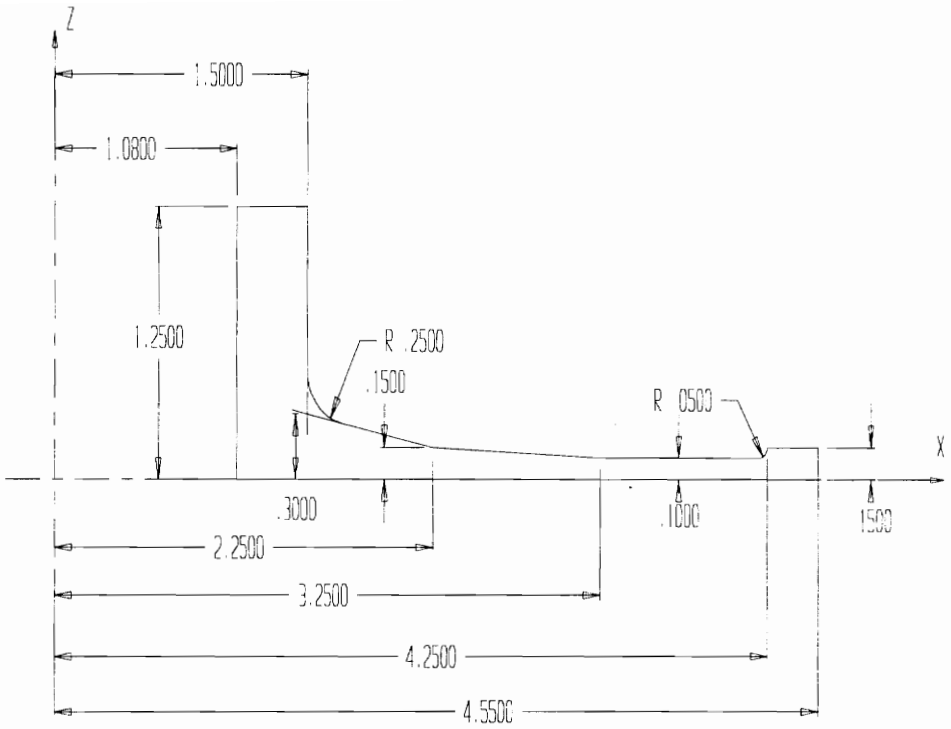

Fig.B-F.1. Computational domain for Problem 1

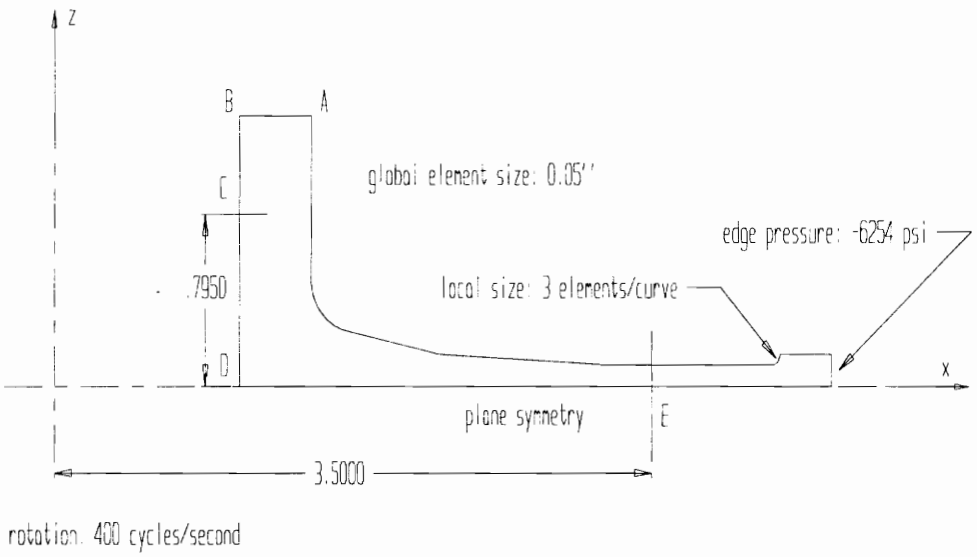

Fig.B-F.2. Mesh and boundary conditions for Problem 1

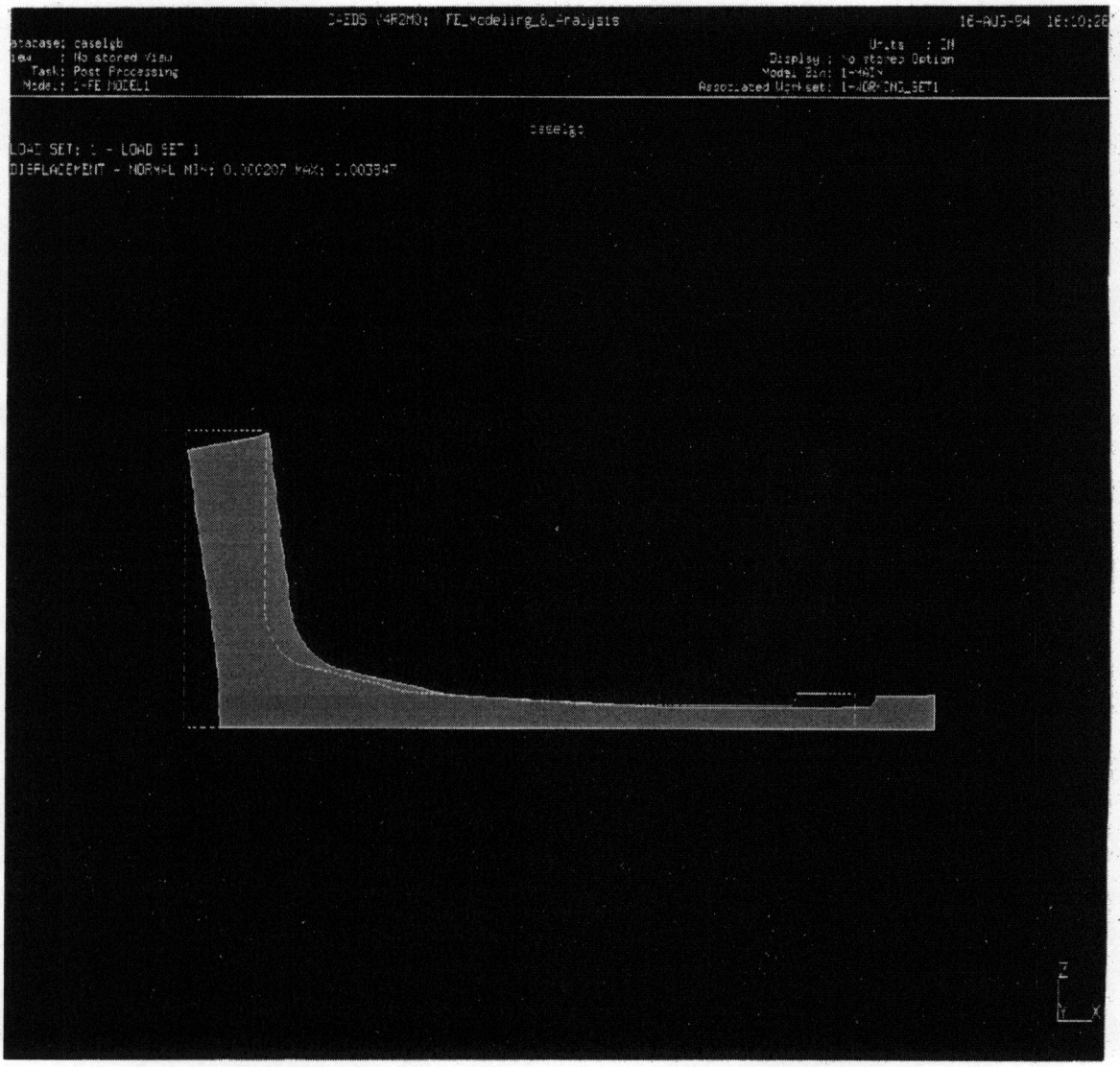

Fig.B-F.3 Deformation of mesh areas from Problem 1

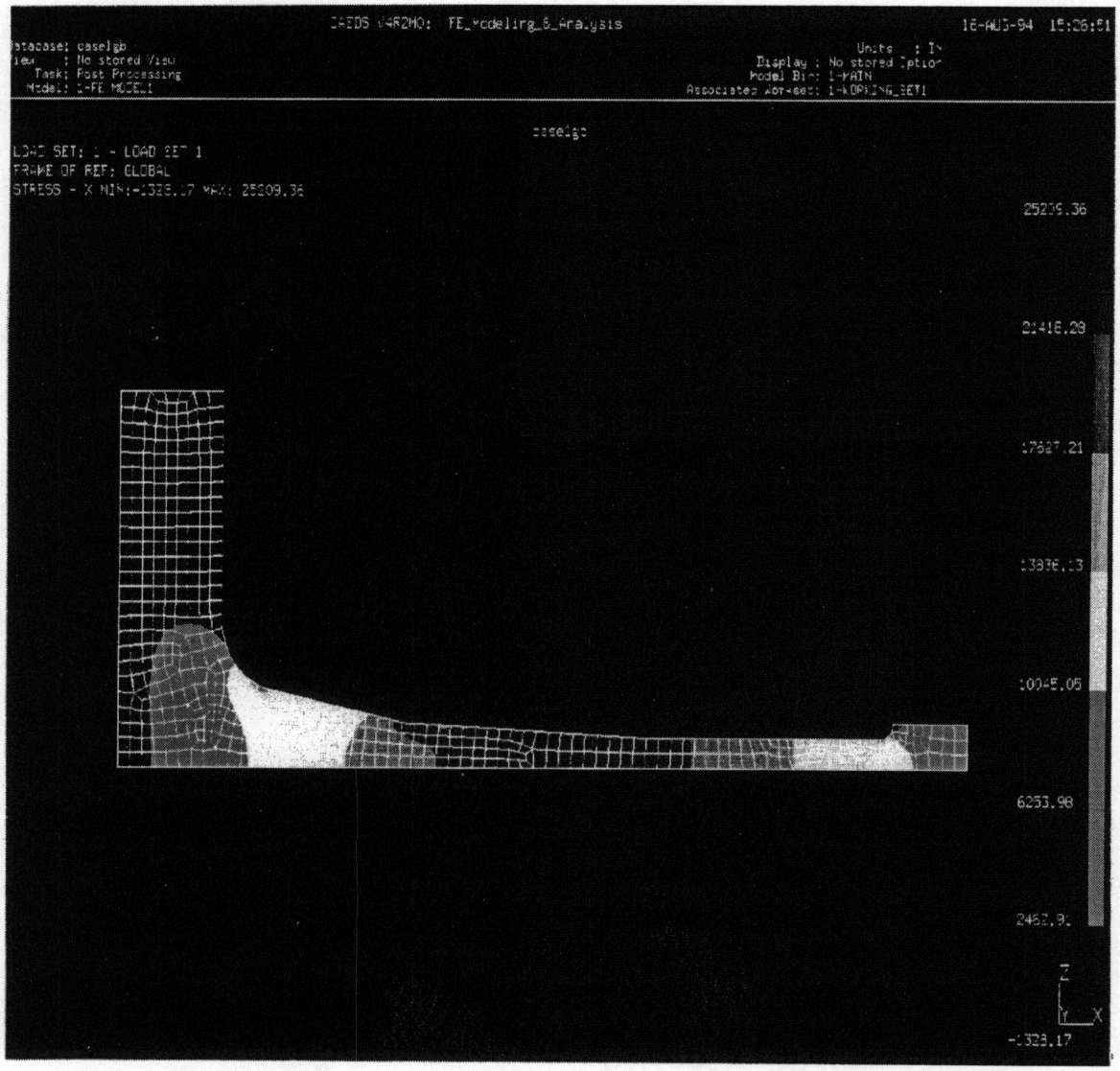

Fig.B-F.4 Contour plot of the x tensile stress for Problem 1

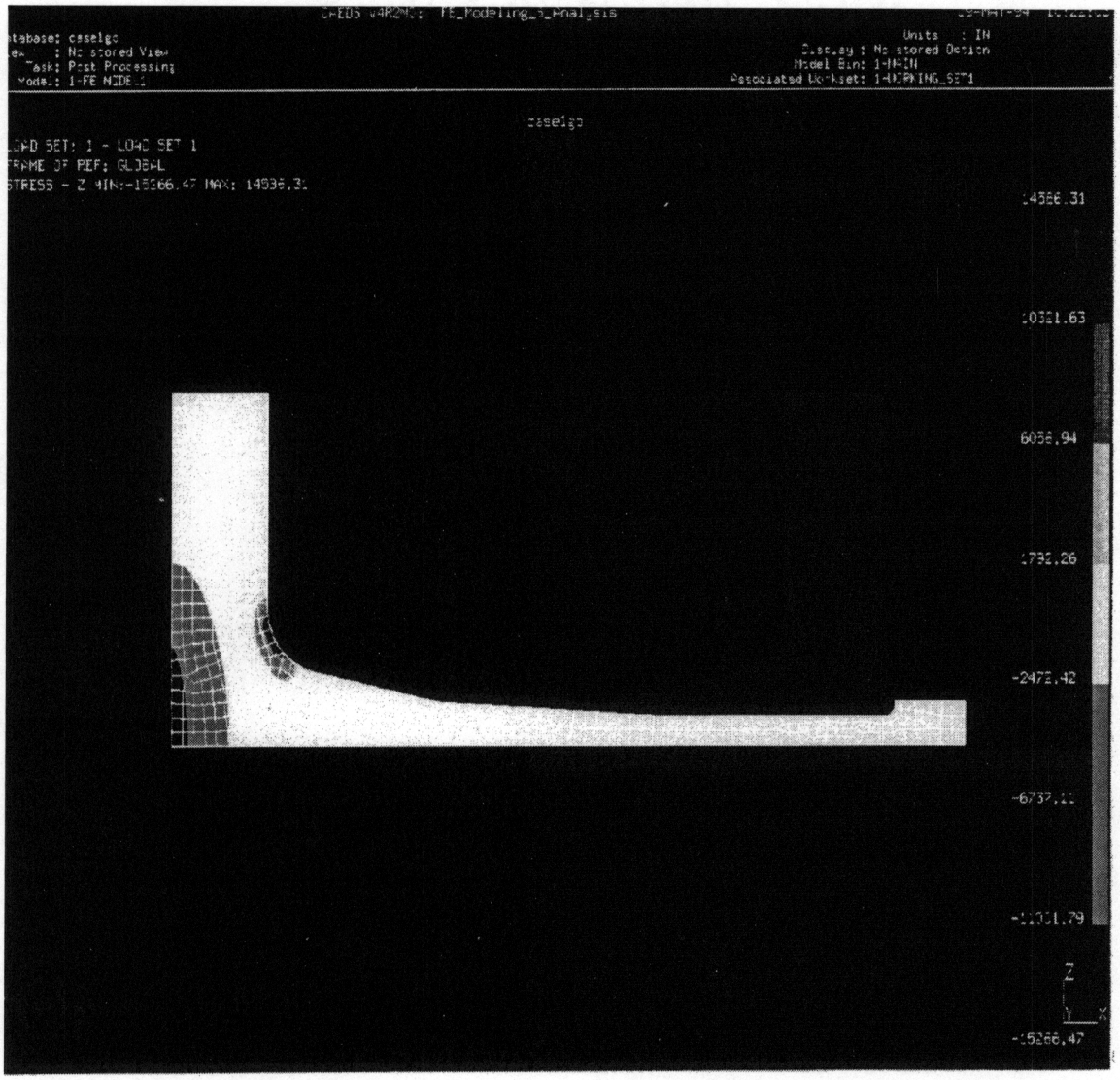

Fig.B-F.5. Contour plot of the z tensile stress for Problem 1

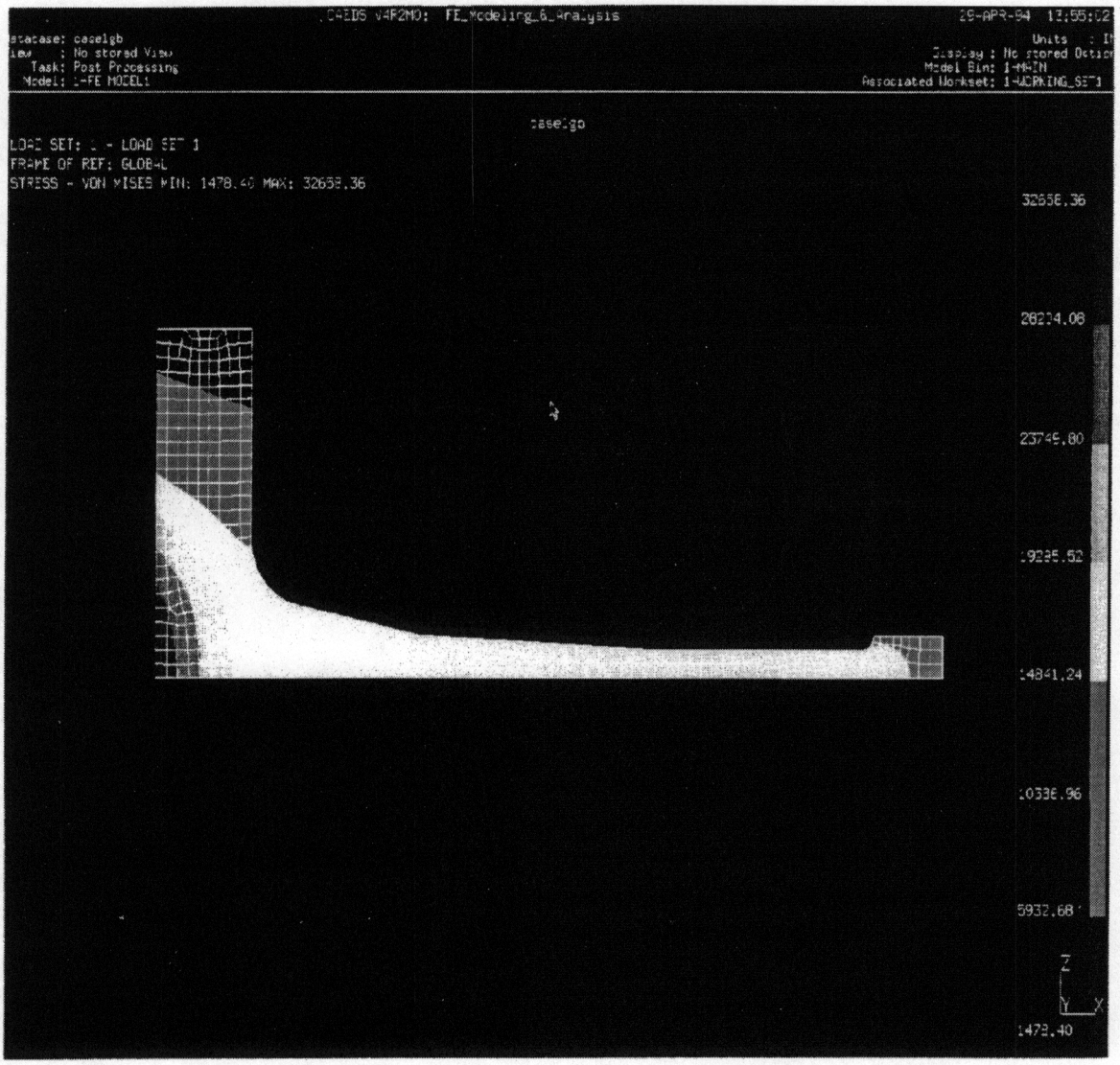

Fig.B-F.6. Contour plot of the von Mises stress for Problem 1

Appendix B-G.

Details of FEM Problem 2

Replacement of the bar and the bore for the bar terminal with a single force:
The total mass removed from the dovetail for creating the dovetail bore is 1.257×10^{-4} lb, as can be calculated from Fig.B-3. The centrifugal force is then reduced by

$$4.7"\cdot(400\cdot2\cdot\pi)^2\cdot1.257\cdot10^{-3}/386.22 = 96.8 \text{ [lb]}$$

compared to a solid dovetail.
The total centrifugal force on the bars was found earlier to be 234.8 lb. Then the net force that has to be applied on one half of the symmetric dovetail piece:

$$F = (234.8 \text{ lb} - 96.8 \text{ lb})/2 = 69 \text{ lb}$$

Replacement of the dovetail retaining tab with edge pressure:

Area of tab plates:	0.2207 in^2
Thickness:	0.0156 in
Volume:	3.443×10^{-3} in^3
Mass:	9.85×10^{-4} lb
Centrifugal force:	72.78 lb
Length of edge:	0.2973 in
Edge pressure:	244.8 lb/in

In FEM problem 2 the actual edge pressure was 312.3 lb/in, since the calculation was done before the tab geometry was finalized. Using that figure is, however, conservative.

Computational domain:	See Fig B-G.1
Mesh elements:	Plane stress, linear quadrilateral
	Thickness: 0.3 in. for Mesh Area 1 and Mesh Area 2
	0.2 in. for Mesh Area 3
	(See Fig. B-G.2)
	Node to node gap elements on indicated edges in Fig.B-G.2
Mesh size:	See Fig. B-G.2
Material:	Ti-6Al-4V for all three mesh areas
Number of elements:	258 on Mesh Area 1
	847 on Mesh Area 2
	346 on Mesh Area 3
Number of nodes:	290 on Mesh Area 1
	904 on Mesh Area 2
	383 on Mesh Area 3
Boundary conditions:	See Fig. B-G.2

Figure B-G.2. shows a restraint of Dy = 0.00545" at the bottom of the dovetail. This restraint is not necessary to make the problem statically determinate from the physical point of view. However, the solver of the equations cannot use the Node to Node Gap Elements to make the problem statically determinate. The above mentioned restraint is sufficient to make the dovetail piece statically determinate regardless of the presence of the Node to Node Elements. If this restraint is specified such that the resulting reaction forces are zero, then there is no real physical effect of this restraint, and it just serves to get around a technical problem with the coding of the solver. To find the correct values for this restriction involves an iteration process in which the restraint is changed until the reaction forces come to zero.

On Fig.B-G.3 the deformation can be seen. It is clear, that we cannot expect a large area of surface contact between the dovetail piece and the rim of the disk. In Fig.B-G.4. the Von Mises stress contours are shown for the whole computational domain. From this figure, the only interesting area is the vicinity of the dovetail. Therefore in Fig.B-G.5. the Von Mises stress contours are shown focusing on and around dovetail.

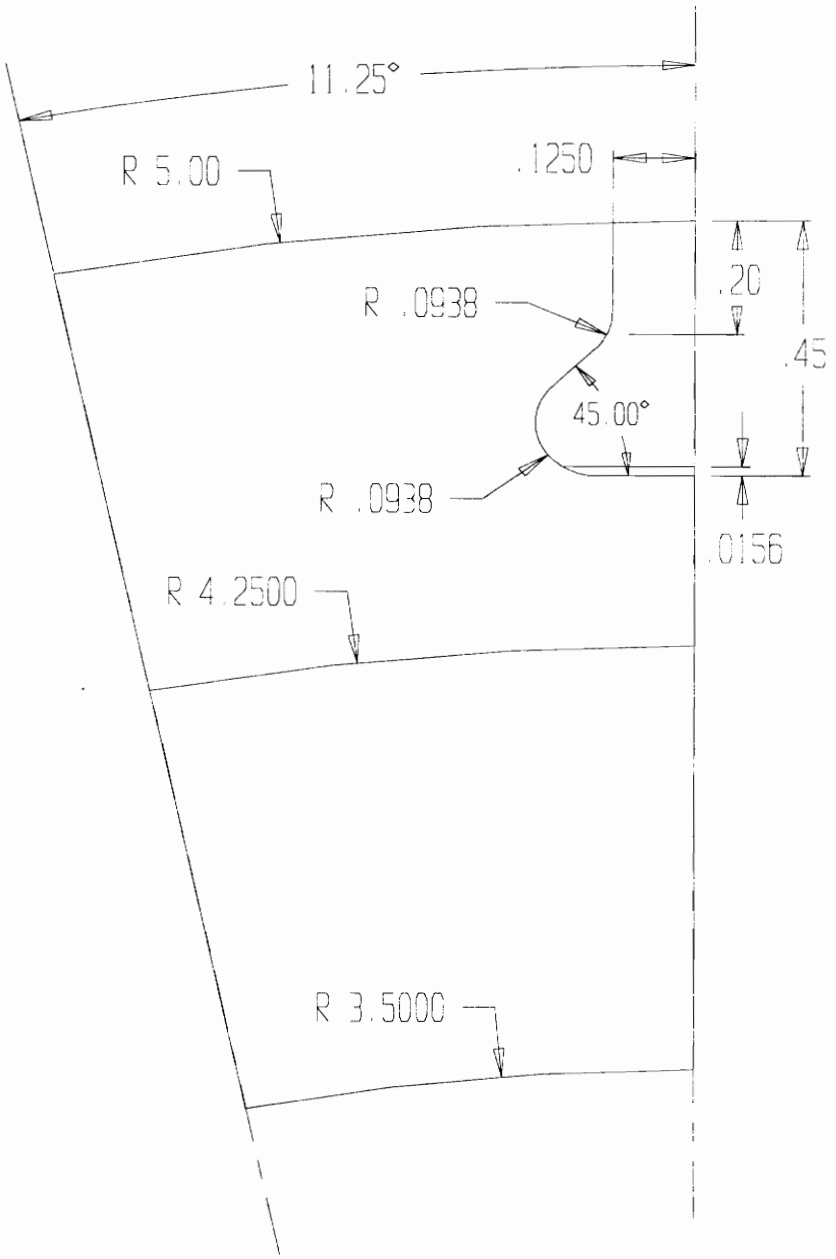

Fig.B-G.1. Conceptual domain for Problem 2

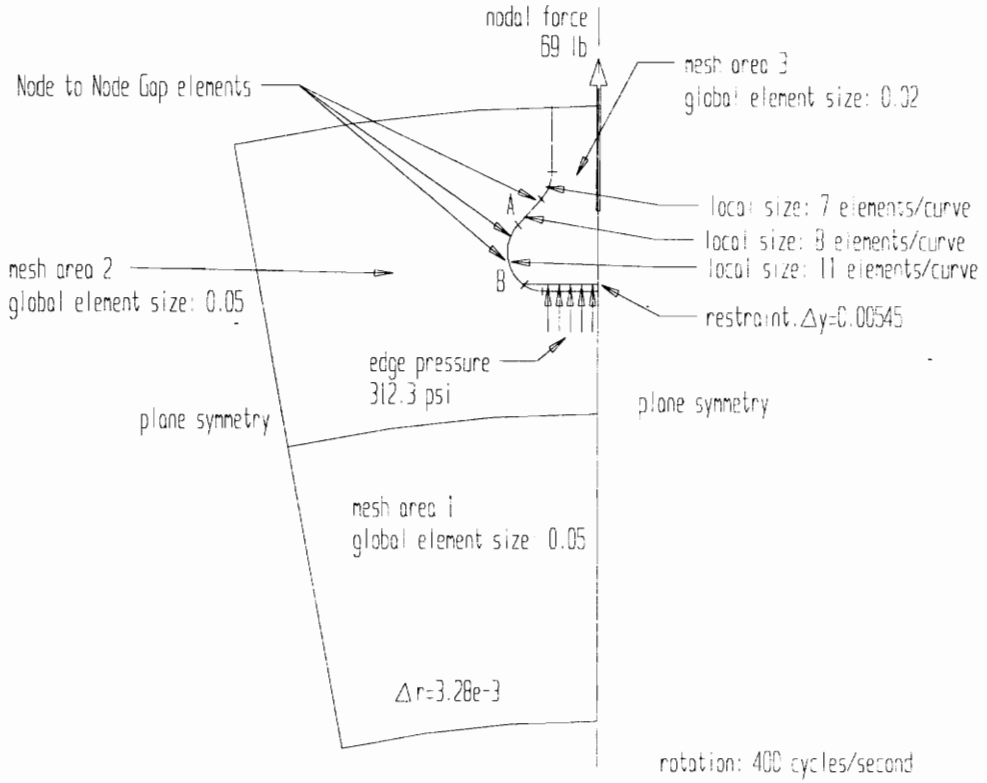

Fig.B-G.2. Mesh and boundary conditions for Problem 2

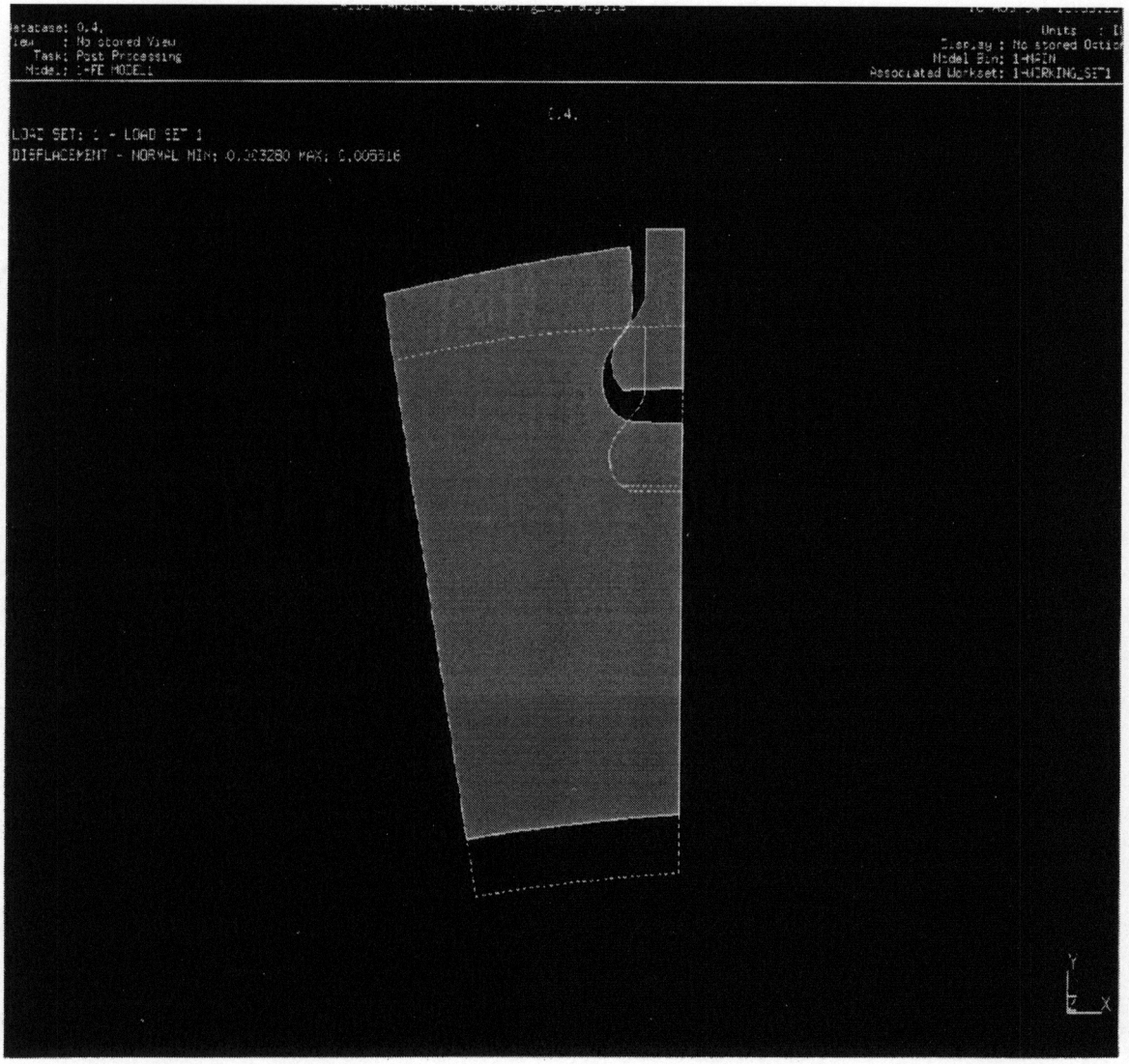

Fig.B-G.3. Deformation of mesh areas for Problem 2

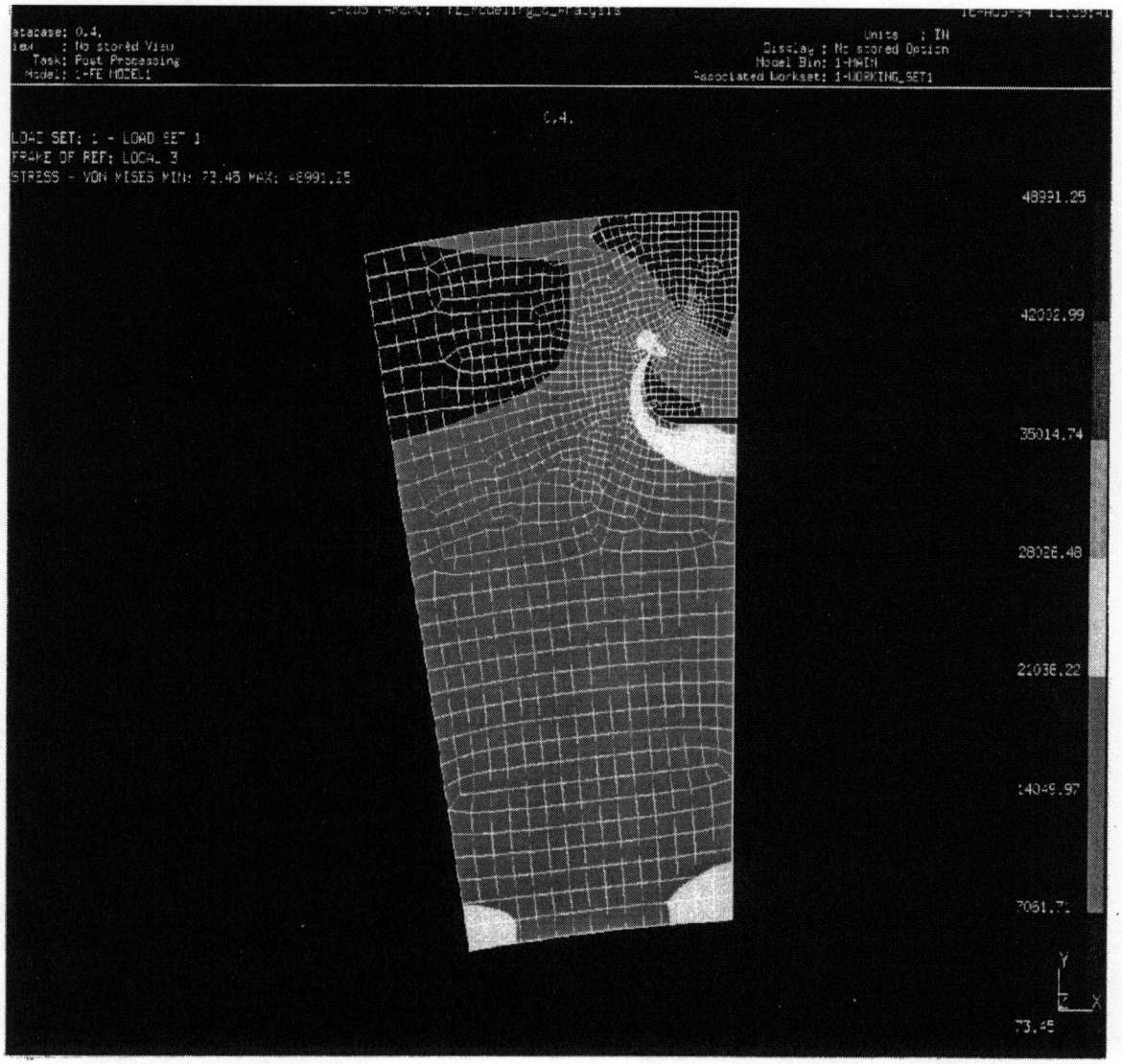

Fig.B-G.4. von Mises stress contours for Problem 2. Full view

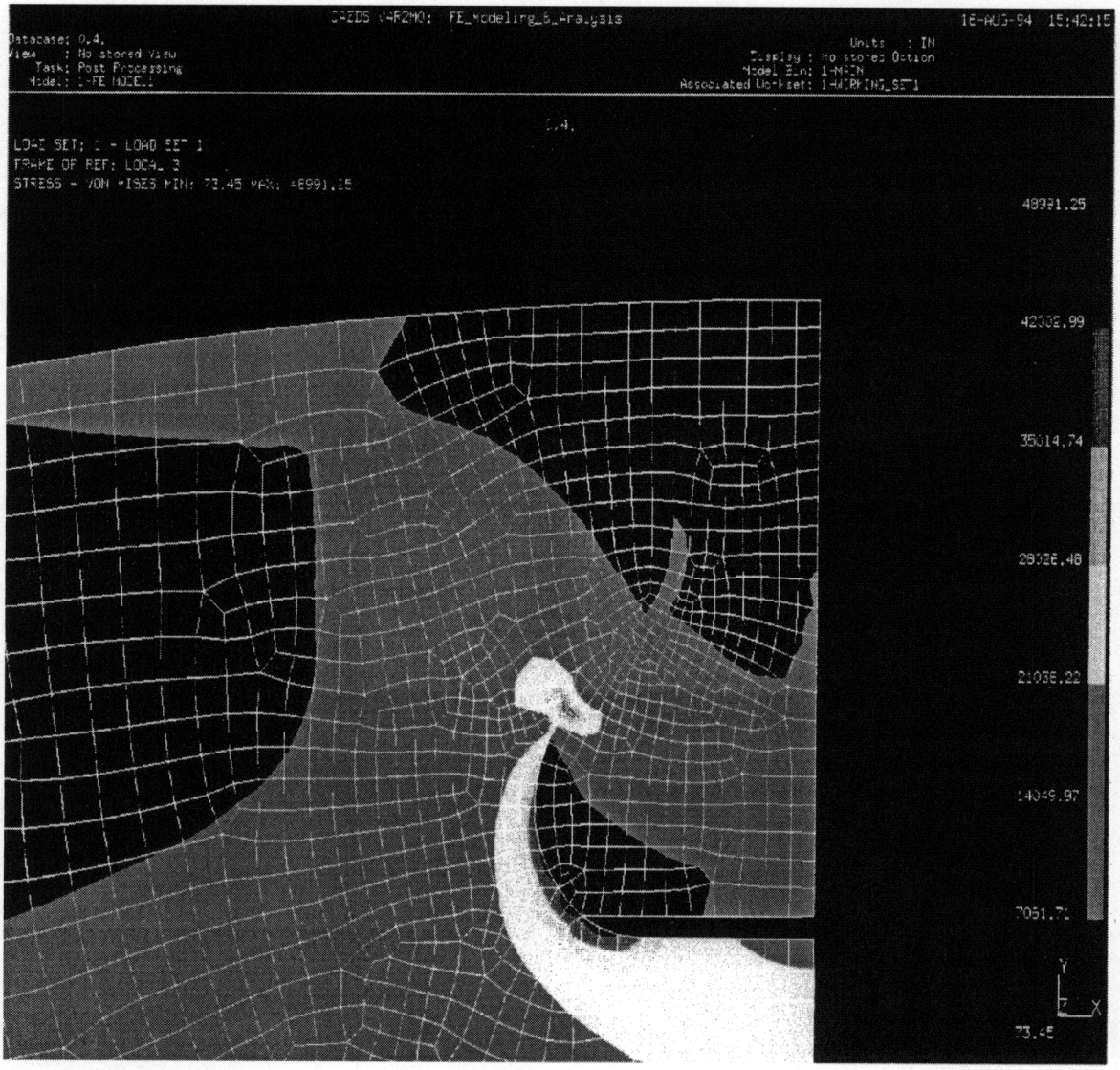

Fig.B-G.5. von Mises stress contours for Problem 2. The dovetail area

Appendix B-H.

Details of FEM Problem 3

Computational domain:	See Fig. B-H.1
Mesh elements:	Plane Stress, parabolic quadrilateral Thickness: 0.375"
Mesh size:	See Fig.B-H.2
Material:	Ti-6Al-4V
Number of elements:	1125
Number of nodes:	3502
Boundary conditions:	See Fig. B-H.2

The stress contours for the reference problem are not shown since the solution is trivial. The maximum Von Mises stress (which is the same as the maximum tangential stress) obviously occurred on the inner radius of 1.08" with a value of 5,411. The Von Mises stress contours for the boss - pin groove problem are shown in Fig.B-H.3. Local maximum stresses were 8,862 psi at Point A and 8,662 psi at Point B (See Fig.B-H.2). Von Mises stress contours are also shown for the problem of pin groove only (the Oxford design) in Fig.B-H.4. The maximum Von Mises stress occurred in the bottom of the pin groove as expected, the value being 15,420 psi. With these results, stress concentration factors can be calculated for both problems.

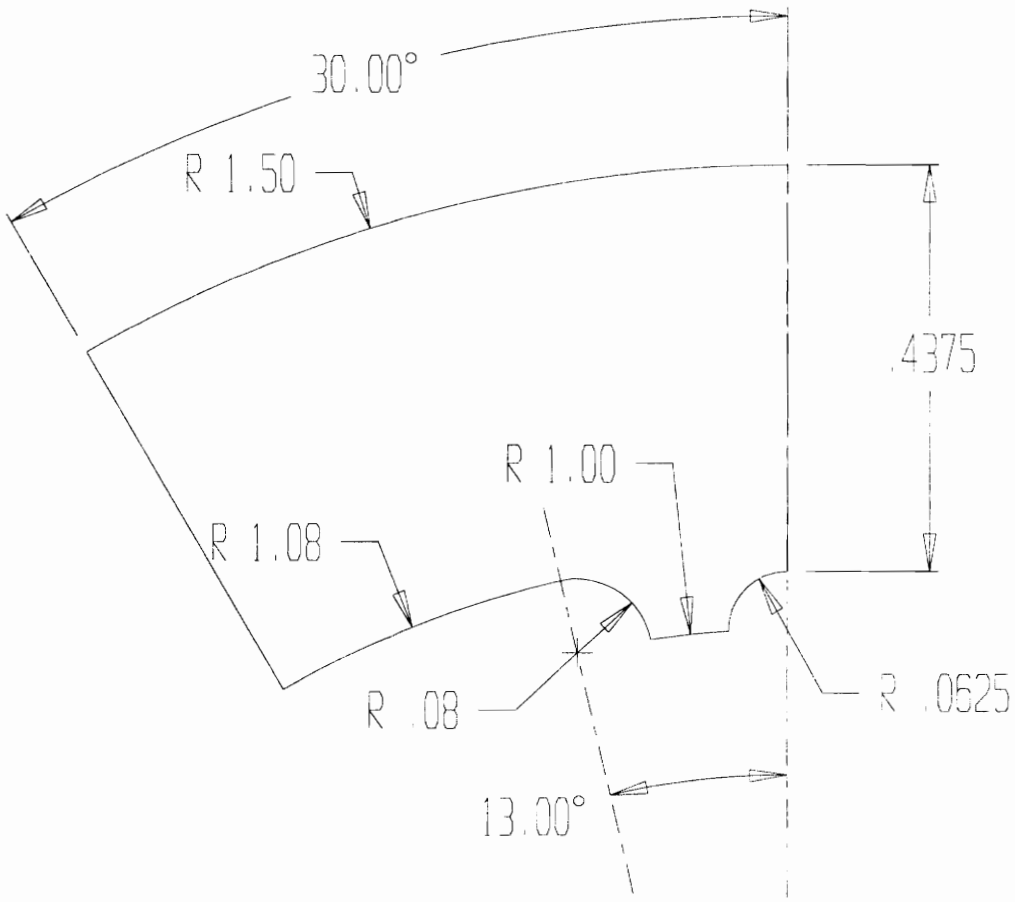

Fig.B-H.1. Computational domain for Problem 3

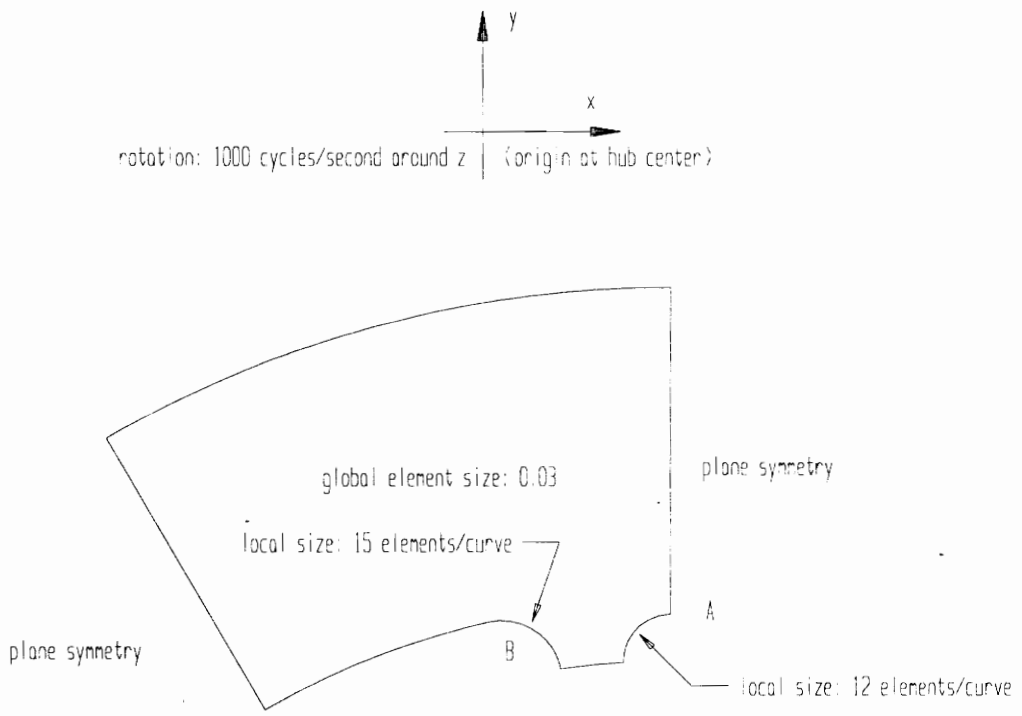

Fig.B-H.2. Mesh and boundary conditions for Problem 3

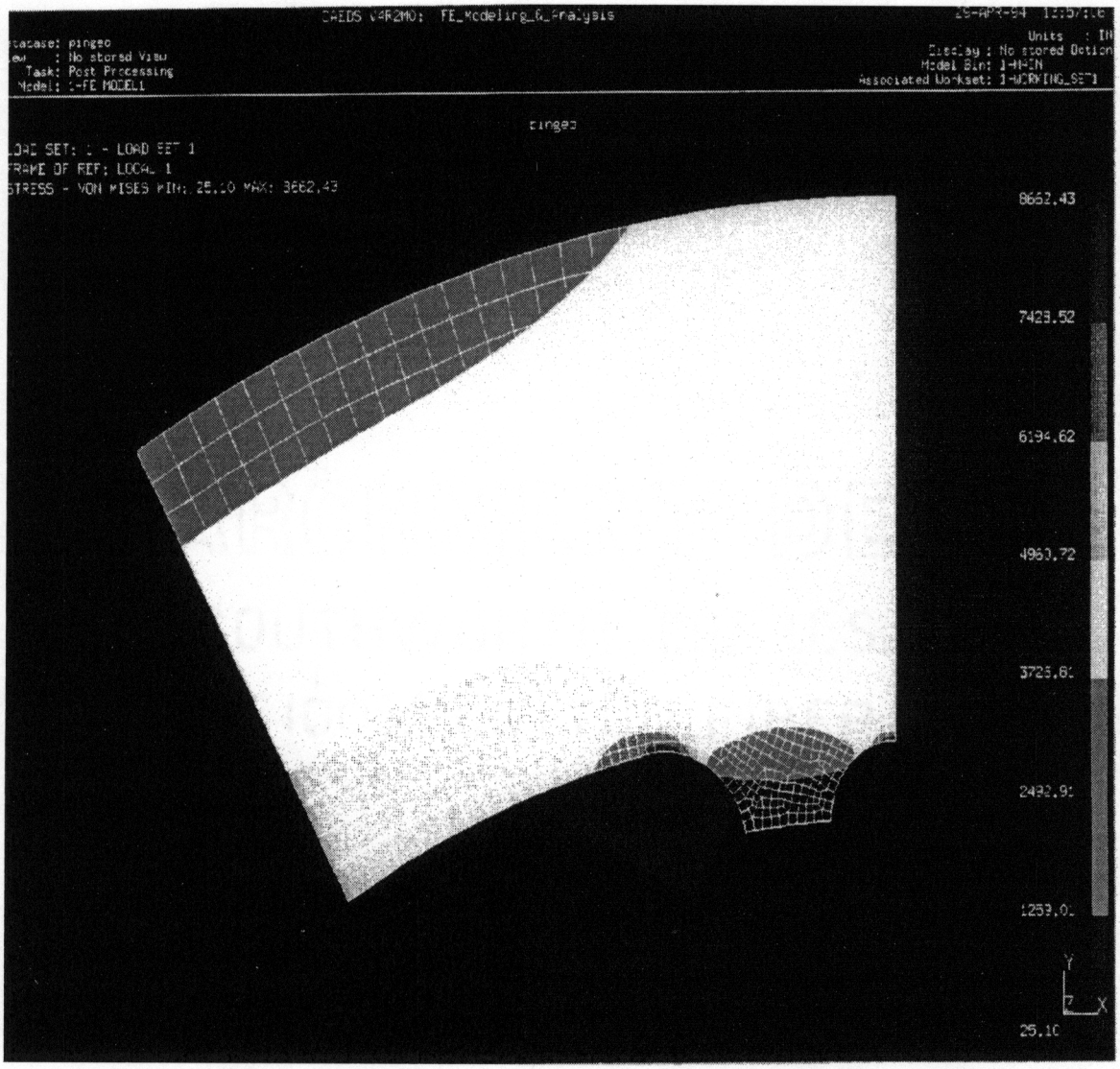

Fig.B-H.3. von Mises stress contours for Problem 3.

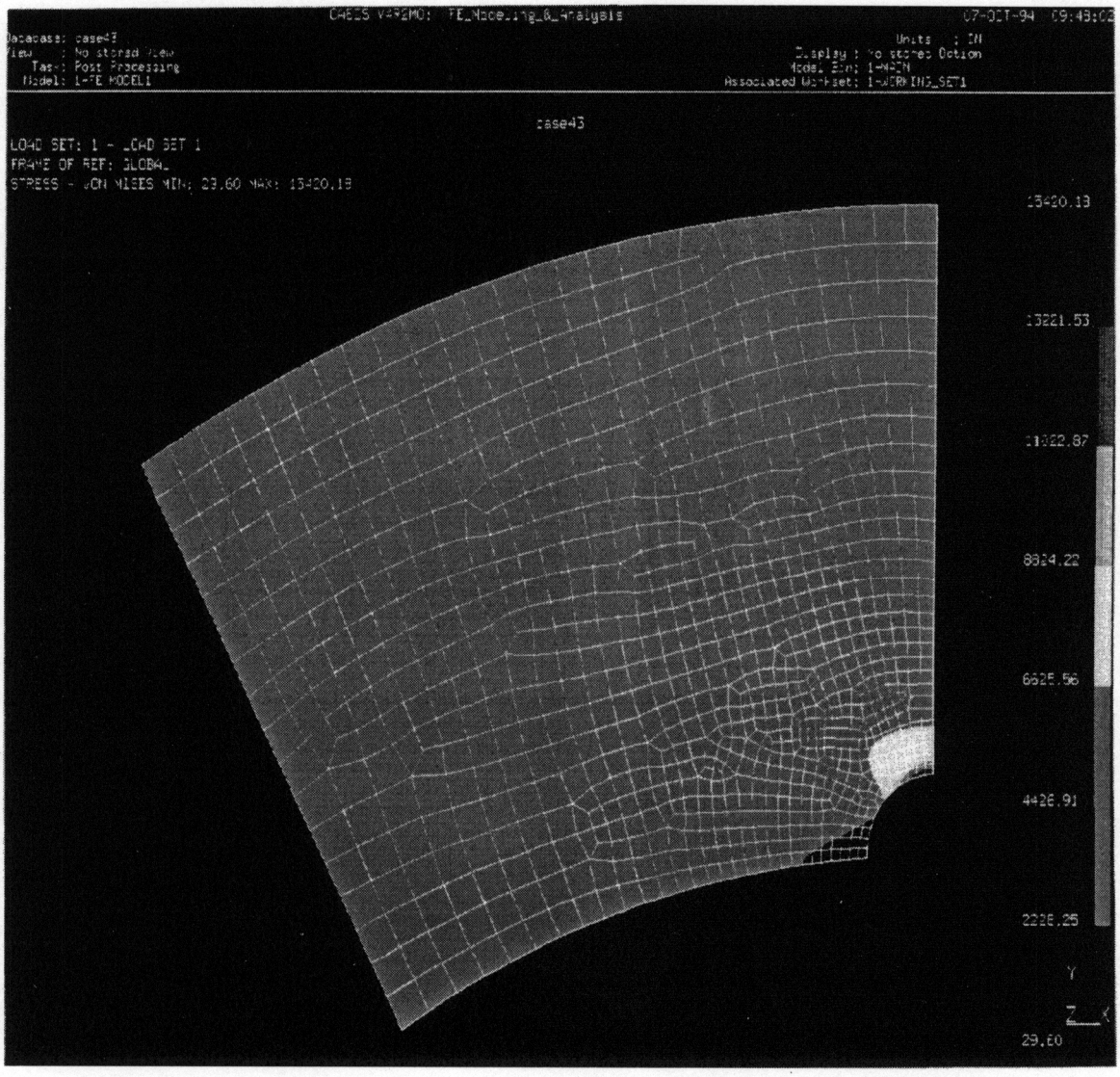

Fig.B-H.4. von Mises stress contours for the alternative problem (Oxford's design).

Appendix B-I.

Details of FEM Problem 4

Computational domain:	See Fig.B-I.1
Mesh elements:	Plane stress, linear quadrilateral
	Thickness: 0.375 in. for all three mesh areas (See Fig.B-I.2)
Mesh size:	See Figs.B-I.2 and B-I.3
Material:	Ti-6Al-4V for Mesh Areas 1 and 2
	Stainless steel 432, for Mesh Area 3
Number of elements:	762 on Mesh Area 1
	1316 on Mesh Area 2
	230 on Mesh Area 3
Number of nodes:	814 on Mesh Area 1
	1391 on Mesh Area 2
	255 on Mesh Area 3
Boundary conditions:	See Figs.B-I.2 and B-I.3

Comments:
The radial boundaries of the mesh areas are periodic due to the presence of symmetry planes. For imposing the periodicity, the local displacement coordinate systems of the nodes on these boundaries had to be changed to the global cylindrical coordinate system. Then, for the corresponding nodes $\Delta r_1=\Delta r_2$ and $\Delta\theta_1=\Delta\theta_2$.

The torque transferred from the shaft to the hub is imposed by restraining one of the hub periodic boundaries to have an average $\Delta\theta=0$, and placing a concentrated force on one of the nodes inside the shaft mesh area fairly far from the pin. Using a concentrated force is an approximation, since in reality the torque is imposed by a distributed $\tau_{\theta z}$ stress field in the shaft. However, the local presence of that stress field is negligible. What determines the stress concentrations is the moment integral of the $\tau_{\theta z}$ stress field, which is represented by the moment of the concentrated force around the center point. The point that was chosen was 0.6669" away from the center, therefore to achieve 3386 lb·in the magnitude of the force had to be 3386/0.6669=1141 [lb].

The pin as a solid two-dimensional body has three degrees of freedom. Due to the perfect symmetry of the pin, the number of degrees of freedom can be reduced by one by coupling one node on the edge of the pin with a node on either the hub or the shaft, at a location where contact was obviously maintained. Physically, the application of the

Node to Node Gap elements now make the pin statically determinate. However, the reduction of the large linear system matrix is done before the Node to Node Gap elements are taken into the model, therefore singularity error results. The same problem was encountered earlier related with FEM Problem 2, and the same solution can be used here. A point was selected inside the pin computational domain (x,y)=(0.003854,1.0020), a displacement was placed on it, and this displacement was iterated until the reaction forces approached zero. At the end of the iteration the displacement was $\Delta x=-6.08\times10^{-4}$, $\Delta y=7.7\times10^{-5}$, and the reaction forces were $F_x=-2.654$ lb and $F_y=0.236$ lb, which are low compared to the 1141 lb of the load force.

Results are presented in Figs.B-I.4-B-I.6. In Fig.B-I.4 the deformation of the mesh areas can be seen. Fig.B-I.5 shows the deformations in the pin region. Fig.B-I.6 is the contour plot of the Von Mises stresses zoomed again on the critical pin region.

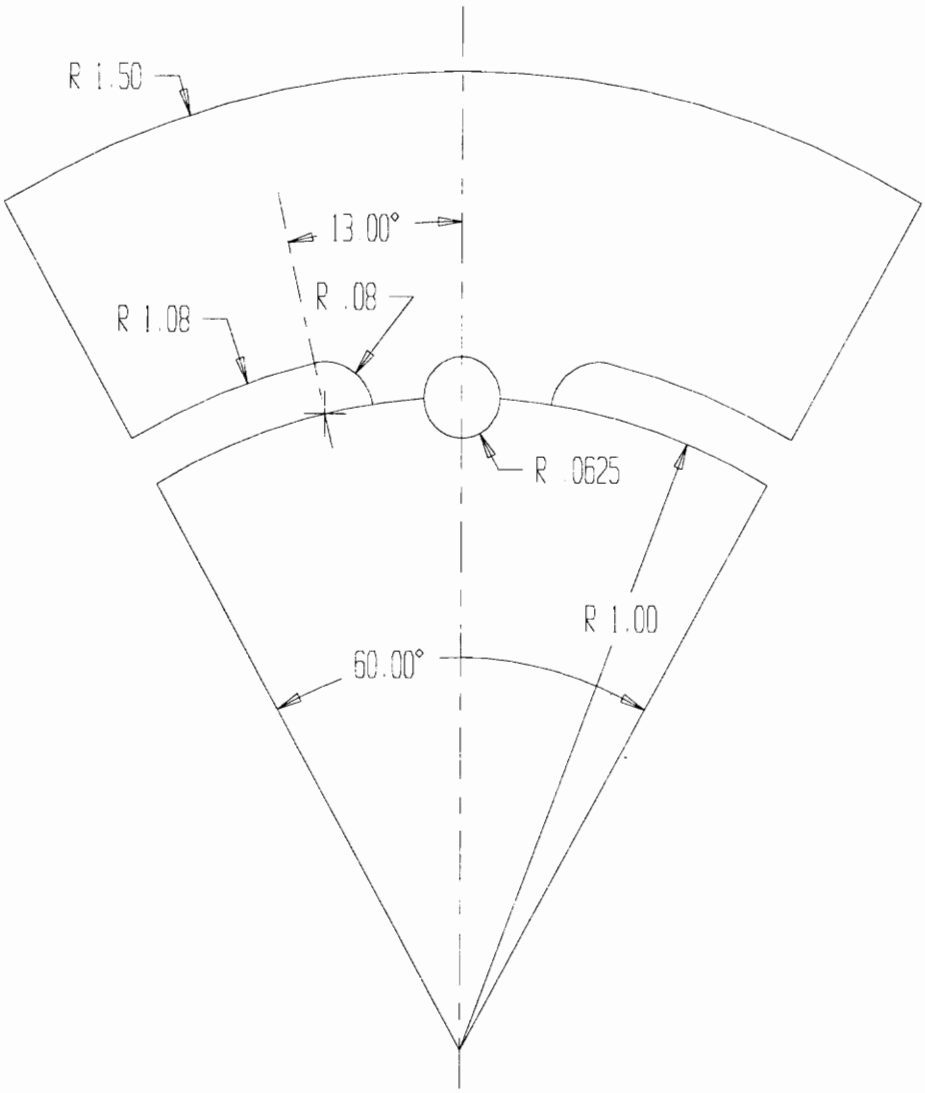

Fig.B-I.1. Computational domain for Problem 4

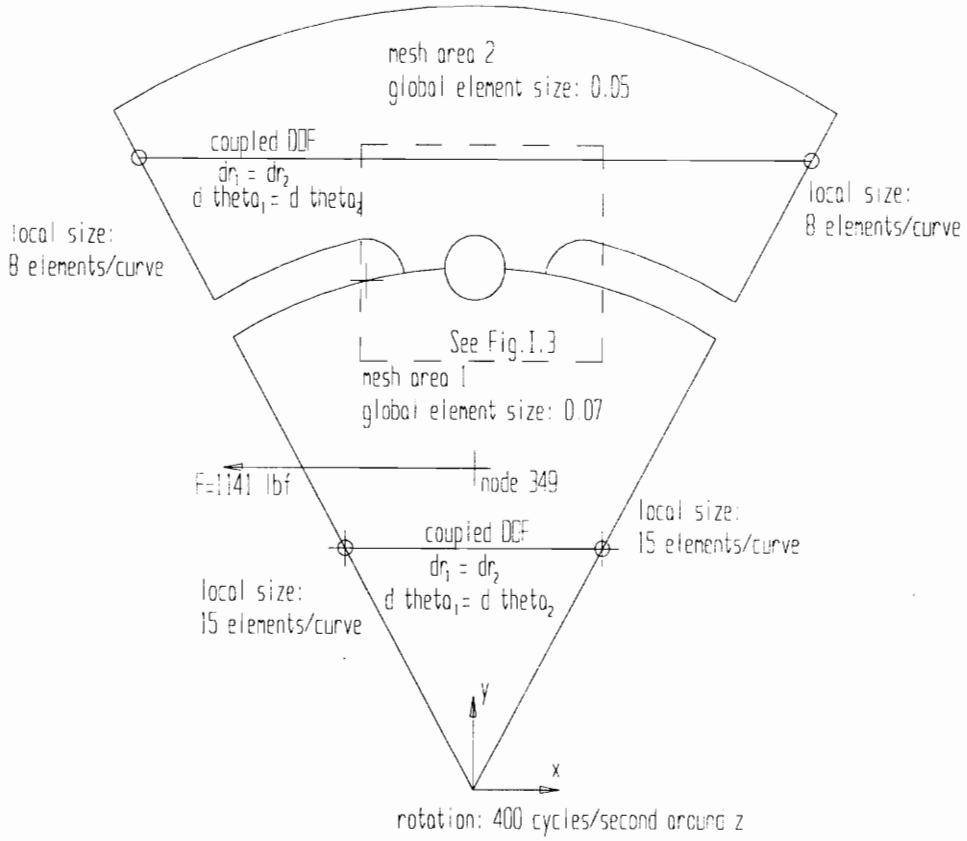

Fig.B-I.2. Mesh and boundary conditions for Problem 4

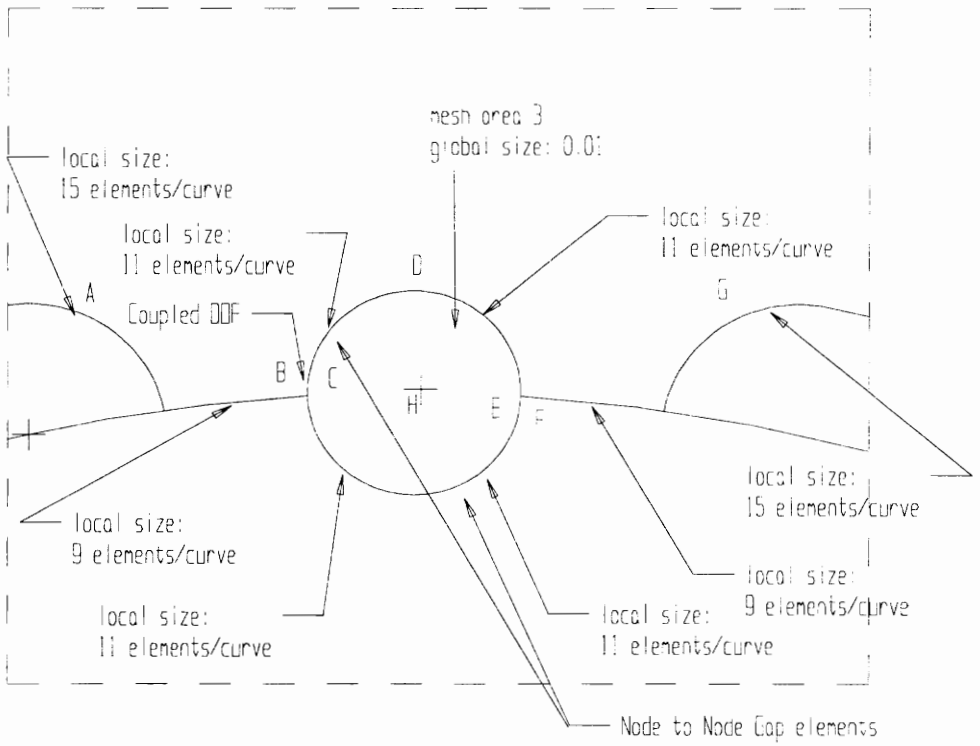

Fig.B-I.3. Detail of mesh and boundary conditions around the coupling pin (Problem 4)

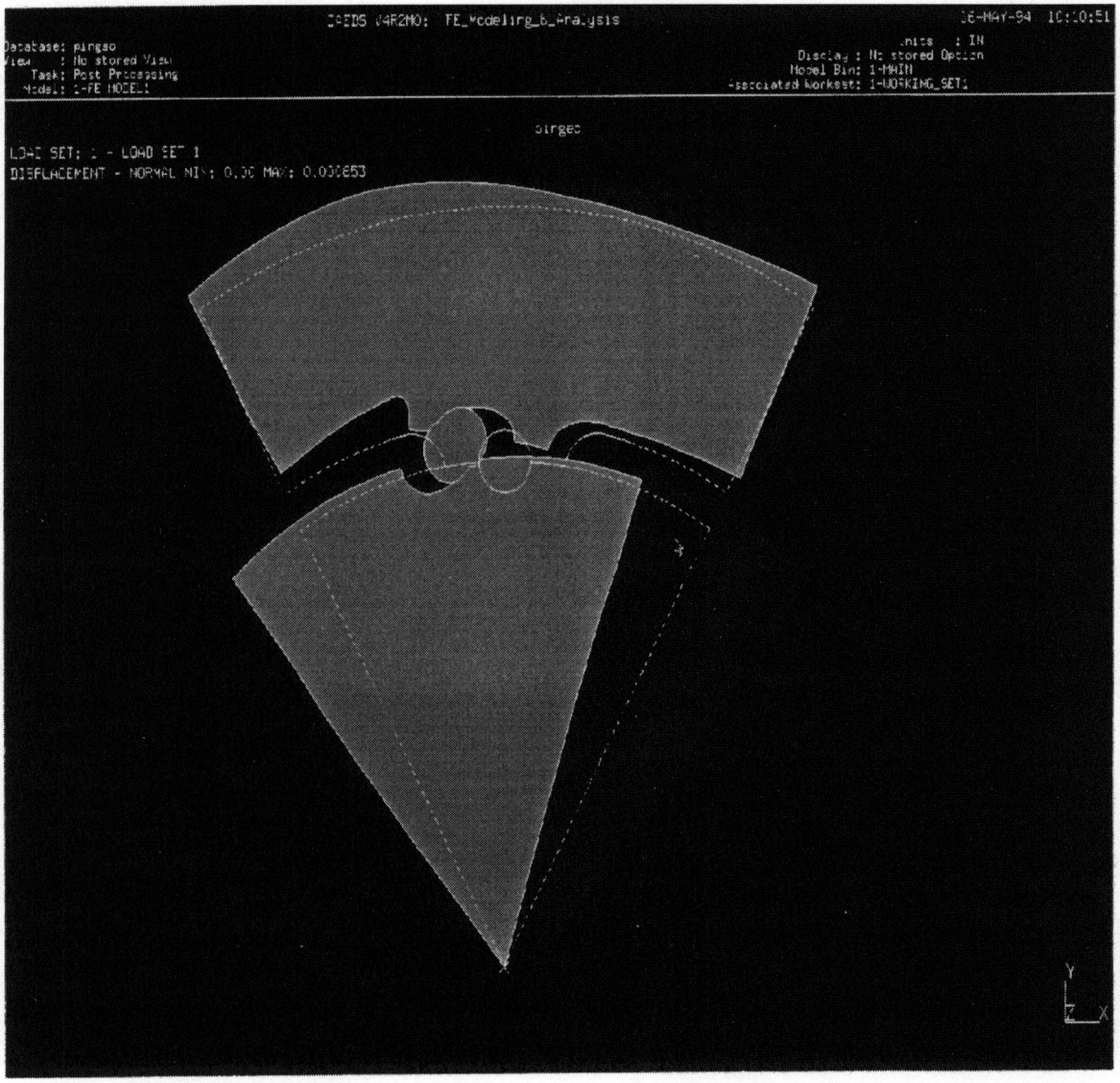

Fig.B-I.4. Deformation of the mesh areas for Problem 4.

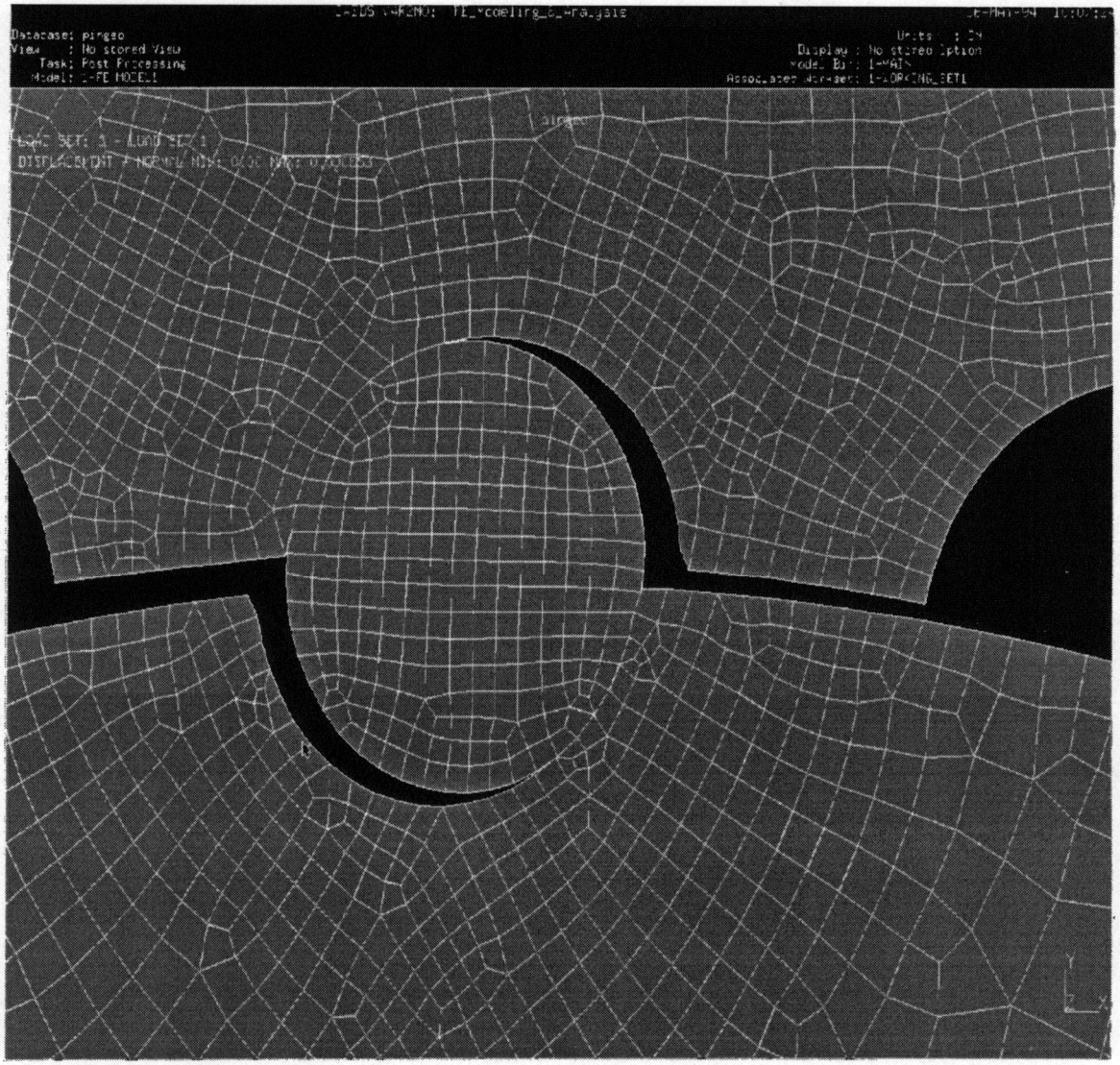

Fig.B-I.5. Deformation around the pin for Problem 4

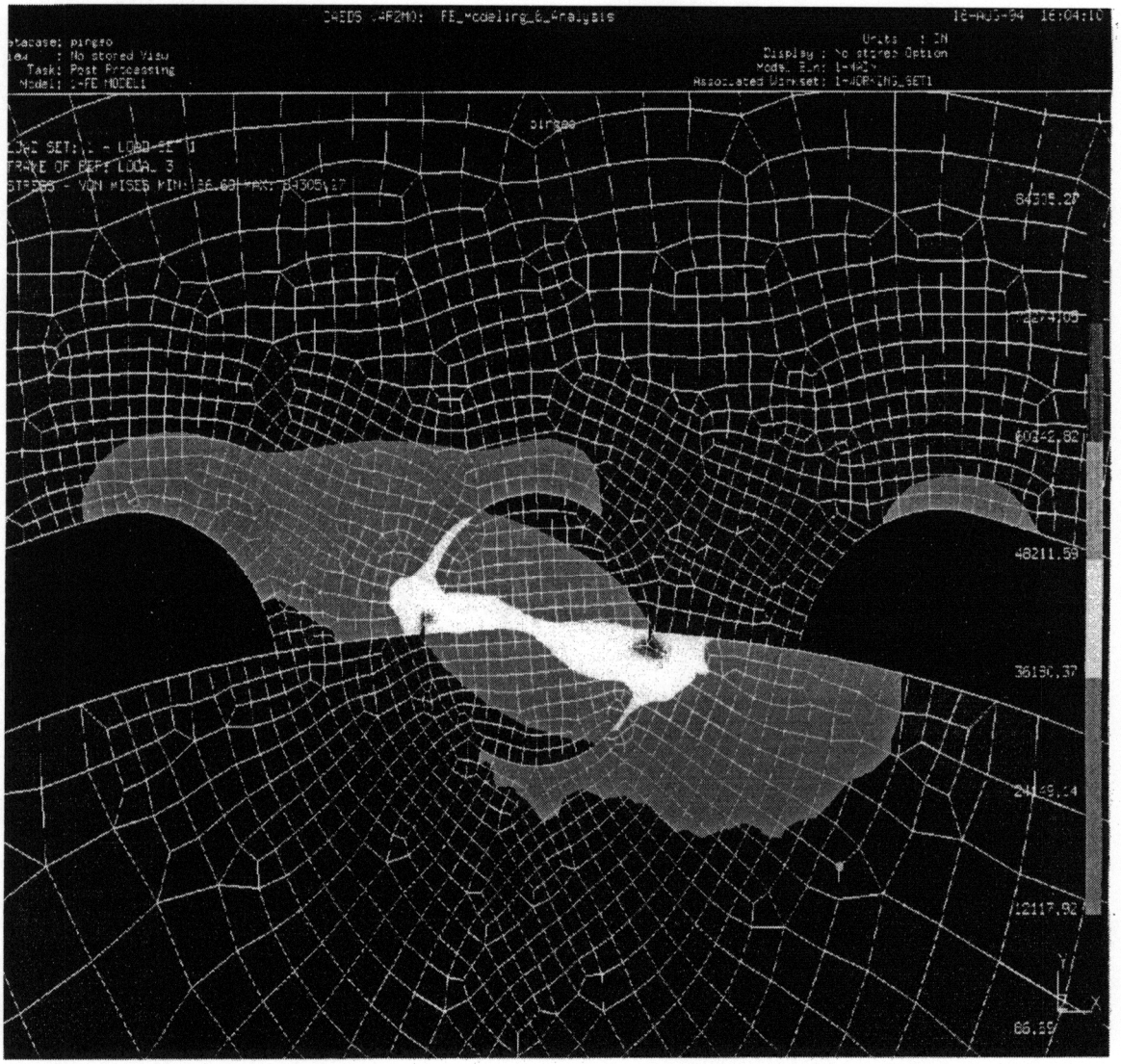

Fig.B-I.6. von Mises stress contours (zoomed at pin region) for Problem 4

Appendix C: CRTSPD Input and Output

The CRTSPD program input deck is included on pages 128 and 129. The program output is listed on pages 130 through 133.

```
Titanium Disk (45 mm Bore Reference Bearing)
5-1/8" X 3" OD Flexible Coupling - 1/2 Mass Approximation
Overhung Design - Axial Pin Mounting
        30          9          2         21         28
         0
     29.00     .28300   11.15000                                        0
   .1E+06
   .15E+06
   .26E+06
   .41E+06
   .27E+06
   .47E+06
   .3E+06
   .56E+06
   .32E+06
   .61E+06
   .36E+06
   .67E+06
   .47E+06
   .77E+06
   .61E+06
   .88E+06
   .1E+07
   .15E+07
    500.00 100000.00    500.00
       .00       .25       .01       .00       .00       .00    .625    .000    .000
       .31       .37       .01       .00       .38       .18    .625    .000    .000
       .00       .25       .63       .00       .00       .00    .625    .000    .250
       .31       .25       .63       .00       .38       .18    .625    .000    .250
       .00       .25       .63       .00       .00       .00    .625    .000    .250
```

.00	.25	.63	.00	.00	.00	.625	.000	.250
.00	.25	.63	.00	.00	.00	.625	.000	.250
.00	.25	1.93	.00	.00	.00	1.930	.000	.250
.66	.25	1.93	.00	.99	.51	1.930	.000	.250
.00	.25	1.93	.00	.00	.00	1.930	.000	.250
.00	.19	2.00	.00	.00	.00	2.000	.000	.188
.66	.19	2.00	.00	.99	.51	2.000	.000	.188
.00	1.00	2.00	.00	.00	.00	2.000	.000	1.000
7.00	.25	2.00	.00	58.82	30.53	2.000	.000	.250
.00	.25	2.00	.00	.00	.00	2.000	.000	.250
.00	1.00	2.00	.00	.00	.00	2.000	.000	1.000
.00	.25	3.00	.00	.00	.00	3.000	.000	.250
.00	.25	3.00	.00	.00	.00	3.000	.000	.250
.00	1.00	2.13	.00	.00	.00	2.125	.000	1.000
.00	.32	1.77	.00	.00	.00	1.770	.000	.315
.60	.33	1.77	.00	1.03	.54	1.770	.000	.315
.00	.80	1.70	.00	.00	.00	1.700	.000	.800
.00	.80	1.70	.00	.00	.00	1.700	.000	.800
.00	.75	1.70	.00	.00	.00	1.700	.000	.750
.00	.78	1.70	.00	.00	.00	1.700	.000	.775
.00	.25	1.75	.00	.00	.00	1.750	.000	.250
.00	.30	1.57	.00	.00	.00	1.570	.000	.300
.55	.30	1.57	.00	.82	.43	1.570	.000	.300
.00	.89	1.53	.00	.00	.00	1.530	.000	.890
.00	.01	1.53	.00	.00	.00	1.530	.000	.010

NEGAVIB RESEARCH AND CONSULTING --- VPI&SU --- --ROTOR
DYNAMICS ANALYSIS CRITICAL SPEEDS OF A FLEXIBLE ROTOR

Titanium Disk (45 mm Bore Reference Bearing)
5-1/8" X 3" OD Flexible Coupling - 1/2 Mass Approximation
Overhung Design - Axial Pin Mounting

CRTSPD1 - MODAL ANALYSIS VERSION 12/1/76

N = 30 STATIONS NB = 2 BEARINGS NSK= 9 STIFFNESS VALUES
NGYR = 0 MASS = 0 DSP= 500.00

TOTAL ROTOR ASSEMBLY C.G.= 5.29 INCHES FROM STA. 1.
BEARING REACTION AT STA. 21 = 28.35 LB
BEARING REACTION AT STA. 28 = -9.53 LB

BEARING STATIONS 21 28

BEARING NUMBER	BEARING LOCATION	SPEED DEPENDENT BEARING STIFFNESS CHARACTERISTICS K1 (LB/IN)	K2 (LB-SEC/IN)	K3 (LB-SEC2/IN)
		STIFFNESS CASE NO. 1		
1	21	1.000E+05	.000E+00	.000E+00
2	28	1.500E+05	.000E+00	.000E+00

STIFFNESS CASE NO. 2

1	21	2.600E+05	.000E+00	.000E+00
2	28	4.100E+05	.000E+00	.000E+00

STIFFNESS CASE NO. 3

1	21	2.700E+05	.000E+00	.000E+00
2	28	4.700E+05	.000E+00	.000E+00

STIFFNESS CASE NO. 4

1	21	3.000E+05	.000E+00	.000E+00
2	28	5.600E+05	.000E+00	.000E+00

STIFFNESS CASE NO. 5

1	21	3.200E+05	.000E+00	.000E+00
2	28	6.100E+05	.000E+00	.000E+00

STIFFNESS CASE NO. 6

1	21	3.600E+05	.000E+00	.000E+00
2	28	6.700E+05	.000E+00	.000E+00

STIFFNESS CASE NO. 7

1	21	4.700E+05	.000E+00	.000E+00
2	28	7.700E+05	.000E+00	.000E+00

STIFFNESS CASE NO. 8

1	21	6.100E+05	.000E+00	.000E+00
2	28	8.800E+05	.000E+00	.000E+00

STIFFNESS CASE NO. 9

1	21	1.000E+06	.000E+00	.000E+00
2	28	1.500E+06	.000E+00	.000E+00

Titanium Disk (45 mm Bore Reference Bearing)
5-1/8" X 3" OD Flexible Coupling - 1/2 Mass Approximation
Overhung Design - Axial Pin Mounting

INITIAL SPEED = 500.0 RPM
FINAL SPEED = 100000.0 RPM
SPEED INCREMENT = 500.0 RPM

SUMMARY OF CRITICAL SPEEDS AND BEARING STIFFNESS VALUES

STIFFNESS CASE NO.	CRITICAL SPEED NO.	CRITICAL SPEED	K1	K2
1				
	1	7728.7	1.000E+05	1.500E+05
	2	46591.8	1.000E+05	1.500E+05
2				
	1	12054.6	2.600E+05	4.100E+05
	2	75302.9	2.600E+05	4.100E+05

3				
	1	12315.0	2.700E+05	4.700E+05
	2	79673.5	2.700E+05	4.700E+05
4				
	1	12935.6	3.000E+05	5.600E+05
	2	85797.9	3.000E+05	5.600E+05
5				
	1	13313.7	3.200E+05	6.100E+05
	2	88931.2	3.200E+05	6.100E+05
6				
	1	13987.5	3.600E+05	6.700E+05
	2	92698.8	3.600E+05	6.700E+05
7				
	1	15540.0	4.700E+05	7.700E+05
	2	99079.3	4.700E+05	7.700E+05
8				
	1	17129.3	6.100E+05	8.800E+05
9				
	1	20508.4	1.000E+06	1.500E+06

Appendix D: Disk Kinetic Energy Calculations

The disk burst energy was calculated as the kinetic energy of multiple disk fragments. The analysis involved dividing the disk into 40 concentric, constant-thickness segments of radii from 1.0 inches to 5.0 inches. The centroid of each segment was then determined using differential elements (see Figure D.1) in the following manner.

Area of the element = $rd\theta dr$

Element moment about y axis = $rd\theta$ x dr x $r\cos\theta$

$$= r^2\cos\theta dr d\theta$$

Total moment of area about y axis

$$= \int_{-\alpha}^{\alpha}\int_{R_1}^{R_2} r^2\cos\theta dr d\theta$$

$$= \left[\frac{r^3}{3}\right]_{R_1}^{R_2}\left[\sin\theta\right]_{-\alpha}^{\alpha}$$

$$= \frac{R_2^3 - R_1^3}{3} 2\sin\alpha$$

Total area of the segment

$$= \int_{-\alpha}^{\alpha}\int_{R_1}^{R_2} r dr d\theta$$

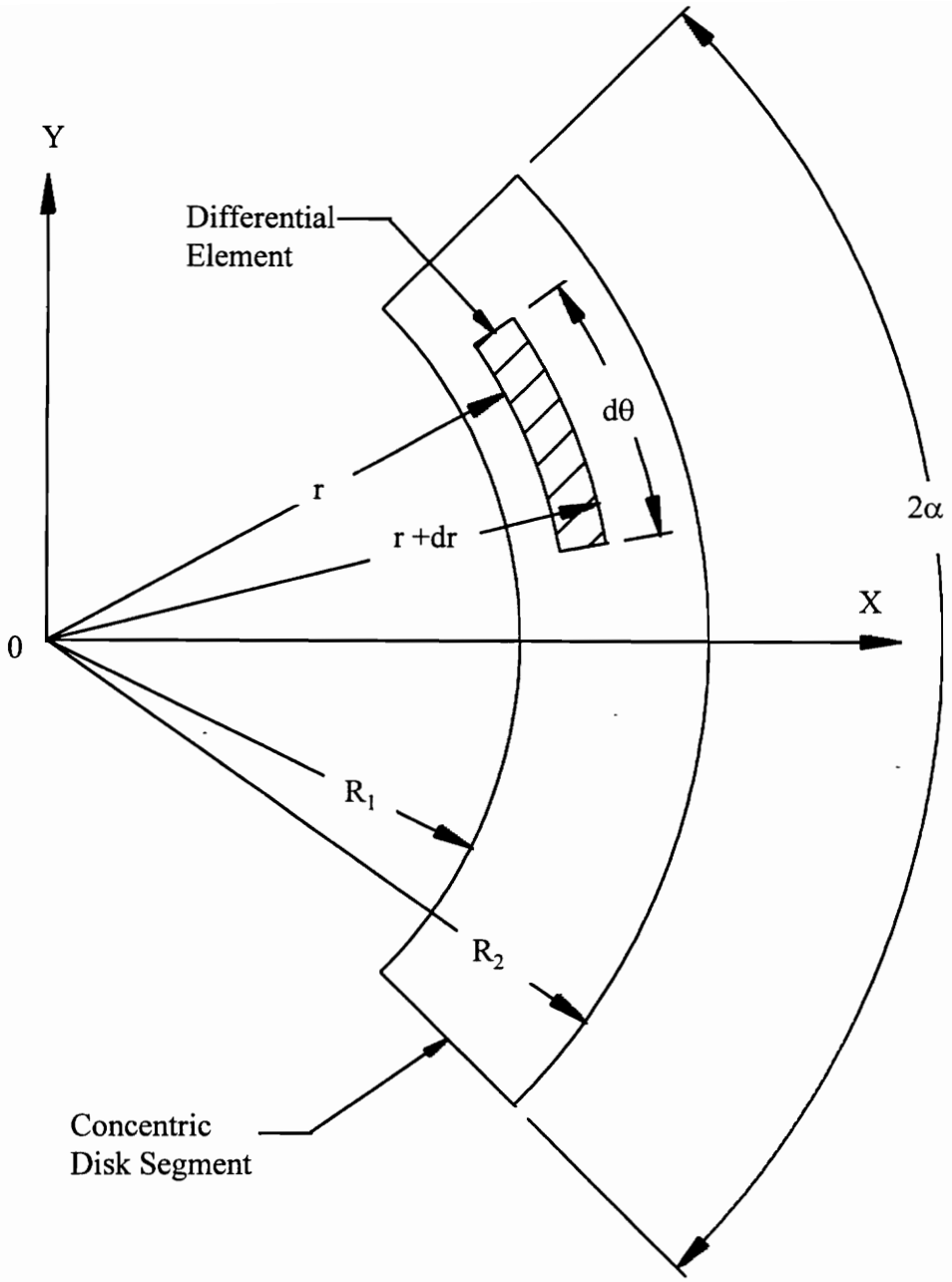

Figure D.1: Centroid Determination

$$= \int_{-\alpha}^{\alpha} \left[\frac{r^2}{2} \right]_{R_1}^{R_2} d\theta$$

$$= \frac{R_2^2 - R_1^2}{2} \left[\theta \right]_{-\alpha}^{\alpha}$$

$$= \left(R_2^2 - R_1^2 \right) \alpha$$

The distance of the centroid from the center O

$$= \frac{\text{Moment of area about } y \text{ axis}}{\text{Area of the segment}}$$

$$= \frac{\frac{R_2^3 - R_1^3}{3} 2\sin\alpha}{\left(R_2^2 - R_1^2 \right) \alpha} \qquad \text{D.1}$$

The preceding method was taken from Hagerty (1975).

After determining the centroid for each segment, the segment mass was calculated. Using the segment mass and centroid, a composite centroid for multiple segments (composing a disk fragment) was calculated in the following manner.

$$\overline{X} = \frac{\sum mass_i \bullet \overline{X}_i}{\sum mass_i} \qquad \text{D.2}$$

The kinetic energy of the disk fragment was then calculated using the composite centroid in the following manner.

$$\text{Velocity} = \overline{X} \bullet \omega$$

$$E_k = \frac{\frac{1}{2} mass \bullet velocity^2}{g_c} \qquad \text{D.3}$$

Table D.1 was created using the preceding equations and the following assumptions:

1. Operating speed of 24,000 RPM.

Table D.1: Disk Kinetic Energy at 24,000 RPM

Disk Radius inches	Disk Thickness inches	Segment Mass lbm	Segment R_{cg} inches	Fragment R_{cg} inches	Fragment Velocity ft/s	Fragment E_k ft-lbf
5.0	0.30					
4.9	0.30	.1502	4.950	4.950	1037	2509
4.8	0.30	.1472	4.850	4.901	1026	4869
4.7	0.30	.1442	4.750	4.852	1016	7085
4.6	0.30	.1411	4.650	4.803	1006	9162
4.5	0.30	.1381	4.550	4.754	996	11106
4.4	0.30	.1350	4.450	4.706	986	12922
4.3	0.30	.1320	4.350	4.659	976	14615
4.2	0.20	.0860	4.250	4.626	969	15665
4.1	0.20	.0840	4.150	4.592	962	16639
4.0	0.20	.0819	4.050	4.556	954	17540
3.9	0.20	.0799	3.950	4.519	946	18371
3.8	0.20	.0779	3.850	4.482	939	19136
3.7	0.20	.0759	3.750	4.444	931	19837
3.6	0.20	.0738	3.650	4.406	923	20477
3.5	0.20	.0718	3.550	4.368	915	21060
3.4	0.20	.0698	3.450	4.330	907	21588
3.3	0.20	.0678	3.350	4.293	899	22064
3.2	0.21	.0690	3.250	4.253	891	22512
3.1	0.22	.0701	3.150	4.212	882	22930
3.0	0.23	.0710	3.050	4.170	873	23318
2.9	0.24	.0716	2.950	4.128	864	23672
2.8	0.25	.0721	2.850	4.084	855	23994
2.7	0.26	.0723	2.750	4.040	846	24282
2.6	0.27	.0724	2.650	3.995	837	24537
2.5	0.28	.0722	2.550	3.950	827	24757

Table D.1 (Cont.): Disk Kinetic Energy at 24,000 RPM

Disk Radius inches	Disk Thickness inches	Segment Mass lbm	Segment R_{cg} inches	Fragment R_{cg} inches	Fragment Velocity ft/s	Fragment E_k ft-lbf
2.4	0.29	0.0719	2.450	3.905	818	24945
2.3	0.30	0.0713	2.350	3.860	809	25099
2.2	0.33	0.0759	2.250	3.812	798	25231
2.1	0.37	0.0797	2.150	3.762	788	25337
2.0	0.40	0.0830	2.050	3.710	777	25414
1.9	0.43	0.0855	1.950	3.656	766	25461
1.8	0.47	0.0873	1.850	3.601	754	25476
1.7	0.50	0.0885	1.750	3.546	743	25461
1.6	0.60	0.1001	1.651	3.484	730	25409
1.5	2.50	0.3920	1.551	3.265	684	25166
1.4	2.50	0.3667	1.451	3.091	647	24948
1.3	2.50	0.3414	1.351	2.949	618	24725
1.2	2.50	0.3161	1.251	2.829	593	24484
1.1	2.50	0.2908	1.151	2.727	571	24222
1.0	2.50	0.2655	1.051	2.639	533	23940

Segment = disk section between consecutive radii

Fragment = disk section between current radius and outer edge

For example, at a radius = 1.5 inches, the segment is defined as the disk section with an inner radius of 1.5 inches and an outer radius of 1.6 inches. The fragment is defined as the disk section with an inner radius of 1.5 inches and an outer radius of 5.0 inches.

2. Disk fragments in a large number of symmetric, radial sections (this minimizes the sector angle α and maximizes the composite centroid and resulting kinetic energy).

3. The table presents sensitivity cases for symmetric fragments of varying radii. For example, the kinetic energy reported for a fragment at a radius of 3 inches is based on calculations for a composite of all disk segments from radii of 3 inches to 5 inches. Likewise, the kinetic energy reported for a fragment at a radius of 1 inch is based on a composite of all disk segments.

As indicated in Table D.1, a maximum kinetic energy value of 25,476 ft-lbf was calculated for the disk operating at 24,000 RPM. This value roughly corresponds to 36% of the explosive energy of one 200g stick of Ammonia Gelatin Dynamite (TNT). The explosive energy estimate for TNT was obtained from Explosives and Rock Blasting.

References

1. Atlas Powder Company, Explosives and Rock Blasting, Atlas Powder Company, Dallas, Texas, 1987

2. Bayley, F. J., and Priddy, W. J., "Effects of Free-Stream Turbulence Intensity and Frequency on Heat Transfer to Turbine Blading", ASME Paper no. 80-GT-79, 1980.

3. Doorly, D. J., "A Study of the Effect of Wake-Passing on Turbine Blades", Ph.D. Thesis, Oxford University, O. U. E. L. Report 1515/84, 1984.

4. Doorly, D. J., and Oldfield, M. L. G., "Simulation of the Effects of Shock Wave Passing on a Turbine Rotor Blade", *ASME Journal of Engineering for Gas Turbines and Power*, Vol. 107, pp. 998-1006, (Also ASME Paper no. 85-GT-112), 1985.

5. Ehrich, F. F., Handbook of Rotordynamics, McGraw-Hill, Inc., New York, 1992.

6. Hagerty, W. H., Engineering Mechanics, R. E. Kreiger Pub. Co., Huntington, New York, 1975.

7. Hoerner, S. F., Fluid-Dynamic Drag, Wiley, Midland Park, N. J., 1965.

8. Muster, D., and Flores, B., "Balancing Criteria and Their Relationship to Current American Practice", *ASME Journal of Engineering for Industry*, pp. 1035-1046, November 1969.

9. Peterson, R. E., Stress Concentration Factors, Wiley, New York, 1974.

10. Pfeil, H., Herbst, R., and Schroeder, T., "Investigation of the Laminar-Turbulent Transition of Boundary Layers Disturbed by Wakes", ASME Paper no. 82-GT-124, 1982.

11. Rao, J. S., Rotor Dynamics, John Wiley & Sons, New York, 1991.

12. Timoshenko, S., Strength of Materials, R. E. Kreiger Pub. Co., Huntington, New York, 1976.

Vita

David Allen White was born in Albany, Georgia on February 16, 1966. He grew up in Mathews, Virginia. After graduating from Mathews High School in June 1984, he began his undergraduate studies in petroleum engineering at Mississippi State University. He worked as a summer engineering intern for the U. S. Army at Fort Eustis, Virginia and later for Chevron in New Orleans, Louisiana. In May 1989, he graduated Summa Cum Laude with a Bachelor of Science degree. He then began working as a petroleum engineer for Chevron in New Orleans, Louisiana. He began his graduate work at Virginia Polytechnic Institute and State University in January 1993, and completed his Master of Science in Mechanical Engineering in December of 1995.

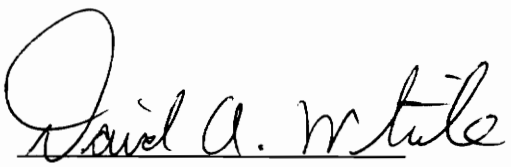

David A. White